NATIONAL AERONAUTICS AND SPACE ADMINISTRATION

REMOTE SENSING: A SURVEY REPORT

By Kenneth B. Craib
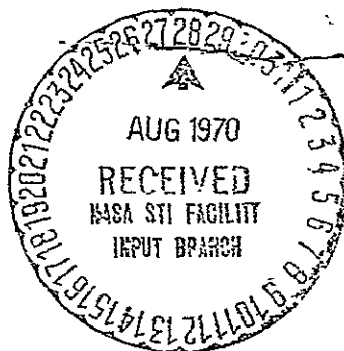
PRICES SUBJECT TO CHANGE

MANNED SPACECRAFT CENTER
HOUSTON, TEXAS
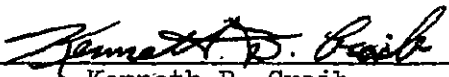### August 11, 1967
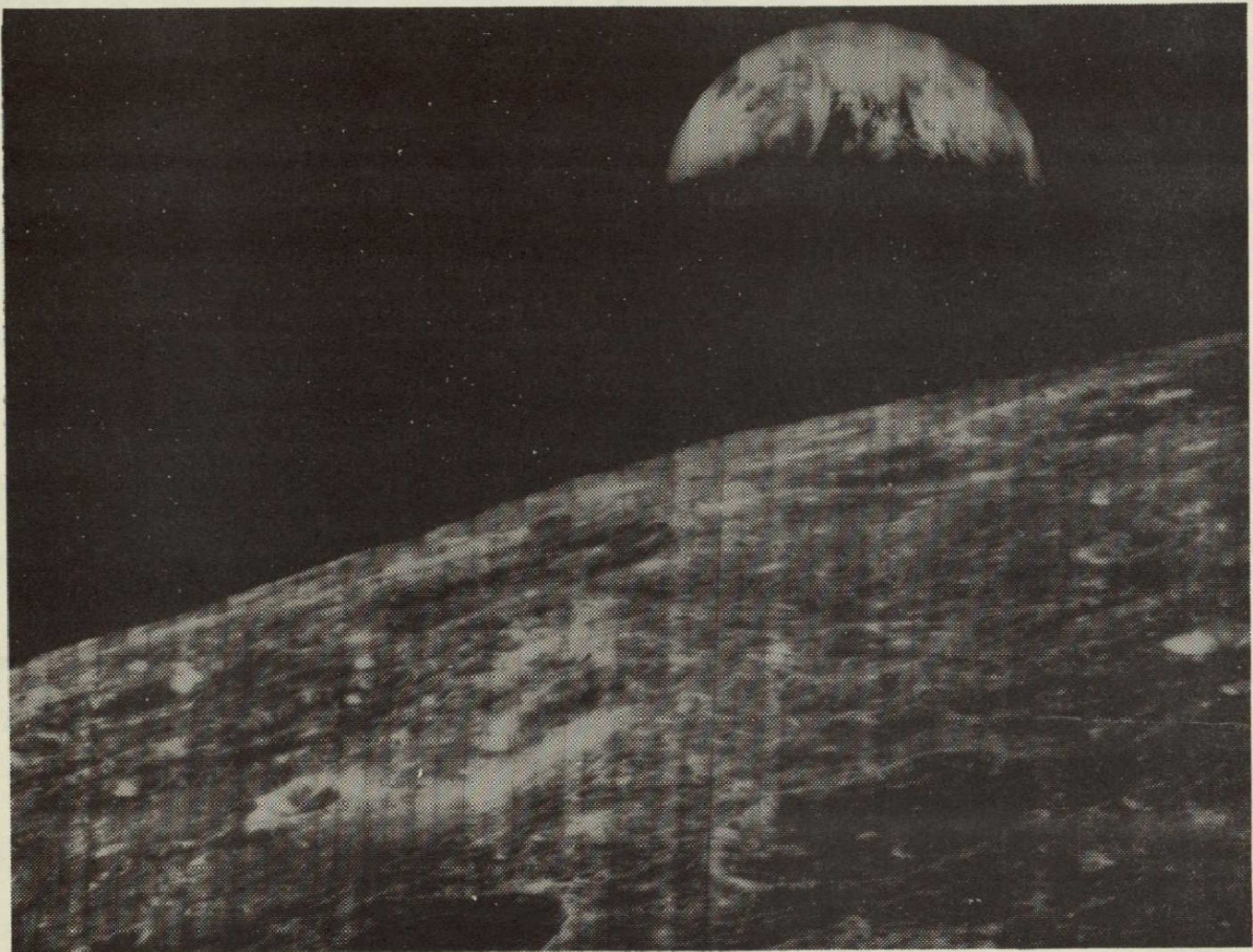
The first photograph of the Earth as seen from the lunar environment.
(Lunar Orbiter I photograph)

"For man must rise above this earth to the top of the
atmosphere and beyond, where, in the solitudes of space,
he may contemplate the earth, for only thus will he ever
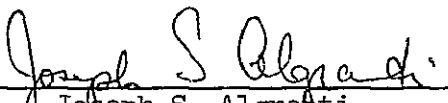come to understand fully this world in which he lives."

Paraphrased from Socrates, 500 B.C.

REMOTE SENSING: A SURVEY REPORT

PREPARED BY

Kenneth B. Craib
Aircraft Operations Office

AUTHORIZED FOR DISTRIBUTION

Joseph S. Algranti
Chief, Aircraft Operations Office

NATIONAL AERONAUTICS AND SPACE ADMINISTRATION
MANNED SPACECRAFT CENTER
HOUSTON, TEXAS
August 11, 1967

ABSTRACT

A survey of remote-sensing techniques and measurement systems is presented. These are considered by area of application as extraterrestrial, atmospheric, and geophysical. Basic energy equations, interactions, and environmental restrictions are reviewed. Sensor systems used in each area are presented, data samples are shown, and information content is discussed. The advantages provided by multispectral scanning from high-altitude observation platforms are shown. References are given, and a comprehensive bibliography is developed as a part of this report.

REMOTE SENSING: A SURVEY REPORT

By Kenneth B. Craib
Manned Spacecraft Center

SUMMARY

. The primary purpose of this report is to review and examine present techniques and systems used in remote sensing. The available time and space have limited the number of research approaches that may be considered; however, representative sensors are shown and discussed for each of the primary areas under investigation. The importance of obtaining data across the entire electromagnetic spectrum is emphasized.

The application of high-altitude remote geophysical sensing technology is increasing at a logarithmic rate. The author is aware of several new techniques that have been developed or announced since this report began, which unfortunately could not be mentioned here, although an attempt has been made to integrate especially significant discoveries.

A secondary objective of this report was the development of a comprehensive bibliography dealing with the science of remote sensing. In this regard, over 250 reports, books, and articles have been reviewed since this report was conceived in October 1966. The majority of these are included here and referenced in the text.

INTRODUCTION

The technique of remote sensing, or "measurement at a distance," is applied whenever man desires to minimize external disturbances which may affect the validity of resultant data, or when it is not possible for him to directly measure a physical phenomenon. Observations from a distance recorded on a macroscale may also provide information unobtainable from a closer vantage point. In this regard, the human senses are reasonably good qualitative tools; however, they have limited quantitative capabilities and are sensitive to only a small portion of the electromagnetic spectrum. Our eyes respond to light in the 4000- to 7000-A range and our ears respond to sound between 16 and 20 000 Hz, but exact measurements within those ranges are difficult. Furthermore, other turmoil effects in the universe are undetected by the senses.

A variety of instruments have been designed to compensate for these human limitations, extending man's senses into regions hitherto denied him, thus providing a quantitative measuring capability. Cameras, infrared detectors, and radio-frequency (rf) receivers have been designed to detect electromagnetic radiation; magnetometers and gravity meters have been designed to detect force fields; and scintillation counters have been designed to detect radioactivity. One early instrument, the Choko seismometer, built in China around 136 A.D., was designed to detect and locate the origin of earthquakes (ref. 1). Although based on the misconception that the ground moves in a particular direction when earthquake waves pass a given point, it was, nonetheless, an attempt to obtain a measurement beyond the capabilities of the human senses. The technique of stop-action photography, developed in the 19th century to settle a bet concerning whether or not a running horse had all four feet in the air at any given time, represents a similar attempt to obtain such information. Over the years many such techniques and systems have evolved in man's quest for knowledge and better understanding of his environment.

The majority of remote sensors in present use were originally developed to satisfy increasing military demands, but their application is by no means limited to this area. Recently, there has been an increasing awareness of the need for a better understanding and exploitation of our natural resources. An increasing population, resulting in a subsequent drain on the food and energy supply of the world, has provided at least one significant impetus. Remote-sensing systems and technology may make several valuable contributions in these areas, particularly when it is considered that data can now be obtained from aircraft and orbital altitudes.

SYMBOLS

C   ground coverage, ft

C_1 $2\pi hc^2$, where $h = 6.6252 \times 10^{-34}$ J/sec; and c = velocity of light in a vacuum, 3.0×10^8 m/sec

C_2 $\frac{hc}{k}$, where k is the Boltzmann constant, 1.3805×10^{-23} J/°K; c = velocity of light in a vacuum, 3.0×10^8 m/sec; and h = Planck constant, 6.6252×10^{-34} J/sec.

c   velocity of light in a vacuum, 3.0×10^8 m/sec

D*   spectral D-star or detectivity

E total radiant emittance of a black body

E_i incident radiant energy

E_t transmitted energy

E_α absorbed energy

E_λ spectral radiance or spectral radiant emittance

E_ρ reflected energy

e   the base of natural logarithms, 2.718

F   focal length, in.

H   altitude above terrain, ft

h   Planck constant, 6.6252×10^{-34} J/sec

K   approximately equal to 2.897×10^3, yielding λ_{max} in microns

k   Boltzmann constant, 1.3805×10^{-23} J/°K

LFR   lens-film resolution, lines/mm

R   ground resolution, ft

T   temperature, °K

t   transmissivity

V   velocity

W   width of film format, in.

α   absorptivity

ε   emissivity

λ_{max} wavelength of frequency at which maximum radiation occurs

ρ reflectivity

σ the Stefan-Boltzmann constant, 5.6687×10^{-8} watts$/m^2/°K^4$

THE OUTER ENVIRONMENT

The science and technology presently employed in remote sensing may be roughly separated into three major areas characterized by the region under investigation: (1) the study of the Earth through an intervening medium, (2) the study of extraterrestrial phenomena through this same atmosphere or from space platforms, and (3) the study of the intervening medium itself.

Since earliest recorded history, man has been characterized by a driving curiosity to learn more about himself and his surrounding environment. One of the most fascinating aspects of his environment has been the Moon, along with the stars, the planets, and other extraterrestrial objects about which, until recently, man could only speculate. Today, high-powered cameras and telescopes, operating at both optical and radio wavelengths, provide much in the line of new knowledge and at least a partial understanding in many of these extraterrestrial areas.

One such system, the Super Schmidt Meteor Camera, operated by the Harvard Observatory, the Canadian Dominion Observatory, and the Air Force Cambridge Research Center, is shown in figure 1. A typical photograph taken by the camera is shown in figure 2. In this example, the chopped trail of a meteor is clearly visible above the black disk in the center of the photograph.

Sensors have also been placed in near-Earth orbits or have been carried aloft by sounding rockets or balloons to reduce or eliminate limitations imposed by the atmosphere of the Earth. The Perkin-Elmer solar telescope, shown in figure 3, was carried to altitudes in excess of 80 000 feet during Project Stratoscope I, 1957 to 1959, conducted for the Office of Naval Research. This system incorporated a 12-inch-aperture telescope having an effective focal length of 2400 inches and a rotating secondary mirror and relay lens system designed to overcome the effects of the hot solar image. An example of the resolution obtainable with such a system is shown in the sample sunspot photograph in figure 4, where 1 mm corresponds to 0.4 second of arc or about 190 miles.

Since the visible spectrum covers only a small percentage of the total energy radiated from any object, sensing in other frequency bands

may be instructive. The results of several solar scans from ground-based radiometer systems, operating at wavelengths from 4.3 mm to 10.4 cm (ref. 2), is shown in figure 5. The information contained in the various electromagnetic regions is clearly different, emphasizing the importance and usefulness of multispectral data. Scans of the active Sun at a wavelength of 3.15 cm, taken with the 50-foot antenna of the U.S. Naval Research Laboratory on May 1, 1956, are depicted in figure 5(a). A graph of the solar outburst of June 9, 1959, at a wavelength of 4.3 mm is shown in figure 5(b). The results of the scans of the active Sun at a wavelength of 3.2 mm taken on August 12 and 13, 1964, are given in figure 5(c). The solar outburst flux curves for December 1, 1959, at wavelengths of 4.3 mm, 3.15 cm, and 9.4 cm are shown in figure 5(d).

Although photography has provided the bulk of immediately usable data concerning the Moon, investigations of the lunar surface have not been limited to the optical range. Information obtained from radar systems operating at several different wavelengths has indicated that most of the lunar surface is generally smooth, with only about 10 percent of the area covered by objects creating surface irregularities on the order of 1 meter or more (refs. 3 and 4). Light-scattering measurements have also been made in an effort to obtain a more complete knowledge of the lunar surface (ref. 5). Conjectures about surface composition and history, based on similar data and experimentation, are included in references 6 and 7 and in many other reports.

The success of the Ranger, Surveyor, and Lunar Orbiter spacecraft series in obtaining high-resolution photographs of the lunar surface has contributed to the beginning of the necessary mass of selenographic data on which a relatively complete understanding may be based. Several of the photographs obtained by these and similar vehicles have been previously published; however, it is felt that their inclusion in this paper may illustrate the usefulness and the state of the art of remote photographic imagery in the space environment.

Figure 6 was taken from an altitude of 1000 feet above the lunar surface by a P-3 camera carried onboard the Ranger 7 spacecraft. The smallest craters shown in this photograph, which covers an area of about 60 by 100 feet, are about 3 feet in diameter and 1 foot in depth. The spacecraft impacted while transmitting this photograph, resulting in the -receiver noise pattern on the right side.

A full-scale mockup of the Surveyor I spacecraft, the first U.S. lunar soft-lander, is shown in figure 7. This vehicle touched down on the lunar surface at 11:17 p.m. (P.d.t.), June 1, 1966, and began transmitting pictures similar to that which is shown in figure 8. This 600-scanline photograph, received at the Jet Propulsion Laboratory on June 2, 1966, shows a small rock approximately 6 inches high and 12 inches

long. The TV camera used to take this photograph is illustrated in figure 9; its position on the vehicle itself is shown in figure 7 to the left of the center of the photograph.

The relative location of Surveyor I on the lunar surface was verified on February 22, 1967, when the Lunar Orbiter III spacecraft took the three views shown in figure 10. The oblique shot (fig. 10(a)) was taken by the wide-angle lens system at an altitude of 30 miles and at a slant range of 82 miles to the center of the photograph. The crater Flamsteed can be seen at the southern tip of the partial ring structure in Oceanus Procellarum.

The photograph in figure 10(c) is an eight-times enlargement of the center view (fig. 10(b)), taken at an angle of about 12° off vertical. The Surveyor spacecraft resting on the lunar surface can be seen within the white ring as a white object casting a shadow approximately 30 feet long. Its position was previously identified by triangulation of distant objects focused on the horizon by the camera of the Surveyor I. These data points are shown as radial lines in the photograph on the left.

Figure 11 shows a closeup of the crater Copernicus, taken by the telephoto lens of the Lunar Orbiter II on November 23, 1966. The mountains shown in this photograph rising from the crater floor are 1000 feet high. The 3000-foot peak at the upper left is the Gay-Lussac promontory in the Carpathian Mountains. Figure 12 covers an area of about 25 by 30 miles on the floor of the crater Hevelius on the western edge of Oceanus Procellarum. This photograph was taken directly above the crater from an altitude of 38.5 miles. Figure 13 shows the northern portion of Oceanus Procellarum and an area known as the Cavalerius Hills. The largest crater shown is Galilei, which is about 10 miles across and over a mile deep. Contained in this photograph, centered at 64° 34' west, 7° 00' north, is the landing site of the U.S.S.R. Lunik IX spacecraft, which landed on the Moon on February 3, 1966. In figure 14 is shown an area between Mare Sirenum and Mare Cimmerium on the surface of the planet Mars, taken on July 14, 1965, from an altitude of approximately 6000 miles by systems onboard the Mariner IV vehicle. North is at the top of the photograph. The location is further defined in figure 15, which is a standard representation of Mars. Figures 6 to 15 are official photographs furnished by the National Aeronautics and Space Administration (NASA).

Other sensors onboard interplanetary and deep space probes, as well as on Earth-orbiting satellites, have greatly expanded our knowledge about our outer environment and the physical processes and phenomena occurring there. Since astronomers now have the ability to conduct observations from a viewing platform stationed above the Earth's atmospheric mantle, measurements of undistorted optical and electromagnetic radiation can provide new information on how stars evolve, on the makeup of interstellar gas, and on the existence of stellar atmospheres. Measurements

in the X-ray and ultraviolet bands, conducted above the ozone and molecular-oxygen-absorption layers, have already caused the modification of several theories (ref. 8).

The general aspects of the problems involved in the remote sensing and analysis of interstellar gas, cosmic rays, magnetic fields, and energetic particles, and in the communication and data-processing requirements have been discussed at length in references 9 to 12.

The Explorer I satellite, launched in January 1958, provided data on the extent of the inner Van Allen belts. Subsequent vehicles in the Pioneer, Lunik (U.S.S.R.), Explorer, and Relay satellite series, as well as Elektrons I and II (U.S.S.R.) and Ariel II (U.S./U.K.), have provided information on micrometeoroids, on solar and galactic shortwave radio propagation, on the energy and distribution of trapped particles in the geomagnetic field, and on solar-wind velocity, temperature, energy, and density (refs. 13 to 19). The Mariner IV vehicle, launched in 1964, has also provided information concerning the outer magnetosphere of Mars and has provided a measure of the intensities of trapped particles in this region (ref. 20). In the future, automated spacecraft, such as the advanced Mariner and Voyager systems planned for the early 1970's, will obtain direct measurements of the physical and chemical properties of the Mars and Venus atmospheres during fly-by and soft-landing missions. A Jupiter probe has also been proposed to gather data on the magnetosphere and ionosphere of that planet (ref. 21).

A diagram of some of the phenomena of interest in the Earth-Sun system is shown in figure 16 (ref. 10). Figure 17 is a graphic summary of several solar-wind experiments, showing spacecraft trajectories in Earth-Sun coordinates (ref. 14).

THE INTERVENING ATMOSPHERE

When remote sensing of extraterrestrial objects or occurrences is to be accomplished from the surface of the Earth, or when Earth reconnaissance is to be accomplished from altitudes above the surface of the Earth, the composition and nature of the intervening atmospheric medium and its distortion effect on data must be considered. In this regard, the medium itself may be the target of remote investigation.

Figures 18 and 19 depict the 1964 U.S. standard atmosphere properties from sea level to an altitude of about 400 miles. This reference atmosphere, however, provides a seriously inadequate description of properties and variations above 60 miles. It is primarily in this area that new and continuous information is desired (refs. 22 to 24).

In addition to instrumented balloons, high-altitude aircraft, such as the U-2 (fig. 20), the RS-70 (fig. 21), and the SR-71 (fig. 22), equipped with a variety of multipurpose research and reconnaissance sensors can provide data concerning the various atmospheric properties in the sea-level to 15-mile altitude regime. Rocket-powered research aircraft, such as the X-15 (figs. 23 and 24), can conduct basic research and direct observations at altitudes up to 60 miles. Sounding rockets are the primary research tools in the 60- to 120-mile region, with satellites such as the Essa, Tiros, and Nimbus series being the prime data sources above this point (refs. 25 to 27).

Ground-based spectrometers and photometers (ref. 28), ionospheric radio sounding systems (ref. 29), and high-altitude gun-launched projectiles (refs. 30 and 31) have provided much usable data on upper-atmosphere composition, wind velocities, temperatures, densities, and the formation of sporadic E layers. However, in this middle-altitude regime, sounding rockets, such as those in figures 25 and 26, continue to supply the bulk of information presently available in these areas, including data concerning solar and ultraviolet radiation, cosmic-ray activity, airglow, and the aurora (refs. 32 and 33).

The primary measurement techniques employed with sounding rockets involve the use of plasma probes, such as the Langmuir or the Gerdien Condenser probes (refs. 34 to 36), and artificially-created chemical clouds. In the conventional Langmuir probe as shown in figures 27 and 28, an electrode on the insulated nose tip of the rocket is experimentally inserted into the plasma region where the current to it is determined as a function of the potential of the electrode. From the resulting current-voltage characteristics, the electron energy distribution, the temperature, the density, and the fine structure may be obtained (refs. 30 and 37). As stated in reference 30, the use of the Langmuir probe technique for temperature measurements is limited to altitudes above 85 kilometers, since below this point "electron collisions with the neutral gas particles cannot be neglected, and negative ions may be present in significant numbers."

Rocket release of gas clouds, the "vapor trail" technique, has been shown to be highly successful in the measurement of winds, atmospheric density and composition, temperature, and in determining the characteristics of radio-wave reflections at altitudes between 80 and 200 kilometers. In measuring wind and diffusion profiles the release of vapor, typically sodium, trimethylaluminum, or potassium, is photographed by several ground-based narrow-filter cameras which provide, by triangulation, relative position data and a time history of cloud development and movement. High-resolution photometers, spectrometers, and interferometers are used to measure spectral profiles from which temperature and density information may be obtained (refs. 28, 32, and 37 to 40).

One major limitation on the use of these techniques is the requirement for clear weather simultaneously over several remote observation sites. In areas of high cloud concentration and where weather-forecast information is limited, such as at the Fort Churchill Rocket Research Range, Manitoba, Canada, this constitutes a primary launch constraint. A map of the range, figure 29, shows the relative positions of the launch and observation sites located at Eskimo Point, Seal River, Twin Lakes, Digges, Belcher, and O'Day.

In September of 1966, a P-3A aircraft (fig. 30), operated by the NASA Manned Spacecraft Center, was equipped with photometer and spectrometer systems and several cameras. The aircraft was then flown as a high-altitude observation platform during a series of rocket launches at the Fort Churchill range. This allowed measurements to be made above constraining weather conditions and from any of several directions. Sensor systems are shown in figures 31, 32, 33, 34, and 35. Figure 36 shows a sequence of photographs of a typical trimethylaluminum (TMA) gas release and subsequent wind distortion observed during this mission.

Simultaneous probe and vapor-trail data have been used in the investigation of regions of sporadic E. It has been shown (ref. 38) that these regions are not located at the zero point of an east-west shear as was originally predicted by the "wind shear" theory, but are usually closely associated with sharp directional changes in a plotted wind hodograph. As an illustration, an electron density profile, a wind profile, and a plotted hodograph from a Nike-Apache shot at Wallops Island, Virginia, in October 1964, are shown in figures 37, 38, and 39 (ref. 37).

A unique radar system operated by the Air Force Cambridge Research Laboratory in Bedford, Massachusetts, has also been used in the determination of upper-atmosphere density and winds. In this system, operated at frequencies of 36.8 and 73.6 MHz, radar signals are reflected from the ionized trails of entering meteors, and the data are processed to obtain range, altitude, and signal strength information. The rate of decay of signal strength reflected from the trail is proportional to the rate of diffusion of the ionized particles, which is, in turn, inversely proportional to the atmospheric density (refs. 32 and 41). A similar system developed for the Smithsonian Astrophysical Observatory is presently being evaluated at a site in Havana, Illinois.

At the lower altitudes, radiosondes, weather balloons, and remote-sensor-equipped aircraft provide the majority of meaningful data. In addition to the more conventional instrumentation, laser, infrared, and sounding-balloon/radiosonde-accelerometer systems have been employed in air-turbulence and turbidity investigations, an area of significant importance in aircraft operation and high-altitude photography (ref. 42).

As the amount of atmosphere between the target area and the remote sensing system is increased, transmission of emitted or reflected energy is decreased. The two curves in figure 40 show transmission percentages at various wavelengths at sea level and at an altitude of 30 000 feet. These curves will be somewhat modified as meteorological conditions change.

In addition to its absorption properties, the atmosphere exhibits Rayleigh, Raman, and Mie scattering. Since most Mie particles, the sizes of which approximate the wavelength of visible light (for example, water particles, dust, smoke, and similar aerosols), are restricted to altitudes below 15 000 feet, a predominantly Rayleigh atmosphere composed largely of nitrogen and oxygen gas molecules may be postulated above this point. For most photographic purposes, the effective scattering atmosphere lies below about 30 000 feet (refs. 43 and 44). Extraterrestrial objects which are viewed in the visible range are then most appropriately examined from altitudes in excess of 30 000 feet.

Atmospheric turbulence must also be considered because of its effect on image quality, typically in photographic systems. This is seen as scintillation or time variation of image intensity, image position, and image size. As stated by J. D. Clarke in reference 45, when viewing celestial targets from the Earth, "these effects can be reduced from as much as 3 arc seconds of apparent motion at ground level to less than one-half arc second at 40 000 feet." High-frequency scintillation effects are mostly due to wind shear at the top of the troposphere; however, as reported by F. Gifford, Jr., in reference 46, some low-frequency (1 to 10 Hz) scintillations have been observed as high as 100 000 feet.

THE ENERGY ENVIRONMENT

Before discussing the third major area of interest, sensing of the Earth from aircraft and orbital altitudes, the basic equations and energy considerations involved in remote sensing in the electromagnetic spectrum should be reviewed briefly.

. At any temperature above absolute zero, all objects radiate electromagnetic energy because of their atomic and molecular oscillations and absorb and reflect a certain amount of impinging energy as a function of their composition and surface condition. All objects are characterized by a specific spectral signature, or by the manner in which they emit, absorb, and reflect radiation. Therefore, it should be possible to distinguish among various objects on the basis of these spectral characteristics and also to obtain some information pertaining to relative size, shape, and other physical and chemical properties. This is essentially the same process used in visual discrimination. In addition, all matter tends to reach thermal

equilibrium in relation to its surroundings, a condition in which equal amounts of energy are absorbed and radiated. Since the amount of incoming energy is usually time variant (such as in the diurnal cycle), most objects exhibit emittance and absorption rates which also change with time. These heating and cooling rates are a function of the basic material and of its surface characteristics and, therefore, provide an additional means of differentiating between objects or classes of objects.

Remote sensing of electromagnetic radiation (ref. 47) is basically a problem of determining interactions between particulate energy and particulate matter. Since electromagnetic waves do not interact among themselves, all energy changes in radiant photons must be caused exclusively by interactions with matter.

A useful concept in energy interaction is that of a "black body," or a body which, by definition, exhibits zero reflectance. For such an object, the radiant emittance equals the radiation power incident on a unit area of surface (irradiance). An object so described is said to have an emissivity or radiating efficiency factor E equal to unity and emits radiation in a continuous spectrum with the wavelength of peak emission dependent on the temperature of the source.

Planck's distribution law, derived from his hypothesis of the energies of elemental oscillators, states that the energy emitted at a particular frequency is proportional to a constant.

$$E_\lambda = \frac{c_1 \lambda^{-5}}{e^{c_2/\lambda T} - 1} \tag{1}$$

where E_λ = spectral radiance or spectral radiant emittance

e = the base of natural logarithms, 2.718

T = temperature of black body, °K

$c_1 = 2\pi hc^2$, where Planck constant h equals 6.6252×10^{-34} J/sec and c equals the velocity of light in a vacuum, 3.0×10^8 m/sec

$c_2 = \frac{hc}{k}$, where k is the Boltzmann constant, 1.3805×10^{-23} J/°K

The Stefan-Boltzmann law states that the total radiant emittance of a black body per unit area per unit time is proportional to the fourth power of the absolute temperature.

$$E = \sigma T^4 \tag{2}$$

where σ = the Stefan-Boltzmann constant, 5.6687×10^{-8} watts$/m^2/°K^4$

T = temperature, $°K$

This energy is distributed along a skew curve as shown in figure 41 with 25 percent of the total power radiated from the source appearing in the high-frequency end of the spectrum to the left of the radiation peak in figure 41.

The wavelength or frequency at which maximum radiation occurs is found from the Wein displacement law:

$$\lambda_{max} = \frac{K}{T} \tag{3}$$

where $K \simeq 2.897 \times 10^3$ for a black body yielding λ_{max} in microns. It is seen from this relationship that as the temperature of the body increases, the peak of the radiant energy shifts toward higher frequencies. This is illustrated in figure 42.

Most naturally-occurring objects are less perfect radiators than the hypothetical black body since incident energy will be partially absorbed, partially reflected, and partially transmitted.

$$E_i = E_\alpha + E_\rho + E_t \tag{4}$$

where E_i = incident radiant energy

E_α = absorbed energy

E_ρ = reflected energy

E_t = transmitted energy

An equation may now be written relating the characteristics of any "gray body."

$$\alpha + \rho + t = 1 \qquad (5)$$

where α = absorptivity; the fraction of the incident radiation
absorbed by the object

ρ = reflectivity

t = transmissivity, or that fraction transmitted through the
object

For an opaque object $t = 0$,

$$\varepsilon = \alpha = 1 - \rho \qquad (6)$$

where ε, the emissivity, is then a function of the material, its surface,
temperature, and the wavelength of incident radiation. An object with
a high reflectivity is then characterized by a correspondingly low absorp-
tivity and emissivity, while an object that is only slightly opaque will
have a low reflectivity and emissivity. For most materials, emissivity
varies directly with temperature and inversely with the wavelength of the
incident radiation.

If remote sensing of some target area is conducted through an inter-
vening medium, such as the Earth's atmosphere, severe limitations in terms
of spatial and spectral range may be imposed. Although large portions
of the electromagnetic spectrum are effectively blocked by scattering and
absorption, several "windows" do exist through which remote reconnaissance
is possible. Some of the more significant of these are shown in figure 43.
Table I lists the primary absorption bands between wavelengths of 30 Å
and 10 cm, and figure 44 depicts the sensor systems most frequently employed
in remote reconnaissance across the electromagnetic spectrum and their areas
of peak effectiveness.

The radiation curve of the Sun approximates that of a black body at
6000° K. Large amounts of energy are radiated across the ultraviolet, visible,
and infrared spectral bands, with a peak at about 0.5 micron. Therefore,
remote sensing in reflected light may be accomplished easily in the 0.4- to
0.75 micron range with conventional films and camera systems. The Earth,
with an average temperature of 300° K, has a radiation power peak at about

9.6 microns. Remote sensing of emitted energy may then be conducted in the 8- to 14-micron window.

More complete reviews of the interactions between energy and various materials are presented in references 47 to 49 and in other references from which this material was drawn. From this brief summary, however, as stated by R. N. Colwell in reference 50, it is seen that "transmission, reflection, absorption, emission, and scattering of electromagnetic energy by any particular kind of matter are selective with regard to wavelength and are specific for that particular kind of matter, depending primarily upon its atomic and molecular structure." If information concerning these various parameters can be gathered remotely, then the object under investigation may be completely specified.

THE INNER ENVIRONMENT

While the future of man may lie among the stars, his present is tied to the Earth. If he is to expand and explore the surrounding universe, he must more fully understand this Earth on which he lives and expand his knowledge and use of the resources available. Almost all scientific disciplines focus to some degree on the processes and morphology of the Earth, its cultural and physical resources and characteristics, its past, and its future. In these fields, remote-sensing systems may find their widest area of application. Utilization of the technologies and capabilities developed through the space programs of the nation for geophysical reconnaissance and surveillance represents an early and significant return on the space investment dollar. When installed on orbiting space platforms, these systems will provide continuous and synoptic data over any point on the Earth surface. Multisensor-equipped aircraft can carry out similar typical missions in the lower altitude regime. Table II lists several typical sensors and the various scientific areas in which they may be employed.

Visual Spectrum

Aerial photography is perhaps the most familiar and widely used remote-sensing technique. Presently available film and filter combinations cover a spectral range of approximately 290 to 900 millimicrons, which includes the area of peak reflected energy from the Earth surface. Blue end cutoff is largely a function of the glass optics employed in the camera, while cutoff in the near infrared is determined by the sensitivity of the film employed (refs. 51 and 52). Because of the similarity of data presentation between cameras and the human eye, aerial photography usually provides the most accurate and easily interpretable data concerning size, shape, and relative position of objects in a target area.

Ground coverage of a standard framing camera, such as the Wild--
Heerbrug RC-8 or the Aeroflex KC-3, may be calculated as

$$C = \frac{WH}{F}$$
(7)
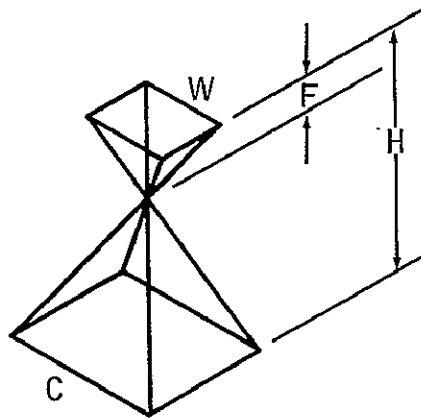
where C = ground coverage, ft

W = width of film format, in.

H = altitude above terrain, ft

F = focal length, in.

Ground resolution is determined by

$$R = \frac{H}{F(LFR)25.4}$$
(8)

where R = ground resolution, ft

H = altitude, ft

F = focal length, in.

LFR = lens-film resolution, lines/mm

The techniques of aerial photography were developed primarily by the British during World War I, and use in scientific endeavor followed. One of the first applications was in geological mapping for petroleum exploration in the Oklahoma City oilfield in 1928. By the 1930's, surveys were being made in remote geographical areas such as Dutch New Guinea and northern Australia, where surface access was difficult or impossible (ref. 53). Today, photography from orbital altitudes has provided previously unobtainable data. Figure 45 shows the entire Sierra del Pinacate volcanic field, located in Sonora, Mexico. Prior to this photograph, taken by the crew of Gemini IV, the full extent of this field was not known. The Agua Blanca Fault Zone, first discovered by geologists in 1956 from aerial-reconnaissance photographs, is immediately recognizable in space photographs. Figure 46 covers part of the Edwards Plateau-Staked Plains interface in central Texas. The basic geologic characteristics of these areas are clearly defined, and oil production areas may be plotted. This photograph is a striking example of geologic definition which cannot be obtained from ground- or low-level imagery.

Oceanographers have also benefited from the macroscopic view of orbiting cameras. Bottom topography and sediment distributions have been identified, and a limited amount of depth mapping has been accomplished from data acquired by Mercury and Gemini astronauts. Figure 47 is a photograph of the Great Bahama Bank, Bahama Islands, taken from the Gemini IV spacecraft. The light area to the right is shoal water bordering the island group, while the darker area represents deeper water. Figure 48, taken from Gemini V, shows this same general area in a more oblique view. Bottom details are clearly visible. The dark object in the lower right-hand corner is the nose of the spacecraft. As an adjunct to weather-surveillance satellites, conventional photography from manned space vehicles may be of value in terms of the ability to selectively view areas of interest. Figure 49, also shot during the Gemini V flight, shows the clockwise circulation pattern of a South Atlantic tropical storm forming behind Hurricane Betsy. Another example of space weather reporting occurred when, on this same mission, Astronauts Cooper and Conrad reported Hurricane Doreen in mid-Pacific during their 65th revolution. At this time, ground weather stations had no information concerning the location of the storm center. This information was transmitted to the ground, and the weather bureau in San Francisco published an advisory to sea and air traffic the same day.

'Multispectral or spectrozonal photography has been employed in many areas in an attempt to obtain data not readily apparent in a single photograph covering a broad spectral range. As pointed out by Colwell in reference 54, two or more objects may reflect exactly the same amount of energy in a given frequency band. When this occurs, they cannot be differentiated on the basis of color tone in a photograph which covers only this band. If simultaneous photographs can be taken in adjacent spectral regions, however, the objects may be distinguished since it is unlikely that they will reflect the same amount of energy in all bands.

The following graph shows the approximate reflectance characteristics of grass, concrete, soil, and asphalt (ref. 54).
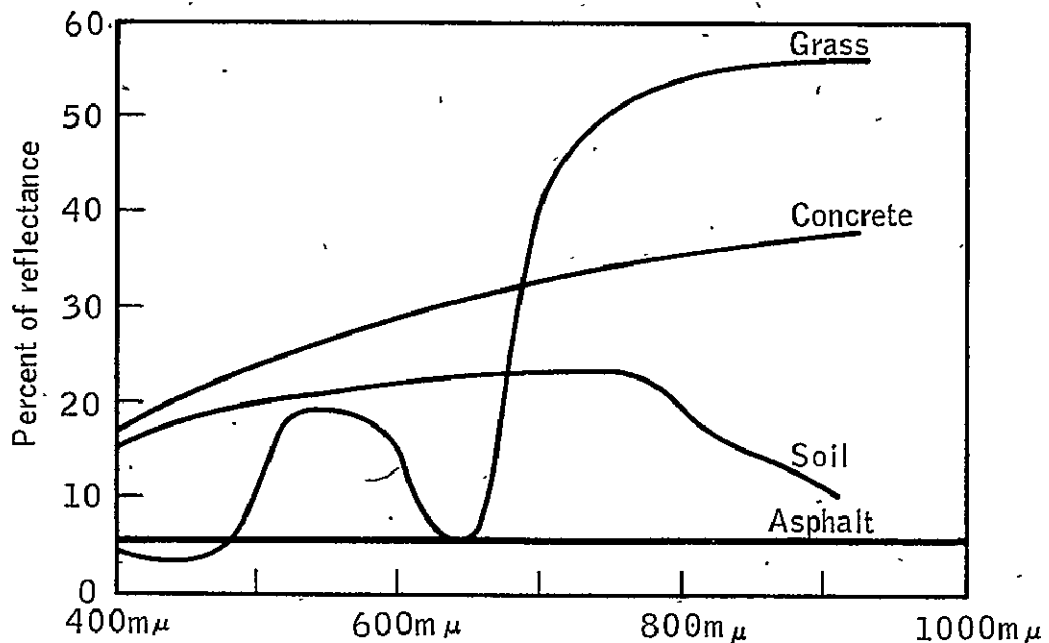
If a photograph of a grass-asphalt interface is taken in the 600- to 700-millimicron band, the two materials may be indistinguishable; however, if concrete or bare soil are present, a difference will be readily apparent. If the imaging band is shifted by a proper selection of film/filter combinations to the 700- to 800-millimicron band, grass may be easily separated from asphalt areas.

Similar differences in reflectance between normally healthy and diseased vegetation may be detected through multispectral analysis, often before such differences become visually apparent to a ground observer (refs. 47 and 55). It has been shown that various species may be distinguished through proper application of this technique, and information

regarding leaf size, age, and moisture content may be obtained (refs. 56 to 58).

High-altitude photography and multispectral analysis has also been applied in glaciological studies (ref. 59). Figure 50 is a contour map of the South Cascade Glacier in the North Cascade Range, Washington. Figure 51 is an oblique aerial photograph of this glacier, looking southeast, taken in 1965 by Austin Post, U.S. Geological Survey. Figure 52 is a vertical photograph taken by an RC-8 camera with color film at an average altitude of 4000 feet above the glacier surface. The photograph in figure 53 was taken a few minutes later with the same systems, using infrared color film. The increase in textural detail, particularly in the moraine areas, is quite evident in the infrared photograph, while the color photograph is less hampered by shadowed areas and crevasses.

Although multispectral photography may be accomplished with a single optical recording system by changing film and filters during repeated overflights, several cameras may be ganged and their shutters activated simultaneously to reduce the time spent over a particular area. This also allows the exposure of the same target in all bands under identical conditions. One unique system, developed by the Itek corporation, incorporates nine lens/filter systems in one camera body (fig. 54). Photography is accomplished simultaneously on three film paths, and by proper selection of film/filter combinations, selective sensing may be accomplished across the entire visual spectrum and beyond. Figures 55 and 56 depict the physical layout of the film paths and the narrow-band transmission curves of the various filters employed.

Infrared

Infrared is the generic term applied to that portion of the electromagnetic spectrum between the visible and microwave regions. This area has been rather arbitrarily divided into three regions: (1) near infrared (0.7 to 1.35 microns), (2) intermediate infrared (1.35 to 5.5 microns), and (3) far infrared (5.5 to 1000 microns). Certain types of photographic emulsions are capable of recording radiation out to approximately 0.9 microns, but beyond this point, "infrared detector" sensors must be employed.

Like cameras, infrared imagery systems are passive in nature. Received energy is focused by a lens or reflective optical system onto a sensitive detector. The output of this sensor is then a function of changes in total received energy in a particular frequency band. This output may be recorded on strip-chart or on magnetic tape recorders, or may be used to modulate the intensity of a light source. This varying light may then be used to expose standard photographic emulsions, yielding a picture very similar to that provided by low-resolution photography. Unlike conventional pictures, however, the light and dark tonal contrast is now a function of energy emitted from the target area rather than of reflected light

controlled primarily by surface characteristics. Since reflected light is not required, remote sensing may easily be accomplished at night, yielding data which may be presented in a form similar to daylight photography.

Again, as in conventional cameras, short-wave-pass, bandpass, and long-wave-pass filters may be added to isolate certain wavelength regions of interest or to screen out undesired wavelengths. When infrared systems are operated under daytime conditions, a certain amount of reflected light may also be recorded because of the spectral sensitivity range of standard detectors. Thus, if only emitted energy is of interest, a filter may be inserted to block all wavelengths shorter than about 760 millimicrons. Some systems also incorporate chopping reticles and mirrors in the principal focal plane. This may be used to provide a reference point for calibration and data analysis or to generate a higher carrier frequency for electronic amplifiers.

While the spectral resolution of an infrared system is determined by the detector employed, the spatial resolution is a function of the cone angle of the sensor. As this becomes smaller, given levels of energy may be more easily associated with specific objects. If a map is to be generated, this scanning spot is swept laterally across the ground track as the carrier vehicle moves over the target area. Figure 57 shows the resultant ground-coverage pattern and a typical video waveform generated by a single scan. A schematic representation of an infrared system employing reflective optics is shown in figure 58. Contiguous line scanning is an obvious requirement here if the total coverage is to be obtained. While this may be accomplished by varying the speed with which the image spot is moved across the terrain as the aircraft changes altitude or velocity, it is more practical to vary the speed with which film is moved past the modulated light source. A velocity-height function is fed manually or automatically from Doppler radar systems to a servo system which controls the film drive speed. At high altitudes and low airspeeds, the film velocity must be extremely slow and accurately maintained.

In addition to the distortion near the edges of the film, caused by a greater distance traversed on the ground per degree rotation than at the center, objects also are printed in reverse because of the scan geometry.

Direction of flight
and film

Scanner rotation

Printer direction

Film
motion

Scanner
direction

Emulsion down
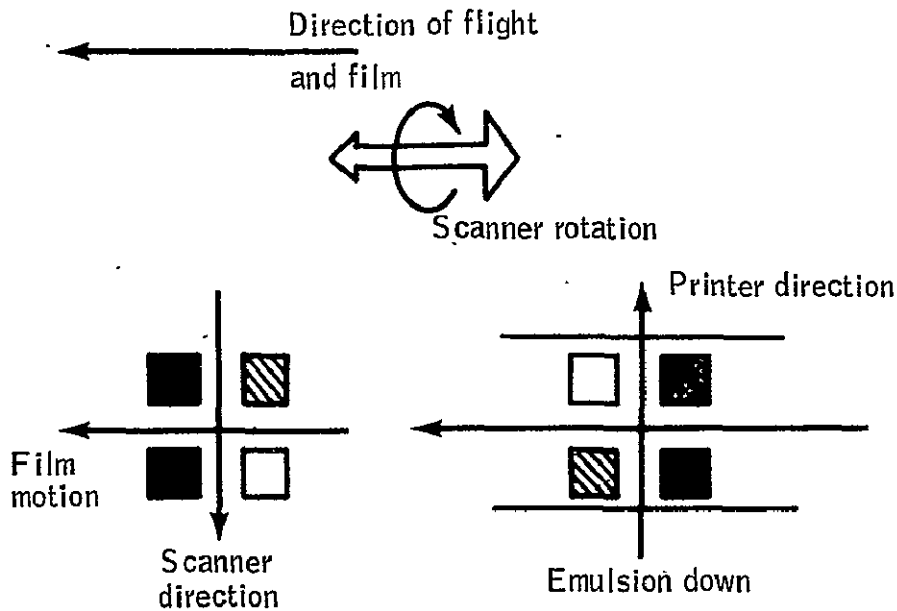
If film is transported opposite to aircraft motion, reverse printing may be required.

The heart of any infrared system is the detector. This is carefully chosen to match the system requirements, the operating environment, and the information requirements of the user agency. These units may be separated into two groups, based on operation principles: (1) thermal detectors and (2) photodetectors.

Thermal detection is accomplished by sensing a change in temperature of the detector material when energy impinges upon it. Three different techniques may be employed: (1) thermopiles, a series combination of several thermocouples; (2) bolometers, which sense resistance changes in the detector; and (3) pneumatic cells, which sense the expansion of a gas as a function of received energy. Although thermal detectors will respond to wavelengths up to approximately 14 microns without cooling, they require more incident radiation than photodetectors to produce an equivalent output signal and may not be as responsive to small changes.

Photodetectors use the photon energy of infrared radiation to change some electrical property of the detector material; they may be classified as photoconductive, photovoltaic, and photoemissive systems. These units normally require cooling to liquid nitrogen or to liquid helium temperatures to reduce energy interaction with the detector enclosure, and to improve the signal-to-noise ratio.

Characteristic sensitivity curves for several infrared detectors are shown in figure 59. The mercury-doped germanium detector (Ge:Hg), operated at temperatures below 35° K, is the unit most commonly employed for sensing in the 8- to 14-micron atmospheric window.

Figure 60 shows two typical strips of unclassified infrared imagery urban-rural interface area. The map on the left, taken at a higher altitude, shows land use and general drainage patterns. On conventional photography, the stream seen here would be generally obscured by vegetation. The strip on the right contains increased geologic detail in the stream area, and differences in vegetation and tree types become apparent. The distortion of the imagery, most evident in the false curvature of roads near the edges of the film, is a function of the scan geometry.

Shown in figure 61(a) is an infrared image of the Meadow Valley area near Quincy, California. The arrow marks the contact point between the lighter-toned serpentine intrusion and the surrounding Quaternary sands. These are relatively indistinguishable in visual-range photography. Shown in figure 61(b) is an area of subsurface drainage near Walley's Springs, Nevada. Unusual thermal patterns resulting from subsurface drainage are indicated by arrows.

Similar reconnaissance and analysis has been conducted in the Kilauea Volcano area, Hawaii. Structural details of the volcano, not evident from surface observations, have been plotted from temperature-contrast data, and some correlation has been found with later sites of volcanic eruption (ref. 60).

Ocean currents and underwater thermal anomalies are also readily apparent in infrared imagery. Shown in figure 62(a) are thermal gradients analogous to drainage patterns in a lake near Walley's Springs, Nevada. The arrow indicates the positions of thermal gradients in the lake caused by the entrance of turbid stream waters. A very obvious anomaly in the Salton Sea, California, is shown in figure 62(b). The underwater thermal anomaly is indicated by the arrow.

Infrared technology has also been applied in the aerial detection of snow-bridged crevasses (ref. 61). Figure 63, furnished by the U.S. Army Cold Regions Research and Engineering Laboratory (CRREL), compares conventional photographic data with infrared imagery acquired under night and daytime conditions. The crevasses, warm lines on the infrared strip maps, show considerable contrast with the snow background. As reported in reference 61, ground investigations in this area confirmed that these lines did, in fact, represent the thermal patterns of crevasses.

. The relative location, type, and thickness of sea ice are important factors affecting international commerce and have obvious military applications in Arctic and Antarctic operations. Infrared sensing, with its night operation capability, has been demonstrated to be of significant value in these areas (ref. 62).

Figures 64 and 65, obtained in April 1962 and January 1964 by CRREL, illustrate this capability. In figure 64, most of the ice shown is thin

winter ice with little or no snow cover. Finger-rafting, characteristic
of ice of this type, is seen as light tone bands crisscrossing the area.
The infrared data show a marked reversal in photograph tone from the more
conventional photography. The very thin ice, which appears dark gray in
the photograph and light gray in the infrared imagery, indicates a warmer
surface. The snow-covered thicker ice, white in the photograph and black
in the thermal map, is substantially colder because of the insulation ef-
fect of the snow surface.

In figures 65(a) and 65(b), obtained under Arctic-night conditions,
ice thickness varies from 4 to over 12 feet as reported by ground parties.
Polar-pack ice shows a darker, colder tone and a characteristic pressure-
ridge pattern on the larger areas. The thinner winter ice varies from a
smooth surface to areas with shallow pressure ridges.

Airborne radiation thermometers operating in the infrared region have
also been used to determine sea-surface temperature (ref. 63). Accuracies
of ±0.4° C have been reported. Figure 66 is a photograph of a unit in-
stalled in the Antisubmarine Warfare Environmental Prediction Service air-
craft. A data sample obtained over the Gulf Stream in March 1963 is shown
in figure 67. The aircraft itself, a modified C-121 operated by the
U.S. Naval Oceanographic Office from the Patuxent River Naval Air Station,
Maryland, is shown in figure 68.

Passive Microwave

Atmospheric absorption of energy at wavelengths between 25 microns and
1 mm severely limits remote measurement operations in this band. Beyond
this point, microwave-radiometric techniques may be employed.

The purpose of any radiometer is to accurately measure the amount of
power radiated by an object. Since the energy contained in the microwave
portion of the spectrum for any given radiating body is usually about four
orders of magnitude less than that at visible or infrared frequencies, much
longer integration times are required. These are typically on the order of
1 second or less. As pointed out in reference 64, the brightness tempera-
ture of the target is affected by its thermometric temperature, emissivity,
reflectivity, and physical state as well as by the wavelength of observa-
tion. Also, for all materials except metals, there is a difference between
the vertical and horizontal polarization apparent temperatures (ref. 65).
Figure 69 shows the variance of emissivity of sea water with incidence angle,
temperature, and polarization at a wavelength of 21 cm (ref. 52).

Microwave frequencies are relatively unaffected by atmospheric mois-
ture, and thus, provide a remote-sensing capability through regions of
dense fog or clouds. This is of increased significance in Arctic opera-
tions. Since ice is highly absorbent at these frequencies, it is easily
differentiated from surrounding water.

Figures 70 and 71, furnished by the CRREL, illustrate this capability. These data were obtained off the coast of Labrador in April 1966 from the NASA Manned Spacecraft Center CV-240A aircraft. The radiometer systems (fig. 72) were mounted in the nose of the aircraft and operated at frequencies of 9.2, 15.8, 22.2, and 34.0 GHz. Outputs were recorded simultaneously on a dual-trace strip-chart recorder and on magnetic tape for subsequent analysis. The correlation photographs shown at the top of figures 70 and 71 were taken with the 6-inch-focal-length RC-8 cartographic camera.

As reported by A. O. Poulin of CRREL in September 1966, in addition to the magnitude of the apparent temperature differences shown in the figures, the data traces have shapes which appear to be characteristic of the physical condition of the ice and water. The curvature for the first centimeter on the charts after transition from ice to water or from water to ice is primarily due to the response time of the radiometer. The traces, however, show evidence of slope prior to this interface, particularly at 15.8 GHz. This change, quite evident in figure 71, is at least partially attributable to a decrease in average ice thickness as open water is approached. The data in figure 70 seem to indicate a lack of gradient ice in the flow shown on the right.

As a supplement to line-scanning radiometers, attempts have been made to generate strip maps at microwave frequencies with passive systems. One such system operates in the 9.1- to 9.7-GHz region. In the planar array antenna, 54 slightly dispersive leaky wave line sources are fed from opposite ends by two highly dispersive helical lines. This design produces two independent symmetrical beams 90° apart. Waveguide directional couplers couple the energy from each helix to the array of line sources and adjust the amplitude distribution to decrease side lobes. The receiver section is a square-wave switched Dicke comparison type which permits absolute temperature measurements as energy is sampled across the beams. The receiver outputs from the fore and aft beams modulate the intensity of two cathode-ray tubes which are, in turn, recorded on film, generating a radiometric map of the overflown terrain. Figures 73 and 74 are an illustration of the general beam geometry. Figure 75 shows the antenna installed in the bomb bay area of a NASA P-3A aircraft, and figure 76 shows the cathode-ray tube/map-matcher unit and systems control panel.

Active Microwave

Active microwave sensors have also been utilized in geoscience research. One of the first applications occurred in 1947 when a map of the northwestern coast of Greenland was constructed using a plan position indicator (PPI) radar (ref. 66). At the present time, radar systems are widely used in meteorology and climatology to provide cloud-height information, rainfall-intensity estimates, maps of severe weather cell activity and so

forth. Of particular interest to the Earth scientist is the inherent ability to provide data also on surface roughness, soil composition, and degree and type of vegetation cover under all weather conditions.

As employed in remote geophysical sensing, radar systems may be classified as imaging or scattering systems. Imaging radars are those which produce a pictorial representation of the target area, such as the brute-force (real-aperture) or the synthetic-aperture side-looking systems. Scatterometers, or scattering radars, measure the magnitude of the radar backscattering cross section per unit area using the relationship between Doppler frequency and angle of incidence. Curves may be plotted from these data which are characteristic of specific terrains.

The side-looking airborne radar (SLAR) imagery has been of particular value in geologic analysis. Major structural and lithological areas are sharply defined, and drainage and fracture patterns are easily seen. Rock types have been identified from radar imagery through microdensitometer measurements of the film (ref. 67), and vegetation types have been differentiated and mapped (ref. 68).

This technique has also been applied in examining the changing nature of sea ice. As shown in figure 77, SLAR imagery can distinguish between polar-pack ice, winter ice, and water areas and provide an indication of surface texture, configuration, and relative thickness (ref. 69). The radar data shown here were obtained by an AN/APQ-56(XAA) SLAR system installed in a USAF aircraft with an operating frequency of 35.4 GHz. The conventional oblique photographs shown in figure 77 were taken at lower altitudes over essentially the same areas. The photographs and imagery shown in this figure were furnished by the Army Cold Regions Research and Engineering Laboratory. The photographs, which were taken over the Kane Basin and Smith Sound area between Greenland and Ellesmere Island in April 1962, show sea ice ranging from partial slush coverage to thicknesses of over 6 feet. The ice-water boundary is easily seen in figure 77(a) in which the ice of Kane Basin is to the right of the center. The dark area and white lines in the center of this photograph are typical of dual-antenna SLAR imagery and represent the area immediately below the aircraft, which is not scanned. This area may be as much as 20 miles across depending upon the operation mode selected. Figure 77(b) is a conventional photograph of the windblown slush pattern in the Smith Sound area. Figures 77(c) and 77(d) depict an area farther north in the Robeson Channel. The light ice areas are polar-pack ice. Figure 77(d) is a conventional oblique photograph of the sea-ice pattern depicted on the radar image shown in figure 77(c). Figure 78 is a comparison of a radar map with an aerial photographic mosaic of Leidy Glacier in northwest Greenland (ref. 70).

As noted by R. K. Moore in reference 71, "radar scatterometers permit more detailed observation of radar-scattering behavior than radar imagers

in the same way that infrared spectrometers permit more detailed observa-
tion than infrared imagers." These scatterometers measure the variation of
differential scattering cross section of a surface with angle of incidence.
Any radar system, if properly calibrated, will provide this information,
but these are normally limited since they provide measurements at only one
incidence angle for each point illuminated. Side-looking radar units have
been modified for use as scatterometers (ref. 72), and some systems have
been designed exclusively for this purpose. Figure 79 shows a planar array
antenna developed by Ryan Electronic and Space Systems, and figure 80 is an
illustration showing its beam geometry. The unit generates a fan beam 120°
along the longitudinal axis of the aircraft, 3° wide. With such a system,
operating at 13.3 GHz, scatterers may be tracked through the entire beam
during an overflight, generating a set of reflectivity curves characteristic
of the scatterer at all incidence angles. Changes in Doppler frequency are
usually recorded on magnetic tape with appropriate calibration signals for
later data reduction. Independent measurements of absolute altitude above
terrain, groundspeed, and drift angle are also required for correlation and
correction.

Figure 81 is a composite of an aerial photograph taken of a portion
of the Pisgah volcanic crater area near Barstow, California, and the re-
flectivity curves generated by this system at three angles of incidence.
The transition from sand to lava and the difference in information content
at the various angles is quite evident in the data.

Another type of scatterometer is the LFE Spectrac, shown in figure 82.
It is a single-beam circularly polarized system operated at 9.8 GHz with a
50-percent-duty-ratio interrupted continuous wave modulation. At an alti-
tude of 5000 feet, this unit produces an along-track resolution of about
15 feet. Figure 83 is a strip-chart sample of data obtained by this sys-
tem over Meteor Crater, near Winslow, Arizona, in January 1966. Figure 84
is a correlation photograph taken during this overflight at an altitude of
4500 feet, showing the approximate aircraft ground track.

Figure 85 shows several characteristic curves that have been devel-
oped for various types of terrain and sea-state conditions from scatterom-
eter data (refs. 72 to 74).

CONCLUDING REMARKS

All of the remote-sensing systems mentioned here provide unique in-
formation concerning some target area, which is often difficult or impos-
sible to obtain by any other means. As several prominent researchers have
shown, the amount of data developed by these several sensors expands loga-
rithmically when cross-correlations can be made over a particular target.
This has been shown graphically in the case of multispectral photography.

The ideal situation would be to cluster these systems on one high-altitude platform so that simultaneous sensing of a target across the entire electromagnetic spectrum could be accomplished and a much more complete description result. This objective will be realized in part when the post-Apollo manned orbiting laboratories are launched. In the intervening period, heavily instrumented aircraft can perform this function to some degree. This aircraft phase will probably continue to operate in a testing and calibration capacity after the space laboratories are a reality.

Two of these flying test beds, shown in figures 86 and 87, are operated by the NASA Manned Spacecraft Center and based at Ellington Air Force Base, Houston, Texas. Other similarly equipped vehicles are a Convair 990, operated by NASA, and a C-121 flown by the Naval Research Laboratory (fig. 68). Some of the data contained in this report were obtained from sensors installed in these aircraft.

The illustrations and sensor-data samples contained in this report were drawn from a variety of sources. Deep appreciation is expressed for the cooperation and helpful criticism which was offered by the many experimenters, educators, MSC personnel, and associated companies; without their assistance this report could not have been completed. The author is particularly indebted to Dr. John W. Kern, associate professor of physics at the University of Houston, Houston, Texas, and Mr. Harold D. Toy, Chief, Flight Research Projects Branch, NASA/MSC, for their superior technical direction and for their creation and continuing support of a stimulating research-oriented environment.

REFERENCES

1. Leet, L. D.; and Judson, S.: Physical Geology. Prentice-Hall, Inc. (Englewood Cliffs, N.J.), 1965.

2. Coates, R. J.: Solar Observations at Millimeter Wavelengths. Proceedings of the IEEE, vol. 54, no. 4, Apr. 1966, pp. 471-476.

3. Evans, J. V.: Radio Echo Studies of the Moon, ch. 12 in Physics and Astronomy of the Moon. Academic Press, 1962, pp. 428-478.

4. Meyer, J. W.: Radar Astronomy at Millimeter and Submillimeter Wavelengths. Proceedings of the IEEE, vol. 54, no. 4, Apr. 1966, pp. 484-492.

5. Fessenkov, V. G.: Photometry of the Moon, ch. 4 in Physics and Astronomy of the Moon. Academic Press, 1962, pp. 99-128.

6. Green, J.: Geophysics As Applied to Lunar Exploration. Aerospace Laboratories, No. Amer. Aviation, Inc., AFCRC Doc. no. AFCRL-TR-60-409, June 30, 1960.

7. Warren, C. R.: Surface Material of the Moon. Science, vol. 140, no. 3563, Apr. 12, 1963, p. 188.

8. Kolcum, E. H.: View of Stars Clarified by Space Vehicles. Aviation Week and Space Technology, Oct. 22, 1962, pp. 54-57.

9. Kupperian, J. E., Jr.: Astronomical Research in Space Vehicles, in Geophysics and Astronomy in Space Exploration. NASA SP-13, Dec. 1962, pp. 31-37.

10. Ludwig, G. H.: Particles and Fields Research in Space, in Geophysics and Astronomy in Space Exploration. NASA SP-13, Dec. 1962, pp. 21-29.

11. Parker, E. N.: Interplanetary Plasma. Proceedings of the Amer. Astronaut. Soc. Symposium on Unmanned Exploration of the Solar System, Denver, Colo., Feb. 8-10, 1965, pp. 85-95.

12. Pickering, W. H.: Instrumentation for the Exploration of the Moon and Planets. Proceedings of the 11th National Aerospace Instrumentation Symposium, Instrument Soc. of Amer., Calif. Inst. of Tech., Jet Propulsion Lab., Pasadena, Calif., Oct. 5-7, 1965, pp. 17-26.

13. Raitt, R. J.; Laflin, S.; and Boyd, R. L. F.: A Synoptic View of Ionic Constitution Above the F-Layer Maximum. Space Science, vol. 1, publication of Goddard Space Flight Center, 1965, pp. 408-411.

28

14. Bridge, H. S.: What We Know and What We Don't Know About the Solar Wind. Proceedings of the JPL Conference on the Solar Wind, Apr. 1-4, 1964, pp. 123-143.

15. Levine, M. A.: Plasmas in Space. IEEE Spectrum, vol. 43, no. 47, Nov. 1966.

16. Naugebauer, M.; and Snyder, C. W.: Mariner 2 Observations of the Solar Wind: pt. 1 - Average Properties. J. Geophys. Res., vol. 71, Oct. 1, 1966, pp. 4469-4484.

17. Pizzella, G.; Davis, L. R.; and Williamson, J. M.: Electrons in the Van Allen Zone Measured with a Scintillator on Explorer 14. J. Geophys. Res., vol. 71, Dec. 1966, pp. 5495-5508.

18. Vaysberg, O. L.; and Shuyskaya, F. K.: Distribution of Electrons with $E > 40$ Kev by Pitch Angles in Inner Belt According to Data from KOSMOS 5 Satellite. Cosmic Research, vol. 3, no. 6, 1966, pp. 134-153.

19. Waddel, R. C.: The Relay 1 Radiation Effects Experiment. NASA SP-76, Nov. 1966.

20. Krimigis, S. M.; and Armstrong, T. P.: Observations of Protons in the Magnetosphere with Mariner 4. J. Geophys. Res., vol. 71, Oct. 1966; pp. 4641-4650.

21. Cortright, E. M.: Automated Spacecraft Come of Age. Astronaut. Aeron., Jan. 1967, pp. 22-28.

22. Chubb, T. A.: Problems of the Upper Atmosphere. Proceedings of the IRE, vol. 50, no. 11, Nov. 1962, pp. 2198-2201.

23. Suomi, V. E.: Observing the Atmosphere - A Challenge. Proceedings of the IRE, vol. 50, no. 11, Nov. 1962, pp. 2192-2197.

24. Walker, J. C. G.: The Upper Atmosphere. Space Aeronaut., vol. 42, no. 4, Oct. 1964, pp. 56-63.

25. Stroud, W. G.: Our Earth as a Satellite Sees It. National Geographic Magazine, vol. 118, 1960, pp. 292-302.

26. Walker, J.: Detection of Marine Organisms by an Infrared Mapper. Oceanography from Space, Woods Hole Oceanographic Inst., Apr. 1965, pp. 321-335.

27. Goodison, C. E.: Operational Weather Satellites - Receiving Cloud Cover Pictures. Wireless World, vol. 72, Dec. 1966, pp. 590-594.

28. Stoffregen, W.; and Derblom, H.: ·Observations of an Artificial
    Sodium Cloud in Twilight in Southern France. Rocket Experiments
    for Studies on D-Region Ion Concentration and Emission from
    Released Chemicals in Twilight and Aurora, Research Inst. of Nat.
    Defense, Stockholm, Sweden, 1966, pp. 60-63.

29. Wright, J. W.; and Fedor, L. S.: Comparison of Ionospheric Drift
    Velocities by the Spaced Receiver Technique with Neutral Winds
    from Luminous Rocket Trails. NASA CR-78844, Oct. 1966.

30. Block, A. V.; Kadis, A. L.; and Smith, L. C.: High Altitude Gun
    Probes. GCA Technical Report no. 65-15-G, Sept. 1965.

31. Evans, J. W.: Development of Gun Probe Payloads and a 1750 MC/S
    Telemetry System. CFSTI, BRL-MR-1749, May 1966, pp. 1-73.

32. Air Force Cambridge Research Laboratories: Report on Research at
    AFCRL, July 1963 to June 1965, (Office of Aerospace Research,
    Bedford, Mass.), AFCRL-65-595, Sept. 1965, pp. 1-315.

33. Gursky, H.; Giacconi, R.; Gorenstein, P.; and Waters, J. R.: A
    Program of X-Ray Astronomy from Sounding Rockets, Final Report,
    NASA-CR-79097, 1966.

34. Smith, L. G.: Langmuir Probes for Measurements in the Ionosphere.
    GCA Technical Report no. 65-25-N, Oct. 1965.

35. Pederson, A.: Measurements of Ion Concentrations in the D-Region
    of the Ionosphere. Rocket Experiments for Studies on D-Region
    Ion Concentration and Emission from Released Chemicals in Twilight
    and Aurora, Research Inst. of Nat. Defense, Stockholm, Sweden,
    1966, pp. 9-32.

36. Pederson, A.; and Oeberg, B.: Development and Construction of
    Gerdien Condenser Rocket Probes in Rocket Experiments for Studies
    on D-Region Ion Concentration and Emission from Released Chemicals
    in Twilight and Aurora, Research Inst. of Nat. Defense, Stockholm,
    Sweden, Rept. 15, 1966, pp. 33-45.

37. Smith, L. G.; Bedinger, J. F.; and Best, G. T.: Measurement of
    Upper Atmospheric Ionization and Winds With a Combined Payload.
    GCA Technical Report no. 66-11-N, June 1966, pp. 1-95.

38. Bedinger, J. F.; and Knaflich, H. B.: Observed Characteristics of
    Ionospheric Winds. GCA Technical Report no. 65-26-N, Aug. 1965.

39. Maseide, K.: Emission from a Sodium Trail Released in Aurora, Part II: Observations from the Launch Site. Rocket Experiments for Studies on D-Region Ion Concentration and Emission from Released Chemicals in Twilight and Aurora, Research Inst. of Nat. Defense, Stockholm, Sweden, 1966, pp. 83-91.

40. Rosenberg, N. W.: Chemical Releases at High Altitudes. Science, ·vol. 152, no. 3725, May 20, 1966, pp. 1017-1027.

41. Taylor, R. J.: An Analysis of Some Wind Profiles in the Atmospheric Friction Layer, AFCRL-63-861, Aug. 1963.

-42. Pinus, N. Z.: Atmospheric Turbulence. Translated from Atmosfernaya Turbulentnost, Trudy Tsentral'noy Aerologicheskoy Observatorii, no. 54, Hydrometeorological Publishing House, Moscow, 1964, NASA TT-F-246, Sept. 1965.

43. Curcio, J. A.: Evaluation of Atmospheric Aerosol Particle Size Distribution from Scattering Measurements in the Visible and Infrared. J. Opt. Soc. Am., vol. 51, 1961, pp. 548-551.

44. Brock, G. C.; Harvey, D. I.; Kohler, R. J.; and Myskowski, E. P.: Photographic Considerations for Aerospace. Itek Corp., Lexington, Mass., 1965.

45. Clarke, J. D.: Environmental Factors Affecting Airborne Photography. Soc. of Motion Picture and Television Engineers, Semiannual Technical Conference and Equipment Exhibit, Los Angeles, Calif., preprint no. 100-9, Oct. 2-7, 1966, pp. 1-18.

46. Gifford, F., Jr.: The Height of Scintillation Producing Disturbances. Bull. Am. Meteorol. Soc., vol. 36, no. 1, Jan. 1965, pp. 35-36.

47. Colwell, R. N.; Brewer, W.; Landis, G.; Langley, P.; Morgan, J.; Rinker, J.; Robinson, J.; and Sorem, A.: Basic Matter and Energy Relationships Involved in Remote Reconnaissance. Photogrammetric Engineering, vol. 29, no. 5, Sept. 1963, pp. 761-799.

48. Gates, D. M.: The Energy Environment in Which We Live. American Scientist, vol. 51, 1963, pp. 327-348.

49. Weidner, R. T.; and Sells, R. L.: Elementary Modern Physics, Allyn and Bacon, Inc., June 1965.

50. Colwell, R. N.: Uses and Limitations of Multispectral Remote Sensing. Proceedings of the 4th Symposium on Remote Sensing of Environment, University of Michigan, Apr. 12-14, 1966, pp. 71-100.

51. Parker, D. C.; and Wolff, M. F.: Remote Sensing. International Science and Technology, July 1965, pp. 20-31.

52. Toy, H. D.; Craib, K. B.; and Hughey, J. P.: Introduction to NASA 926 and NASA 927 Remote Sensor Aircraft as Applied to the Earth Resources Survey Program, NR-04-00-999-0001, Mar. 1966.

53. de Sitter, L. U.: The Development of Photogeology. Publication of the International Training Center for Aerial Survey, Delft - The Netherlands, sp. 2, no. 33, Autumn 1965, pp. 4-5.

54. Colwell, R. N.; Thorley, G. A.; Draeger, W. C.; and Lauer, D. T.: A Multispectral Photographic Experiment Based on a Statistical Analysis of Spectrometric Data, Univ. of Calif., School of Forestry, NASA Grant NGR-05-003-080, June 1965.

55. Heller, R. C.; McCambridge, W. F.; Aldrich, R. C.; and Weber, F. P.: The Use of Multispectral Sensing Techniques to Detect Ponderosa Pine Trees Under Stress from Insect or Pathogenic Organisms, Annual Progress Report, NASA-CR-78741, Sept. 1966.

56. Weber, F. P.: Multi-spectral Imagery for Species Identification, NASA-CR-78756, Sept. 1966.

57. Thomas, J. R.; Myers, V. I.; Heilman, M. D.; and Wiegand, C. L.: Factors Affecting Light Reflectance of Cotton. Proceedings of the 4th Symposium on Remote Sensing of Environment, Univ. of Michigan, Apr. 12-14, 1966, pp. 305-312.

58. Hoffer, R. M.; Holmes, R. A.; and Shay, J. R.: Vegetative, Soil, and Photographic Factors Affecting Tone in Agricultural Remote Multispectral Sensing. Proceedings of the 4th Symposium on Remote Sensing of Environment, Univ. of Michigan, Apr. 12-14, 1966, pp. 115-134.

59. Meier, M. F.; Alexander, R. H.; and Campbell, W. J.: Multispectral Sensing Tests at South Cascade Glacier, Washington. Proceedings of the 4th Symposium on Remote Sensing of Environment, Univ. of Michigan, Apr. 12-14, 1966, pp. 145-159.

60. Fischer, W. A.; Moxham, R. M.; Polcyn, R.; and Landis, G. H.: Infrared Surveys of Hawaiian Volcanoes. Science, vol. 146, Nov. 1964, pp. 733-742.

61. McLerran, J. H.: Airborne Crevasse Detection. Paper presented at the 3rd Symposium on Remote Sensing of Environment, Univ. of Michigan, Oct. 1964.

62. McLerran, J. H.: Infrared Sea Ice Reconnaissance. Proc. 3rd
     Symposium on Remote Sensing of Environment, Univ. of Michigan,
     Oct. 1964, pp. 789-797.

63. Schule, J. J., Jr.; and Wilkerson, J. C.: An Oceanographic Aircraft.
     Pres. at Am. Inst. of Aeronautics and Astronautics. U.S. Navy,
     2nd, Marine Systems and Antisubmarine Warfare Conf., Los Angeles,
     Calif., Aug. 8-10, 1966.

64. Barath, F. T.: Microwave Radiometry and Application to Oceanog-
     raphy. Oceanography from Space, Woods Hole Oceanographic Inst.,
     Woods Hole, Mass., Apr. 1965, pp. 235-239.

65. Conway, W. H.; and Mardon, A.: Microwave Radiometers for Ocean and
     Weather Measurements. Oceanography from Space, Woods Hole Oceano-
     graphic Inst., Woods Hole, Mass., Apr. 1965, pp. 241-271.

66. Kinsman, F. E.: Non-Contact Sensors, Across the Electromagnetic
     Spectrum, For Geoscience Purposes. Presented at the 16th Annual
     Southwestern IEEE Conference, Dallas, Texas, Apr. 24, 1964.

67. Pierson, W. J., Jr.; Scheps, B. B.; and Simonett, D. S.: Some Appli-
     cations of Radar Return Data to the Study of Terrestrial and
     Oceanic Phenomena. Proceedings of the 3rd Goddard Memorial Sympo-
     sium on Scientific Experiments for Manned Orbital Flight, CRES
     Technical Report no. 61-8, Mar. 18-19, 1965; pp. 87-137.

68. Simonett, D. S.; and Morain, S. A.: Remote Sensing from Spacecraft
     as a Tool for Investigating Arctic Environments. Presented at the
     7th Congress International Quaternary Assoc., Boulder, Colo.,
     CRES Report no. 61-5, Sept. 1965.

69. Anderson, V. H.: High Altitude, Side-Looking Radar Images of Sea
     Ice in the Arctic. Proceedings of the 4th Symposium on Remote
     Sensing of Environment, Univ. of Michigan, Apr. 12-14, 1966,
     pp. 845-857.

70. Leighty, R. D.: Terrain Information from High Altitude Side-Looking
     Radar Imagery of an Arctic Area. Proceedings of the 4th Symposium
     of Remote Sensing of Environment, Univ. of Michigan, Apr. 12-14,
     1966, pp. 575-597.

71. Moore, R. K.: Radar Scatterometry - An Active Remote Sensing Tool.
     Univ. of Kansas, Center for Research, Inc., Engineering Science
     Div., Report no. 61-11, Apr. 1966.

72. Newbry, L. E.: Terrain Radar Reflectance Study. Photogrammetric
     Engineering, vol. 26, no. 4, 1960, pp. 630-637.

73. Taylor, R. C.: Terrain Return Measurements at X, K_u, and K_a Band. Presented at the National IRE Meeting, New York, N.Y., Mar. 25, 1959, Ohio State Univ. Dept. of Electrical Engineering, vol. 7, part 1, Apr. 1959.

74. Floyd, W. L.; and Lund, T. J.: Scatterometer Program. Supplement to IEEE Transactions on Aerospace and Electronic Systems, vol. 2, no. 6, Nov. 1966, pp. 323-328.

BIBLIOGRAPHY

Aerial Photographic Reference Handbook: Hycon Mfg. Co., Monrovia, Calif.,
   1965.

Anson, A.: Color Photo Comparison. Photogrammetric Engineering,
   Mar. 1966, pp. 286-297.

Apollo Experiments Guide: NASA Office of Manned Space Flight,
   Washington, D.C., NPC-500-9, June 1965.

Babish, R. C.: Temperature and Pressure Considerations in Reconnaissance
   Systems. Principles of Optics, Perkin-Elmer Corp. (Norwalk, Conn.),
   Jan. 10-11, 1962, pp. 9.1-9.5.

Badgely, P. C.; Fischer, W.; and Lyon, R. J. P.: Geologic Exploration
   From Orbital Altitudes. Geotimes, vol. 10, no. 2, Sept. 11-14, 1965.

Bailey, E. A.: Oceanographic Spectral Photography. Itek Corp.,
   Palo Alto, Calif., Vidya Report no. 219, Apr. 29, 1966.

Basic and Advanced Infrared Technology: U.S. Army Missile Command,
   Redstone Arsenal, Alabama, AD-634535, Apr. 1965, pp. 1-173.

Bazhulin, P. A.; Kartashev, A. V.; and Markov, M. N.: Investigation of
   the Angular and Spectral Distributions of Terrestrial Radiation in the
   Infrared Range of the Spectrum by Utilizing Cosmos-45. Translated from
   Kosmich Issled, vol. 4, no. 4, Lockheed Missiles and Space Co.
   Rept. no. N66-39878, 1966, pp. 601-618.

Berkner, L. V.: Geoscience and Geoengineering. Proceedings of the IRE,
   vol. 50, no. 11, Nov. 1962, pp. 2180-2182.

Blinn, J. C., III; and Campbell, J. P.: Microwave Radiometric Sensing
   for Air Navigation. IEEE Transactions on Aerospace and Electronic
   Systems, vol. AES-2, no. 5, Sept. 1966, pp. 585-590.

Bogomolov, L. A.: Problems in Interpreting Aerial Photographs. Trans-
   lated from Geodeziia i Aerofotos'emka, 1965, by the Technical Informa-
   tion Service, American Institute of Aeronautics and Astronautics, Inc.,
   Geodesy and Aerophotography, no. 6, 1965, pp. 386-389.

Branigan, T. L., ed.: TRW Space Log, vol. 4, no. 2, TRW Systems
   (Redondo Beach, Calif.), Summer 1964.

Brock, G. C.: The Status and Problems of Air Photography. The Photographic Journal, June 1961, pp. 165-177.

Brown, E. B.: Military Infrared. Principles of Optics, Perkins-Elmer Corp., Jan. 10-11, 1962, pp. 7.1-7.7.

Canada, A. H.: Simplified Calculation of Black Body Radiation. General Electric Review, Dec. 1948, pp. 50-54.

Celestial Mechanics and Space Flight Analysis: NASA SP-15, Dec. 1962.

Colwell, R. N.: Some Practical Applications of Multiband Spectral Reconnaissance. American Scientist, vol. 49, no. 1, 1961, pp. 9-36.

Cutrona, L. J.; Leith, E. N.; Porcello, L. J.; and Vivian, W. E.: On the Application of Coherent Optical Processing Techniques to Synthetic-Aperture Radar. Proceedings of the IEEE, vol. 54, no. 8, Aug. 1966, pp. 1026-1032.

Data Acquisition from Spacecraft: NASA SP-16, Dec. 1962.

Deller, M. H. A.; and Marchant, A. C.: Some Aspects of Modern Optics. Ministry of Aviation, Farnborough Hants, England, Technical Report no. 65012, Feb. 1965, pp. 1-164.

Derenyi, E. E.; and Konecny, G.: Infrared Scan Geometry. Photogrammetric Engineering, vol. 32, Sept. 1966, pp. 773-778.

Dutton, J. A.: Space and Time Response of Airborne Radiation Sensors for the Measurement of Ground Variables. J. Geophys. Res., vol. 67, no. 1, Jan. 1962, pp. 195-205.

Easterling, M.; and Goldstein, R.: The Interplanetary Medium and S-Band Telecommunications. Astronaut. Aeron., Aug. 1966, pp. 80-86.

Eisenman, W. L.; Merriam, J. D.; and Naugle, A. B.: Properties of Photodetectors. Naval Ordinance Lab., Corona, Calif., NOLC Rept. no. 631, Dec. 30, 1965.

Ewing, G. C., ed.: Proceedings of Conference on the Feasibility of Conducting Oceanographic Explorations from Aircraft, Manned Orbital and Lunar Laboratories. Oceanography from Space, Woods Hole Oceanographic Institution, Woods Hole, Mass., Apr. 1965.

Fink, D. E.: Gemini Photos Advance AES Experiments. Aviation Week and Space Technology, Aug. 9, 1965, pp. 61-62.

Foster, W. B.; and George, T. A.: Post-Apollo Experiments in Space. Astronaut. Aeron., vol. 4, Mar. 1966, pp. 50-56.

Friedman, J. D.; Lyon, R. J. P.; Beattie, D. A.; and Downey, J.: Lunar Ground Data Required for Interpretation of AES Orbital Experiments. AAS — Advances in the Astronautical Sciences, vol. 20, 1966, pp. 381-395.

Fung, A. K.: Theory of Radar Scatter from Rough Surfaces, Bistatic and Monostatic, with Application to Lunar Radar Return. J. Geophys. Res., vol. 69, no. 6, Mar. 15, 1964, pp. 1063-1073.

Geophysics and Astronomy in Space Exploration: NASA SP-13, Dec. 1962.

Grimwood, J. M.: Project Mercury, A Chronology. NASA SP-4001, 1963.

Harris, D. B.: Microwave Radiometry. The Microwave Journal, Apr. 1960, pp. 41-46.

Harris, D. E.; and Woodbridge, C. L.: Terrain Mapping by Use of Infrared Radiation. Photogrammetric Eng., vol. 30, Jan. 1964, pp. 134-139.

Hatcher, N. M.; Newcomb, A. L., Jr.; and Groom, N. J.: Development and Testing of a Proposed Infrared Horizon Scanner for Use in Spacecraft Attitude Determination. NASA TN-D-2995, Sept. 1965.

Hayre, H. S.: Roughness and Radar Return. Proceedings of the IRE, vol. 50, no. 2, Feb. 1962, pp. 223-224.

Henry, J. P.; and Mosely, J. D.: Results of the Project Mercury Ballistic and Orbital Chimpanzee Flights. NASA SP-39, 1963.

Hufnagel, R.: Atmospheric Seeing. Principles of Optics, Perkin-Elmer Corp. (Norwalk, Conn.), Jan. 10-11, 1962, pp. 8.1-8.4.

Katz, I.: Radar Reflectivity of the Earth's Surface. Applied Physics Lab. Technical Digest, Jan.-Feb. 1963, pp. 10-17.

Kawachi, D. A.: Image Motion Due to Camera Rotation. Photogrammetric Engineering, 1965, pp. 861-867.

Kendrick, J. B.: Space Data. TRW Systems (Redondo Beach, Calif.), 1962.

Kendrick, J. B.: Space Data. TRW Systems (Redondo Beach, Calif.), 1965.

Klass, P. J.: Lack of Infrared Data Hampers Midas. Infrared Sensors in Space, part 1, Aviation Week and Space Technology, Sept. 24, 1962, pp. 54-57.

Kleinknecht, K. S.; and Bland, W. M., Jr.: Mercury Project Summary, Including Results of the Fourth Manned Orbital Flight. NASA SP-45, May 15-16, 1963.

Kuo, Wei-hsing: Electronics Applied in Aerial Surveying. Translated from Chinese, Wu hsien tien, 8, 1965, U.S. Army Engineering and Development Labs., Scientific and Technical Information Div., Fort Belvoir, Va., TT-66-61851; July 1966.

Lehman, W. J., Jr.: Report on Black Body Radiance - Temperature Conversion Table. Defense Documentation Center AD-417811, Aug. 1963.

Leonardo, E. S.: Capabilities and Limitations of Remote Sensors. Photogrammetric Engineering, vol. 30, no. 6, 1964, pp. 1005-1010.

Leonardo, E. S.: Comparison of Imaging Geometry for Radar and Camera Photographs. Photogrammetric Engineering, vol. 29, no. 2, 1963, pp. 287-293.

Livingston, R. C.: The Attainment of Quality in the Military Development of Airborne Mapping Systems. Presented at the Semi-Annual Convention of the American Society of Photogrammetry, Dayton, Ohio, Sept. 1965.

Manual of Physical Properties of Kodak Aerial and Special Sensitized Material: Eastman Kodak Co., Rochester, N.Y., Jan. 1965.

Matos, R. A.: Aerial Camera for Photogrammetric Research. Photogrammetric Engineering, vol. 31, Nov. 1965, pp. 978-983.

Mueller, G. E.: Beyond Apollo. Astronaut. Aeron., vol. 3, Aug. 1965, pp. 54-59.

Murray, B. D.; and Westphal, J. A.: Infrared Astronomy. Scientific American, vol. 213, Aug. 1965, pp. 20-29.

Myers, V. I.; Wiegand, C. L.; Heilman, M. D.; and Thomas, J. R.: Remote Sensing in Soil and Water Conservation Research. Proceedings of the 4th Symposium on Remote Sensing of Environment, Univ. of Michigan, Apr. 12-14, 1966, pp. 801-813.

Narva, M. A.; and Muckler, F. A.: Visual Surveillance and Reconnaissance from Space Vehicles. Human Factors, vol. 5, June 1963, pp. 295-315.

Neal, J. T.: Airborne Geoscience Research. Photogrammetric Engineering, vol. 28, no. 3, 1962, pp. 438-441.

Ratner, Vic A.: A Proposed New Set of Performance Standards and
   Specification Criteria for Wideband Magnetic Tape Recording. Elec-
   tronic Instrument Digest, Sept. 1966, pp. 17-23.

Richter, E. W.: Millimeter Radiometers. The Microwave Journal,
   Oct. 1960, pp. 63-66.

Riegler, R. L.: Microwave Radiometric Temperatures of Terrain. Ohio
   State Univ. Research Foundation Report no. 1903-2, June 1966.

Rosenblum, E. S.: Atmospheric Absorption of 10-400 KMCPS Radiation:
   Summary and Bibliography to 1961. The Microwave Journal, Mar. 1961,
   pp. 91-96.

Rouse, J. W., Jr.; Waite, W. P.; and Walters, R. L.: Use of Orbital
   Radars for Geoscience Investigations. CRES Report No. 61-8, Jan. 1966.

Salgado, J. A. M.; Belculfine, U.; Del Tepesco, M.; and de Mendonca, F.:
   Meteorological Sounding Rocket Program at Natal. Presented at the
   Experimental Inter-American Meteorological Rocket Network Executive
   Committee Meeting, Ascochinga, Argentina, CFSTI, Sept. 1966.

Savage, J. R.: Terrestrial Photogrammetry for Geological Purposes.
   Publication of the International Training Center for Aerial Survey,
   Delft, The Netherlands, Spec. Pub. No. 2, Series B, no. 33, pp. 41-53.

Scott, R. M.: Photoreconnaissance Applications and Concluding Remarks.
   Principles of Optics, Perkin-Elmer Corp. (Norwalk, Conn.), Jan. 10-11,
   1962, pp. 10.1-10.3.

Sobel, J. A., III: Prototype Airborne IR Fire Mapping System. Imaging
   Systems Development Lab., HRB-Singer, Nov. 1965, pp. 1-7.

Soviet-Bloc Research in Geophysics, Astronomy, and Space, No. 142:
   Joint Publications Research Service Technical Translation
   no. 61-11147-142, U.S. Dept. of Commerce, Oct. 18, 1966.

Soviet-Bloc Research in Geophysics, Astronomy, and Space, No. 143:
   Joint Publications Research Service Technical Translation
   no. 61-1147-143, U.S. Dept. of Commerce, Nov. 2, 1966.

Space Age Photography: Perkin-Elmer Corp. (Norwalk, Conn.)

Staelin, D. H.: Measurements and Interpretation of the Microwave
   Spectrum of the Terrestrial Atmosphere Near 1-Centimeter Wavelength.
   J. Geophys. Res., vol. 71, no. 12, June 15, 1966, pp. 2875-2881.

Tangborn, W. V.: Glaciological Investigations On South Cascade Glacier.
The Mountaineer, vol. 55, no. 4, 1962.

Verstappen, H. Th.: Geomorphology and the Conservation of Natural
Resources. Publications of the International·Training Center for
Aerial Survey, Delft, The Netherlands, Spec. Pub. No. 2, Series B,
no. 33, 1965, pp. 24-36.

Walsh, D.: The United States and the World Ocean. Presented at the
Second Annual Edwin A. Link Lecture, Smithsonian Institution,
Washington, D.C., no. 4650, Feb. ·1965.

Warnecke, G.; and Nordberg, W.: Inferences of Stratospheric and
Mesospheric Circulation Systems from Rocket Experiments. Proceedings
of the 5th International Space Science Symposium, Florence, Italy, 1964.

Washer, F. E.: Sources of Error in Various Methods of Airplane Camera
Calibration, National Bureau of Standards Report no. NBS 2534,
June, 1953.

Williams, R. A.; and Chang, W. S. C.: Observation of Solar Radiation
 from 50μ to 1 mm. Proceedings of the IEEE, vol. 54, no. 4, Apr. 1966,
pp. 462-470.

Wilson, R. B.·, Jr.: A Study of Geodetic Techniques. Air Force Cambridge
Research Laboratories, AFCRL 65-102, Dec. 1963.

TABLE I.- ABSORPTION BANDS OF THE ATMOSPHERE

Wavelength region	Kind and degree of absorption
X-ray 0.003μ to 0.03μ	Complete absorption because of short wavelength in relation to size of atmospheric particles and very high photon energy with consequent high probability of interaction with atmospheric matter
Ultraviolet 0.03μ to 0.13μ	N_2 and O_2 electronic bands and associated continua; almost complete absorption
0.13μ to 0.22μ	O_2 electronic bands; almost complete absorption
0.22μ to 0.30μ	O_3 electronic bands; strong absorption
0.30μ to 0.40μ	Rayleigh scattering; no specific absorption bands
Visual and photographic infrared 0.40μ to 1.0μ	Few absorption bands except for H_2O at 0.9μ; good transmission
Near infrared 1.0μ to 20.0μ	Many rotational-vibrational absorption bands throughout the region; O_2 electronic band at 1.06μ and 1.27μ, rotational H_2O bands in 15μ to 24μ region; best window is the 8μ to 14μ band
Far infrared 24μ to 1000μ	Many rotational lines, principally H_2O; strong absorption
Microwave 1 mm to 10 cm	Widely spaced pure rotational lines; many clear windows
Radio frequencies 10 cm on out	Almost complete transmission

TABLE II.- REMOTE-SENSOR APPLICATION AREAS

Sensor technique	Agriculture forestry	Geology	Hydrology	Oceanography	Geography
Visual photography	Crop and soil identification, identification of plant vigor and disease	Identification of surface features	Identification of drainage patterns	Identification of sea state, beach erosion, offshore depth and turbidity	Urban and rural land use; transportation routes and facilities; terrain and vegetation characteristics
Multi-spectral photography		Identification of surface structure	Soil-moisture content	Sea color as indicative of living organisms	
Infrared imagery and spectroscopy	Terrain composition, plant vigor and disease condition	Mapping thermal anomalies, mineral identification	Detection of areas cooled by evaporation	Mapping of ocean currents, sea-ice investigations	Surface-energy budgets, near-shore currents and land use
Radar imagery	Soil characteristics, vegetation type, identification of plant disease	Surface roughness, tectonic mapping	Measurement of soil-moisture content, identification of runoff slopes	Sea state, ice flow and ice penetration, Tsunami warning	Land and ice mapping, cartographic and geodetic mapping
Radio-frequency reflectivity		Subsurface layering, mineral identification	Moisture content of soils	Sea-ice thickness and mapping sea state	Land-ice mapping and thickness, penetration of vegetation cover

TABLE II.- REMOTE-SENSOR APPLICATION AREAS - Concluded

Sensor technique	Agriculture forestry	Geology	Hydrology	Oceanography	Geography
Passive microwave	Brightness temperature map of terrain	Dielectric constant measurement indicative of subsurface layering	Snow and ice surveys	Sea-ice and ocean-current mapping	Snow and ice measurements
Absorption spectroscopy (remote geochemical sensing)		Detection of mineral deposits, trace metals, and oilfields		Detection of concentration of surface marine flora	
Laser systems	Topography	Surface roughness	Albedo measurements, lake and reservoir levels	Sea state, shoals and coastal mapping, ice surveillance	Topographic mapping
Magnetometers		Crustal and mantle studies, mineral deposits		Subsurface structure	Resources utilization
Gravity gradiometers		Crustal and mantle studies, mineral deposits, geologic structure		Subsurface structure	
Ultraviolet sensors		Lithology, geologic structure, stratigraphy, mineral deposits			
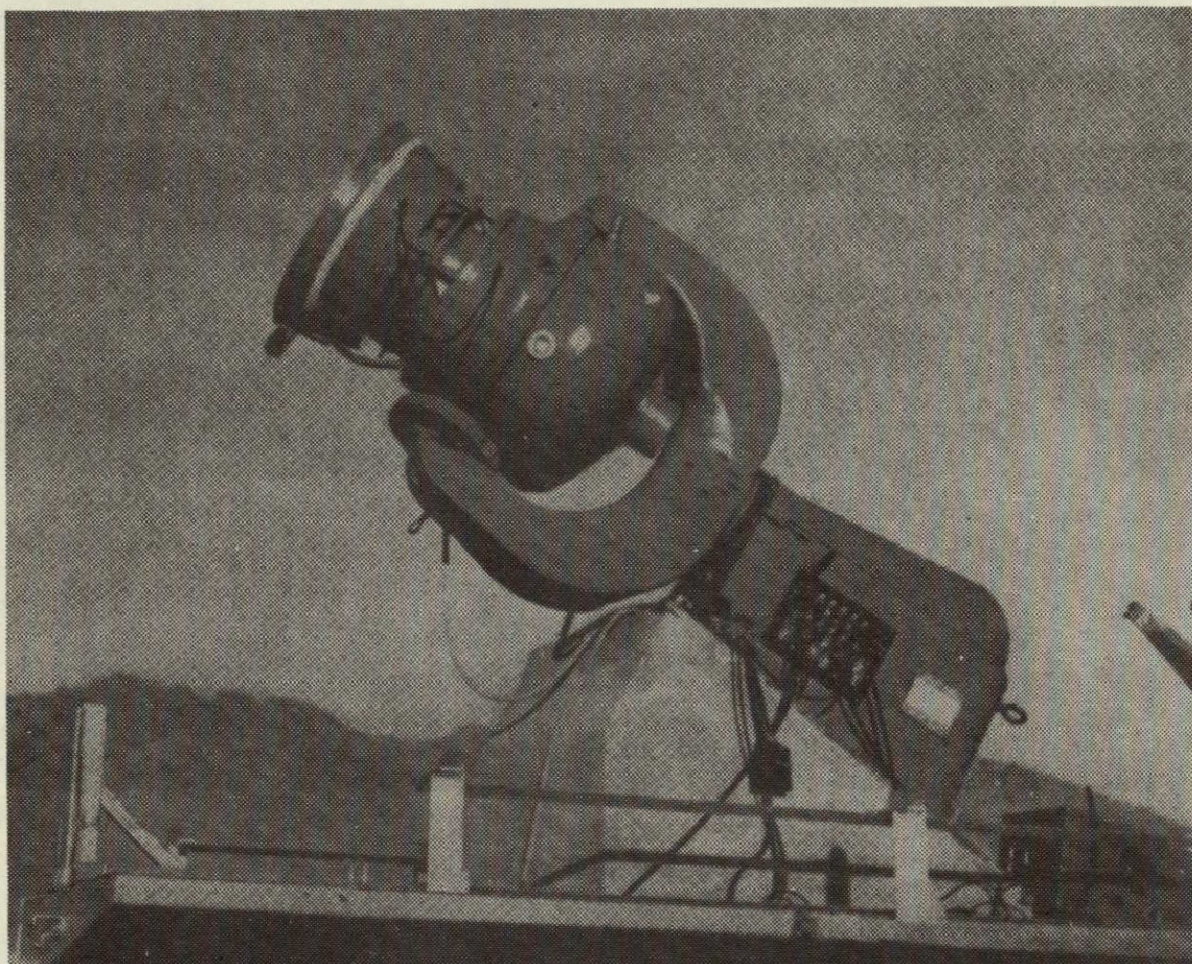
Figure 1.- Super Schmidt Meteor Camera.
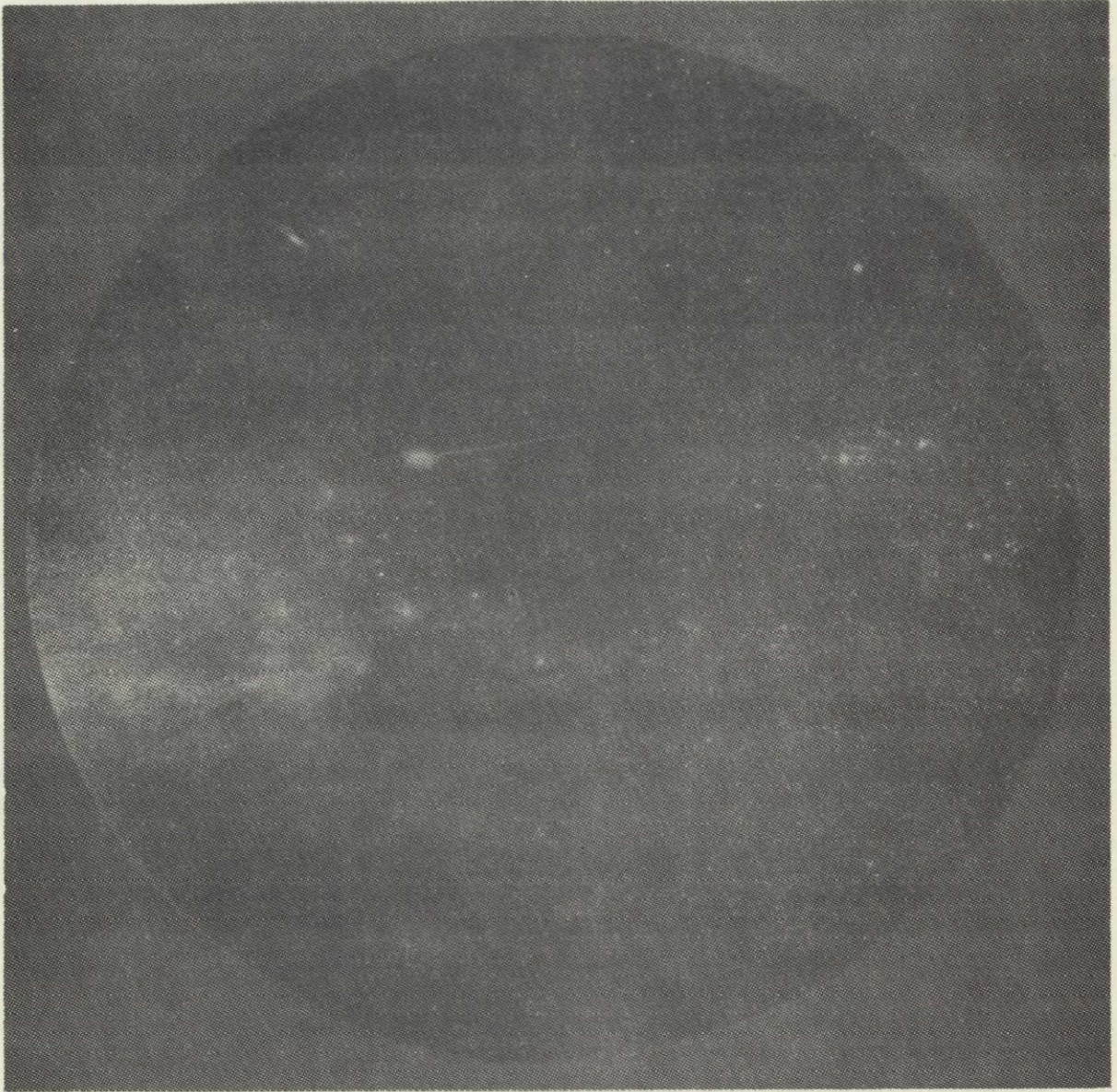
Figure 2.- Photograph taken by a Schmidt camera.
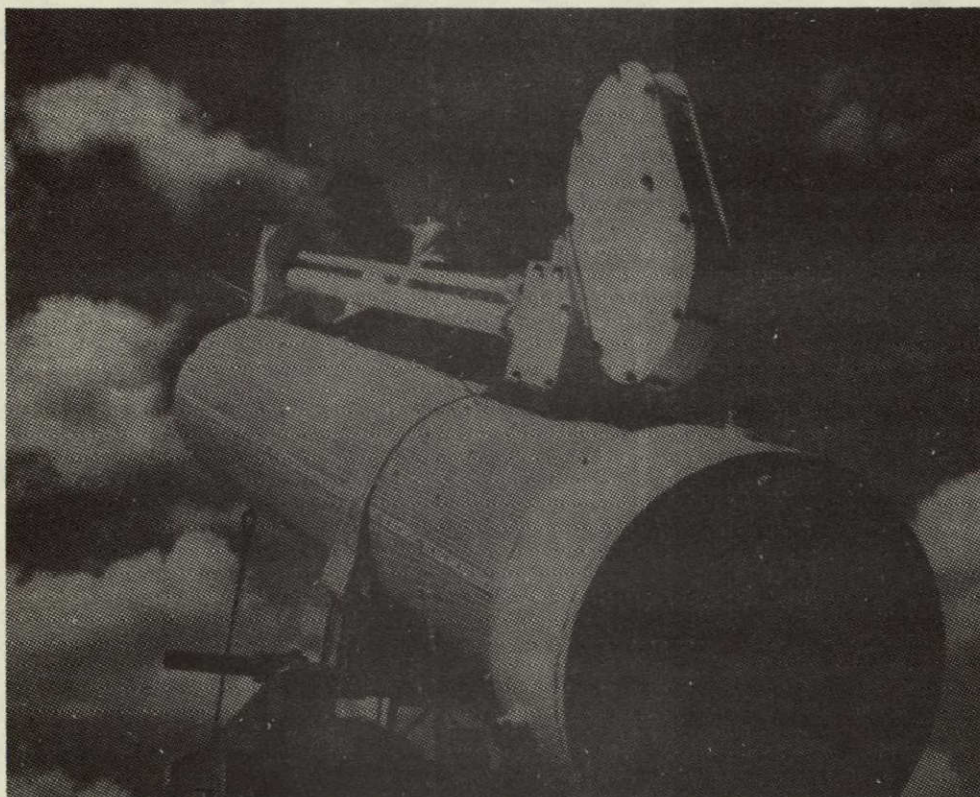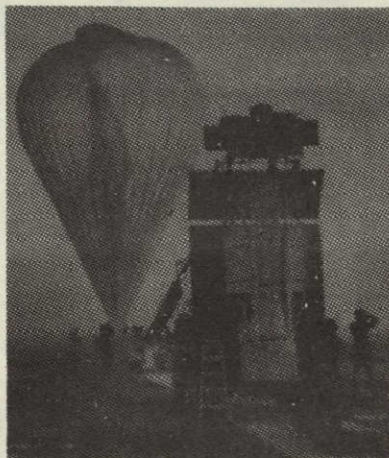
Figure 3.- The Perkin-Elmer solar telescope.

Figure 4.- Photograph of a sunspot.
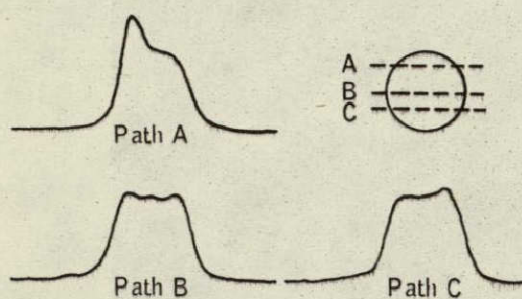
(a) Scans of May 1, 1956.
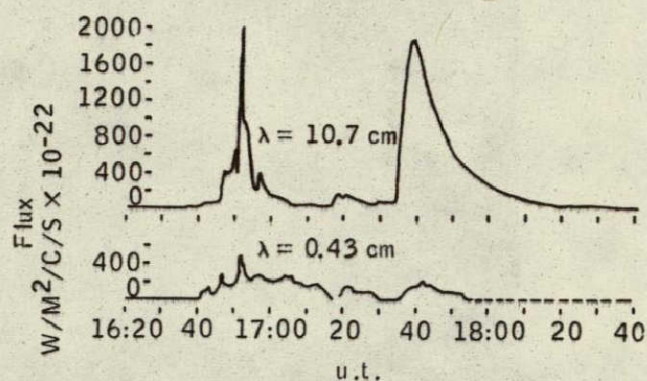
(b) Solar outburst of June 9, 1959.
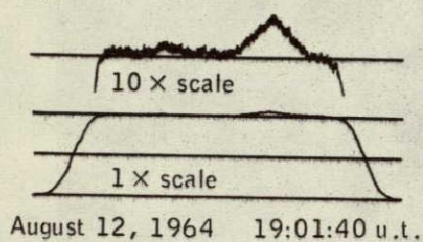
August 12, 1964   19:01:40 u.t.
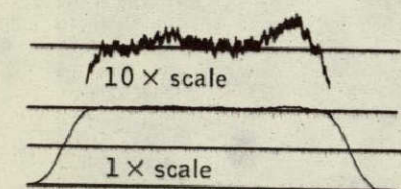
August 13, 1964   17:49:30 u.t.

(c) Scans of August 12 and 13, 1964.
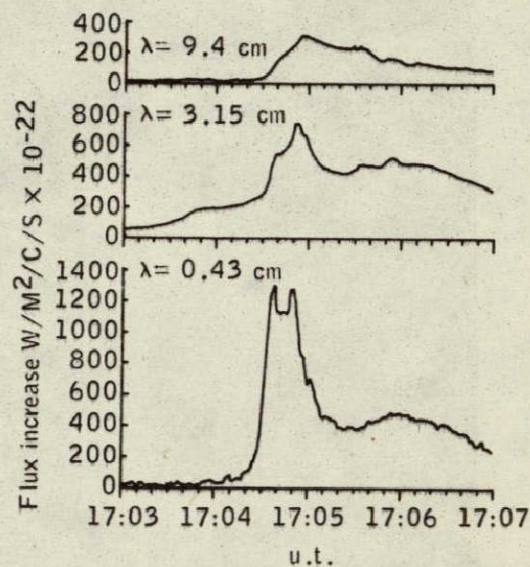
(d) Flux curves for December 1, 1959.

Figure 5.- Results of several solar scans.

Figure 6.- Photograph taken at 1000 feet above the lunar surface by the Ranger 7 spacecraft.
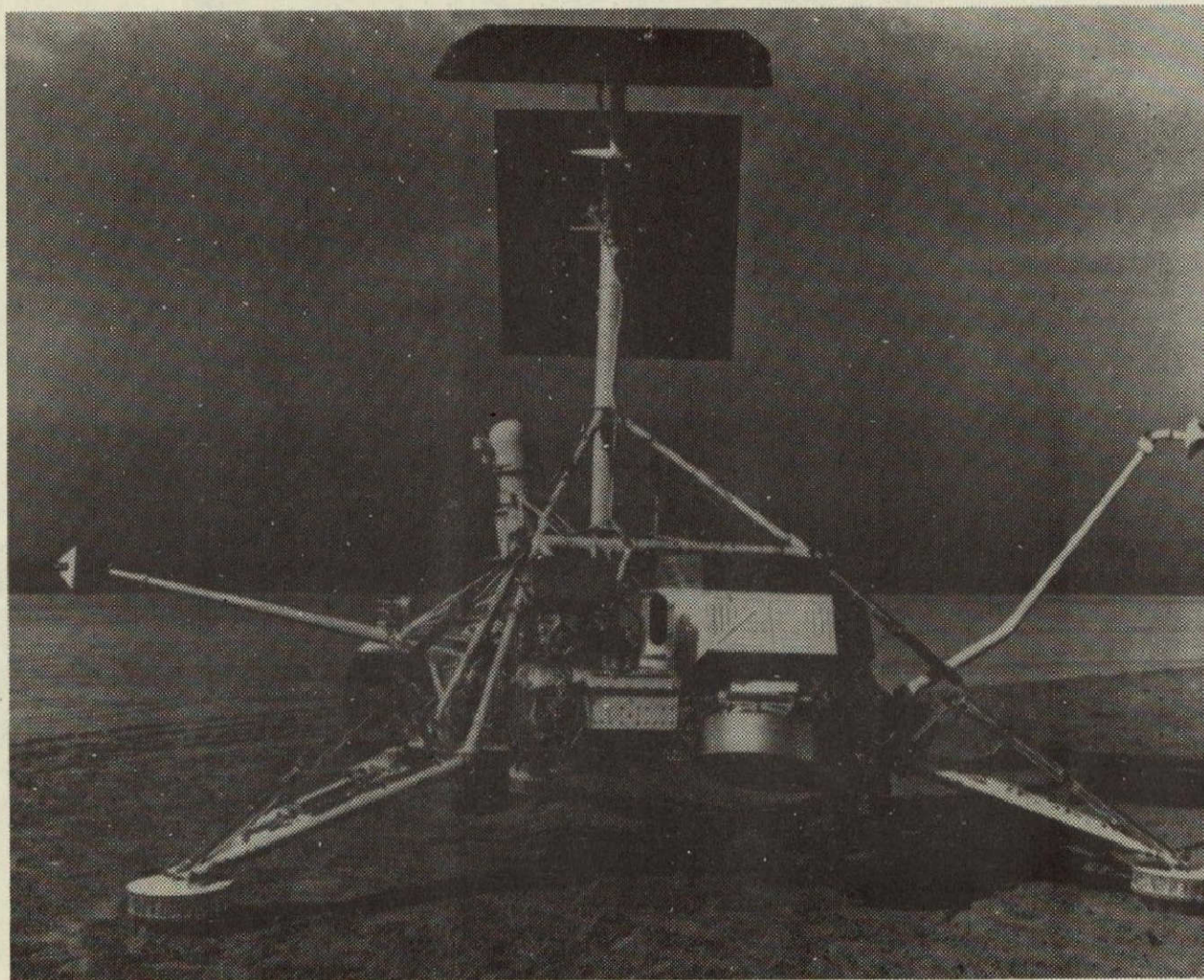
Figure 7.- The Surveyor I spacecraft
(full-scale mockup).

Figure 8.- Photograph taken by the Surveyor I.
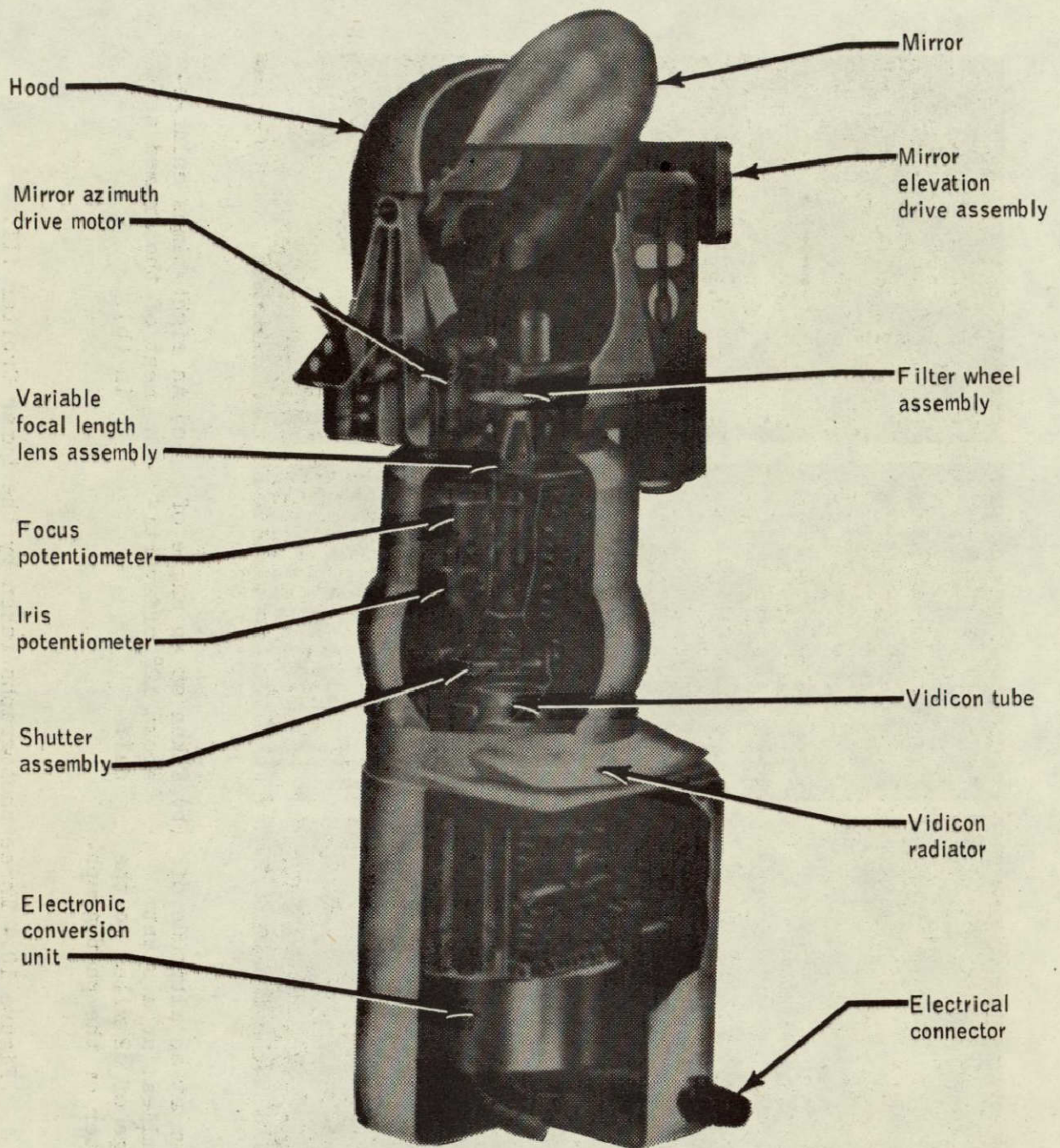
Figure 9.- The television camera of the Surveyor I.
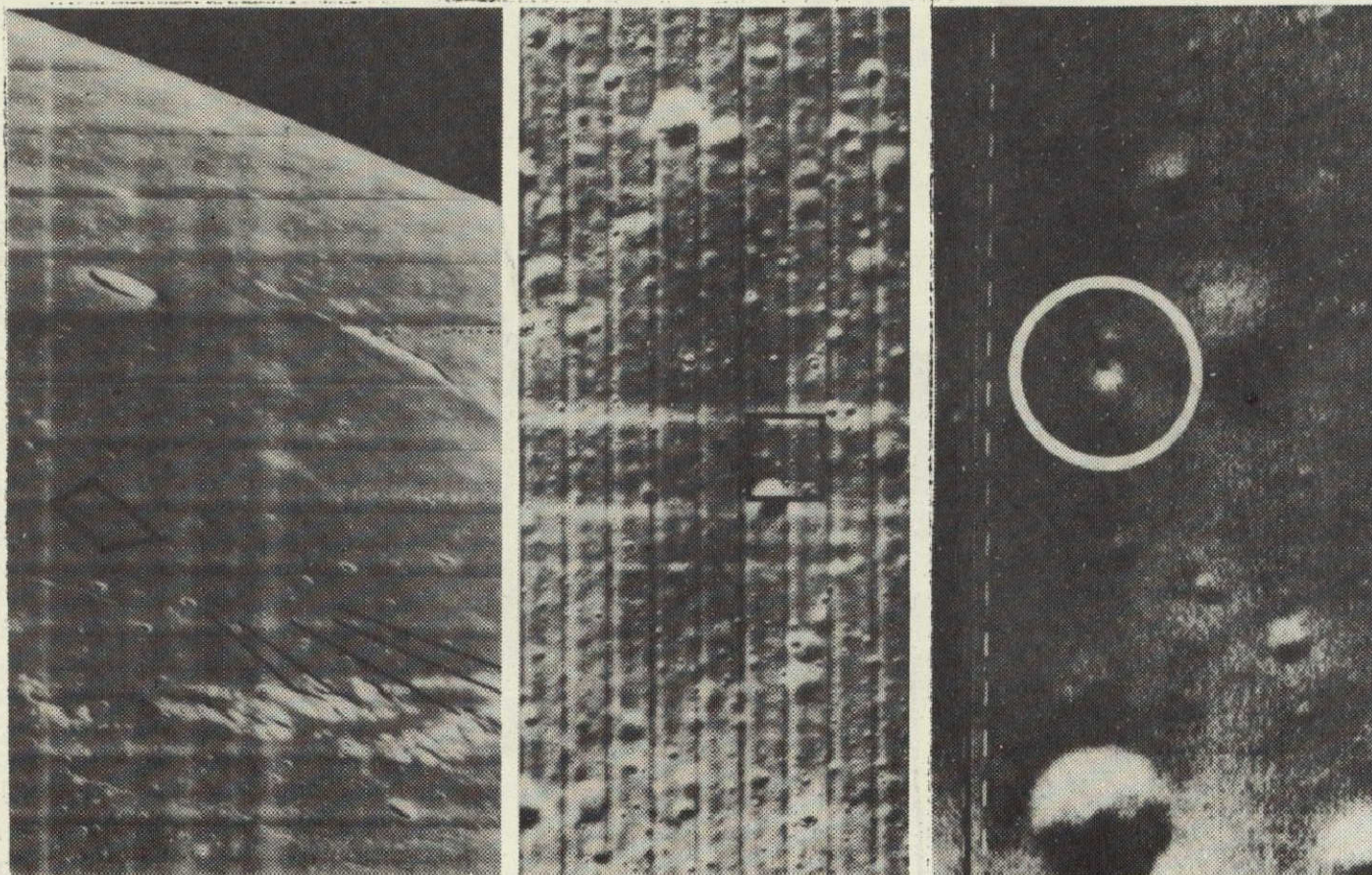
(a) Taken at an altitude of   (b) Taken at an angle of   (c) An eight-times enlarge-
    30 miles, at a slant   about 12° off verti-   ment of the framed area
    range of 82 miles to the   cal.   in (b).
    center of the photograph.

Figure 10.- Three photographs taken by the Lunar Orbiter III.

Figure 11.- A photograph of the crater Copernicus taken by the Lunar Orbiter II.

Figure 12.- Photograph of an area within the crater Hevelius taken from an altitude of 38.5 miles.
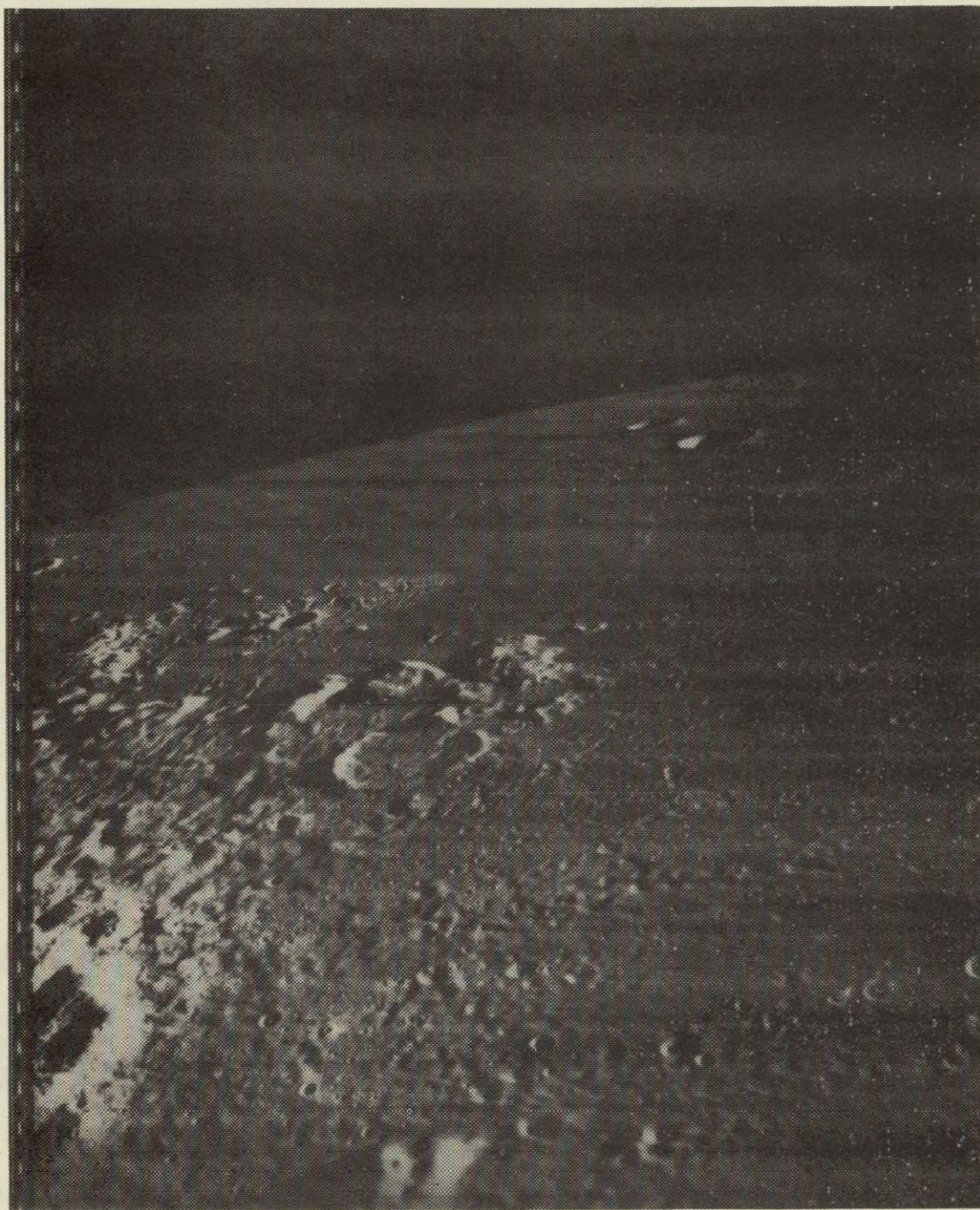
Figure 13.- Photograph of the northern portion of Oceanus Procellarum, containing the landing site of Lunik IX spacecraft.
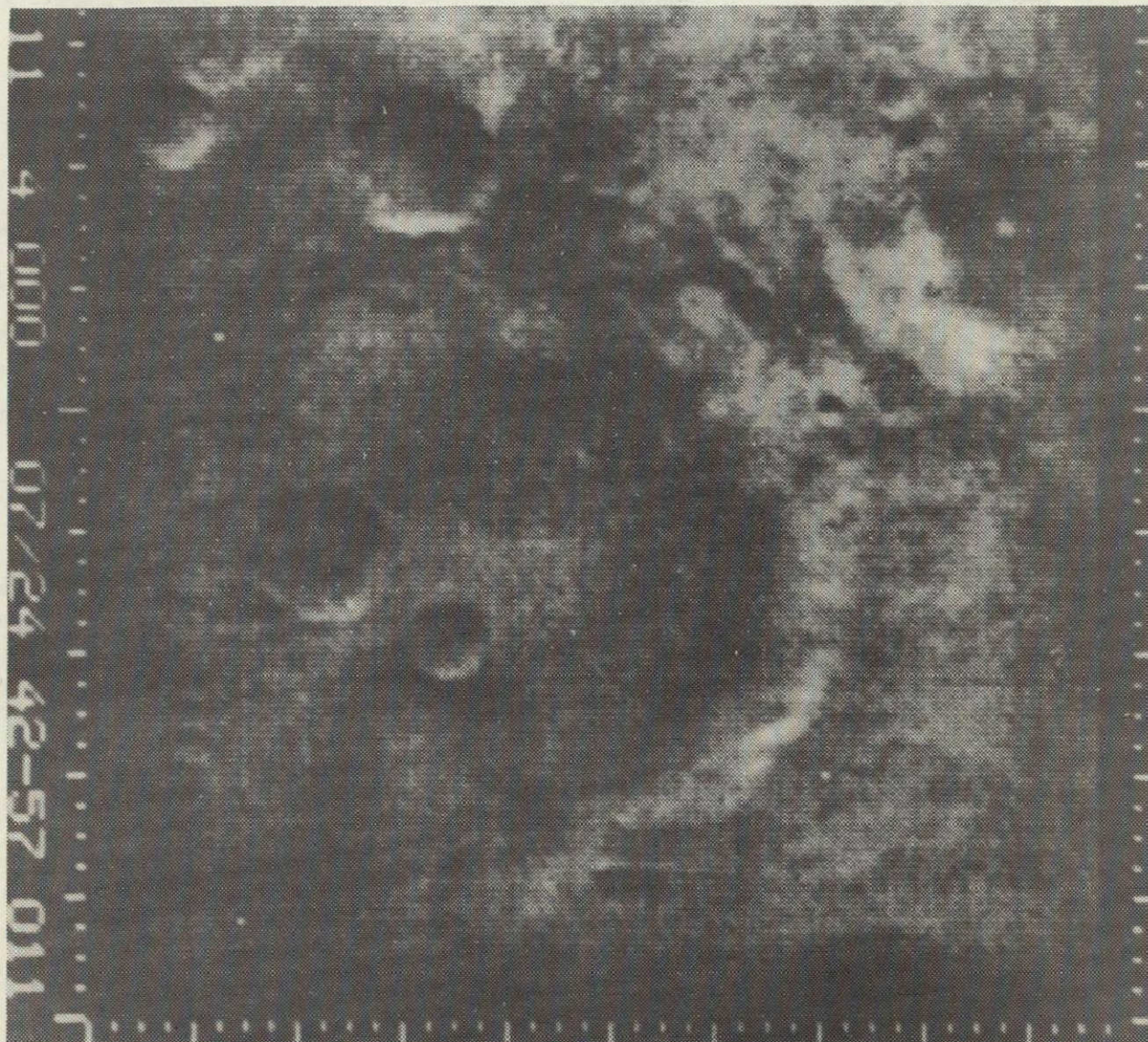
Figure 14.- A photograph taken of the surface of the planet Mars between Mare Sirenum and Mare Cimmerium.
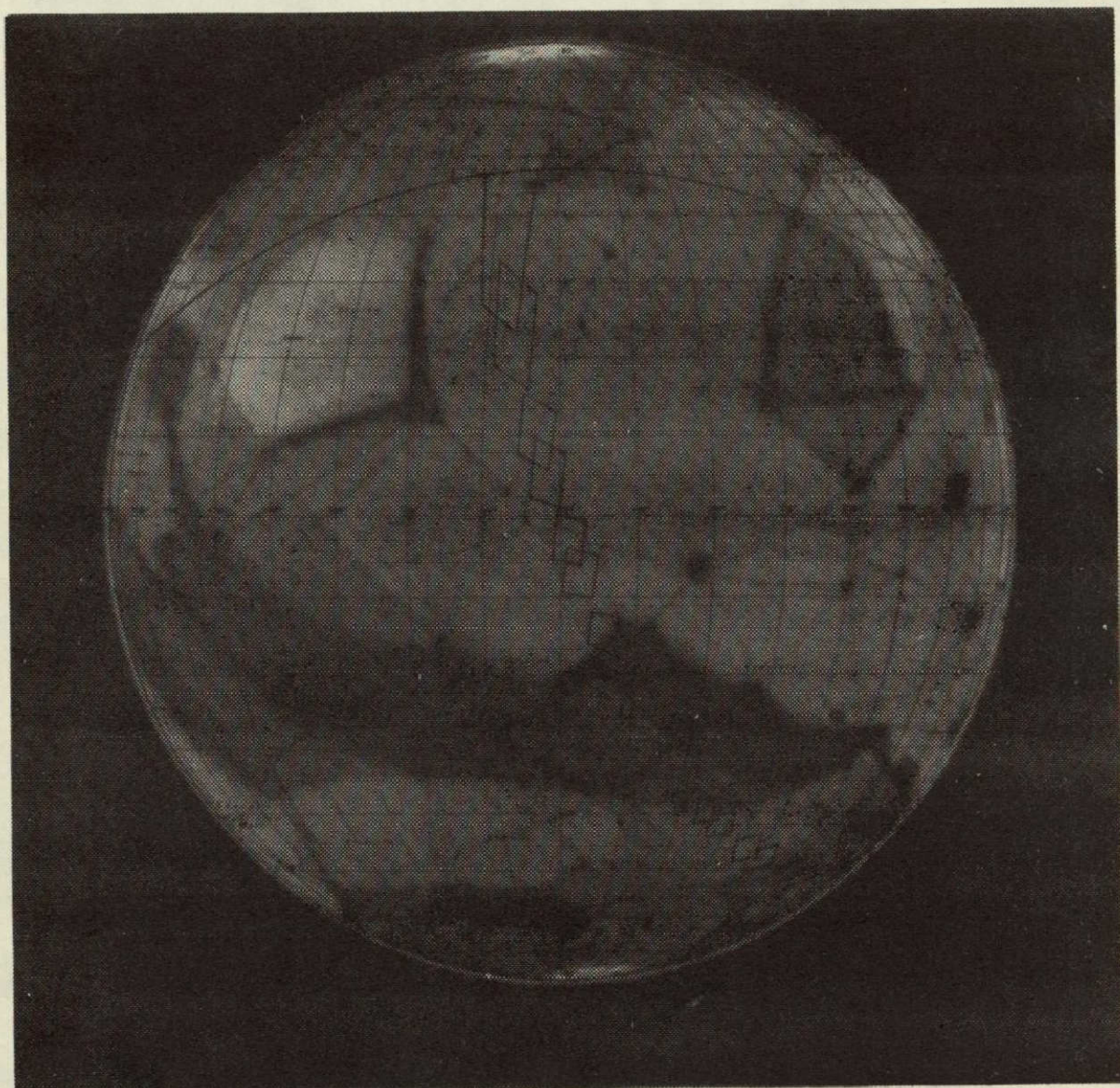
.Figure 15.- A standard representation of the planet Mars.
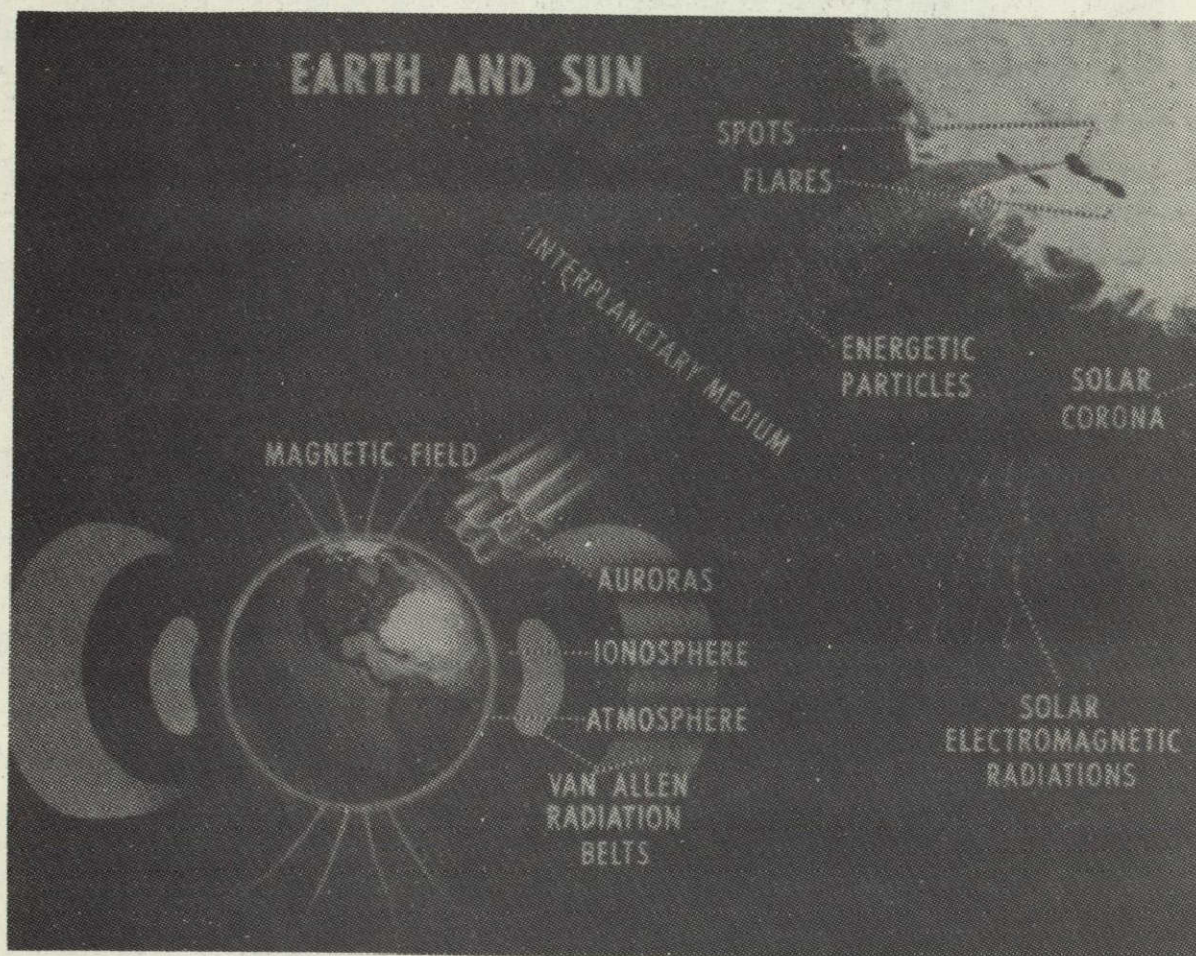
Figure 16.- Diagram of some interesting phenomena in the
Earth-Sun system.
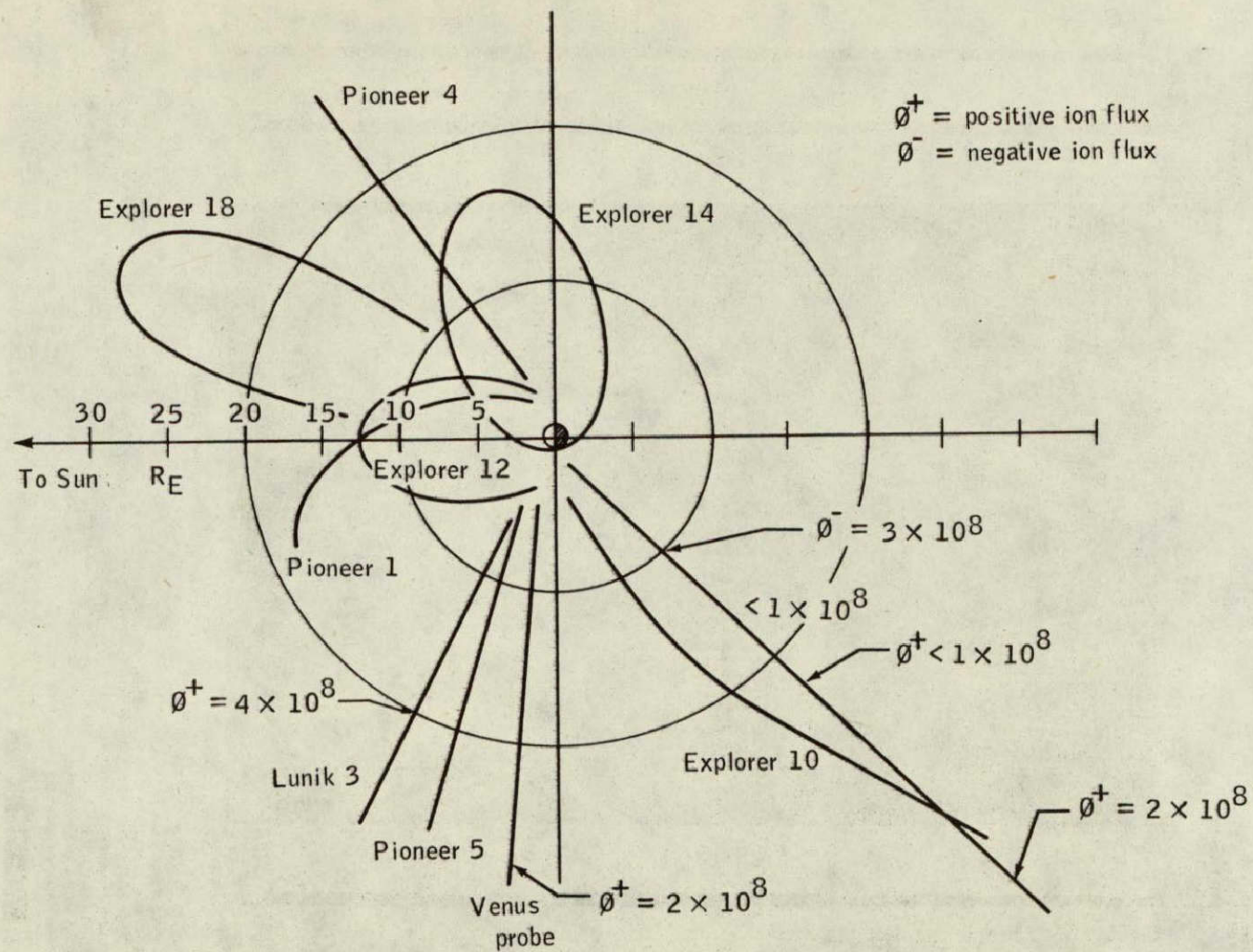
Figure 17.- A graphic summary of several solar-wind experiments.
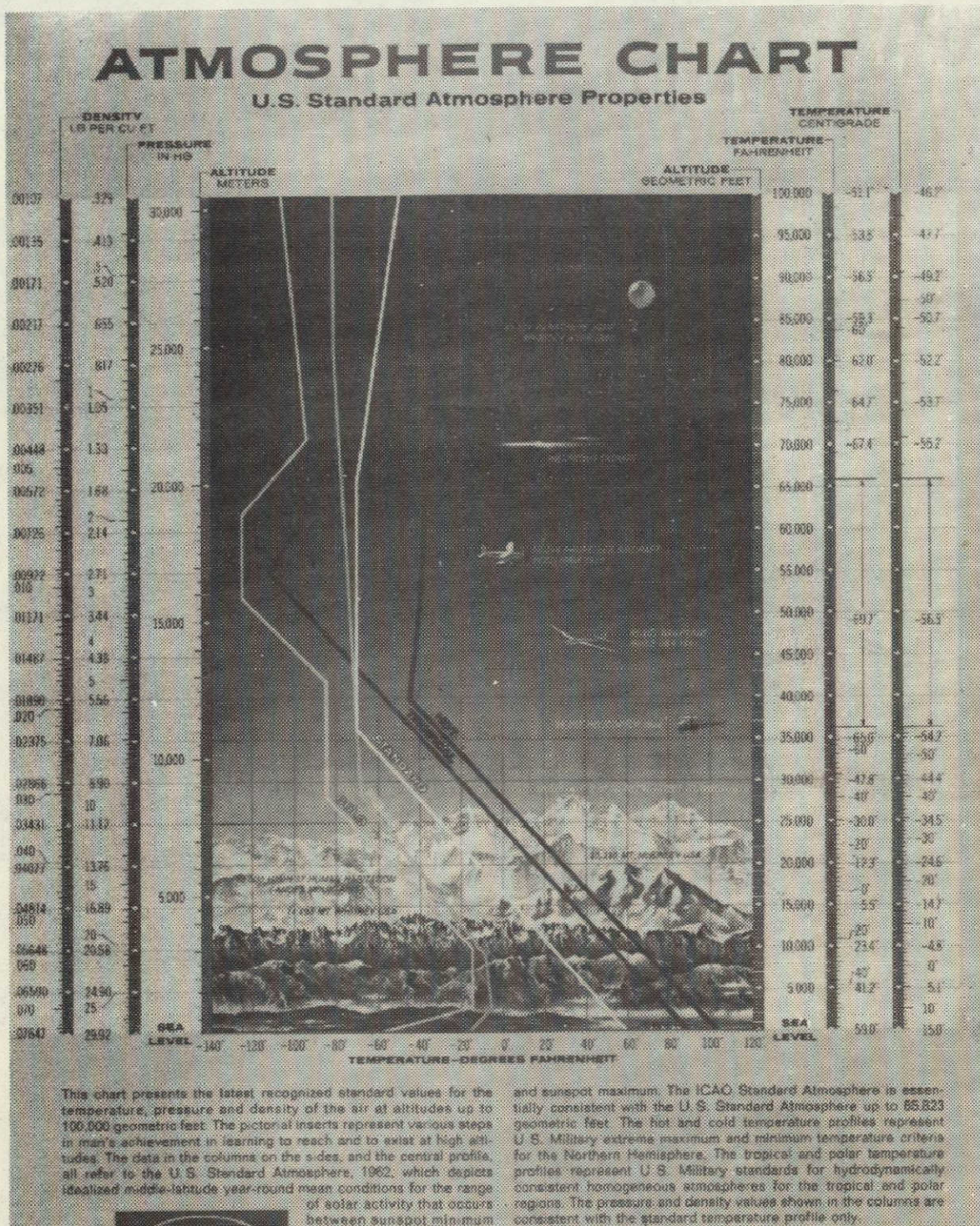
Figure 18.- Atmosphere chart (courtesy of the Garrett Corp.).
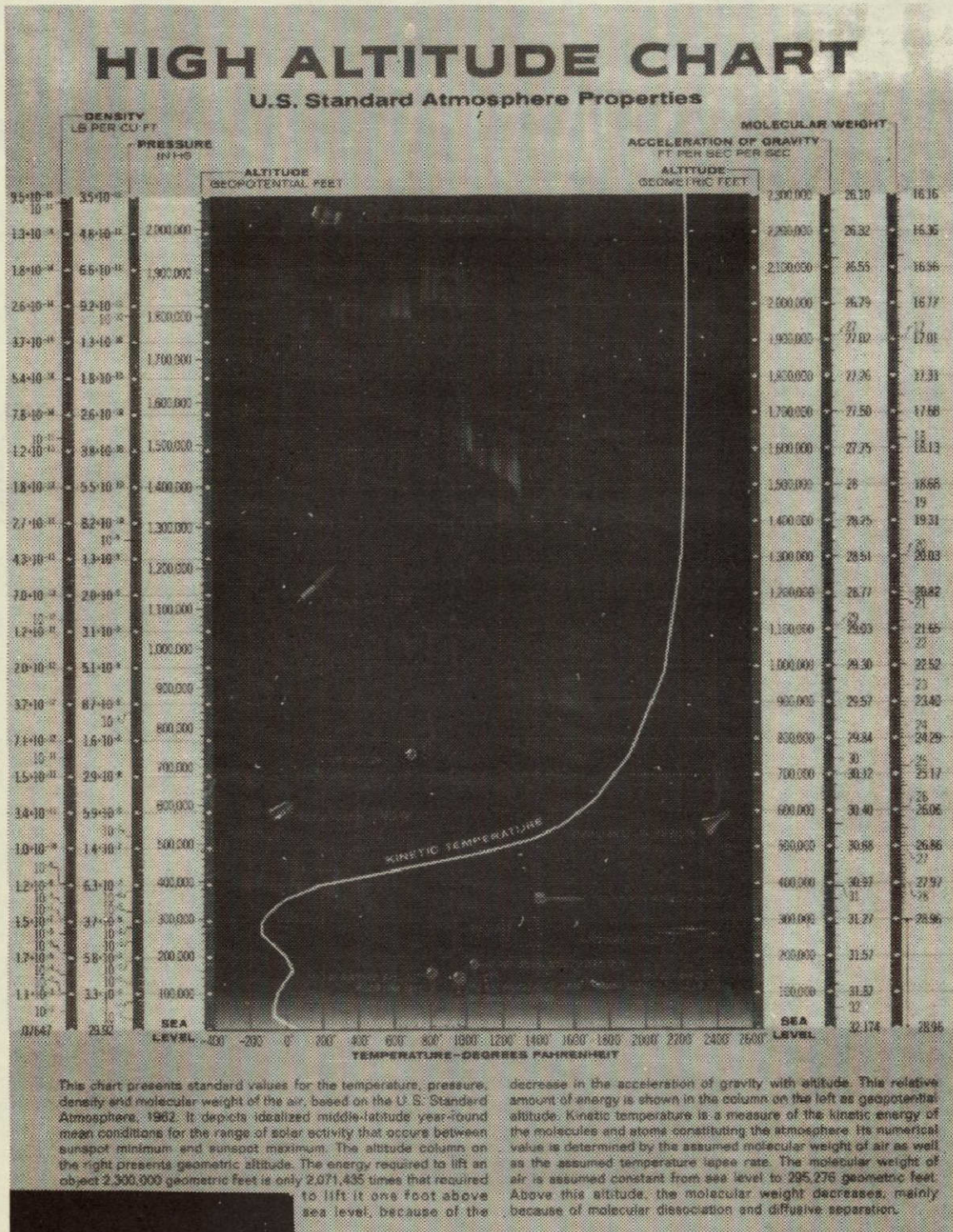
Figure 19.— High-altitude chart (courtesy of the Garrett Corp.).

Figure 20.- The U-2 aircraft.

Figure 21.- The RS-70 aircraft.
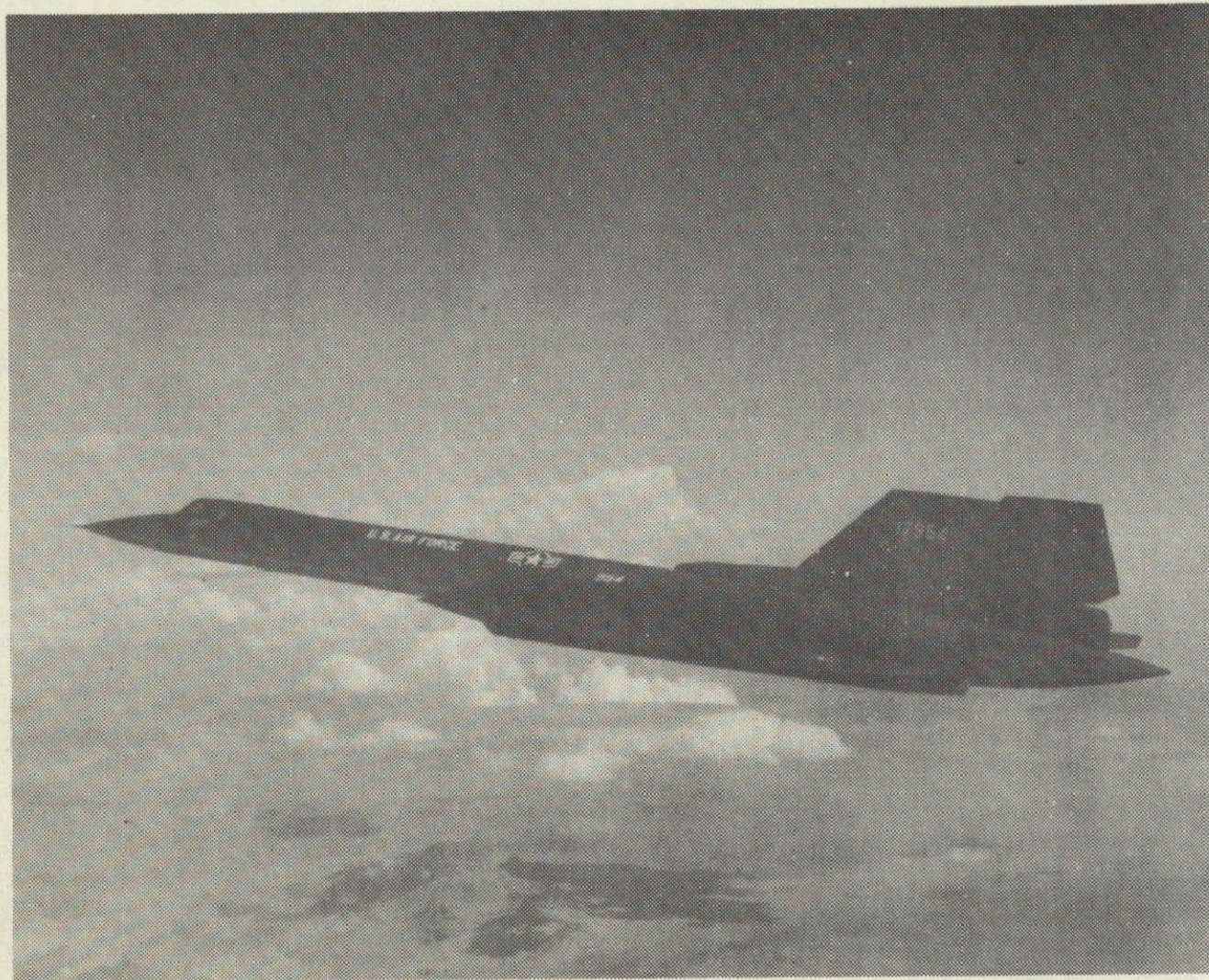
Figure 22.- The SR-71 aircraft.

Figure 23.- The X-15 aircraft (prior to launch from a B-52 mother aircraft).
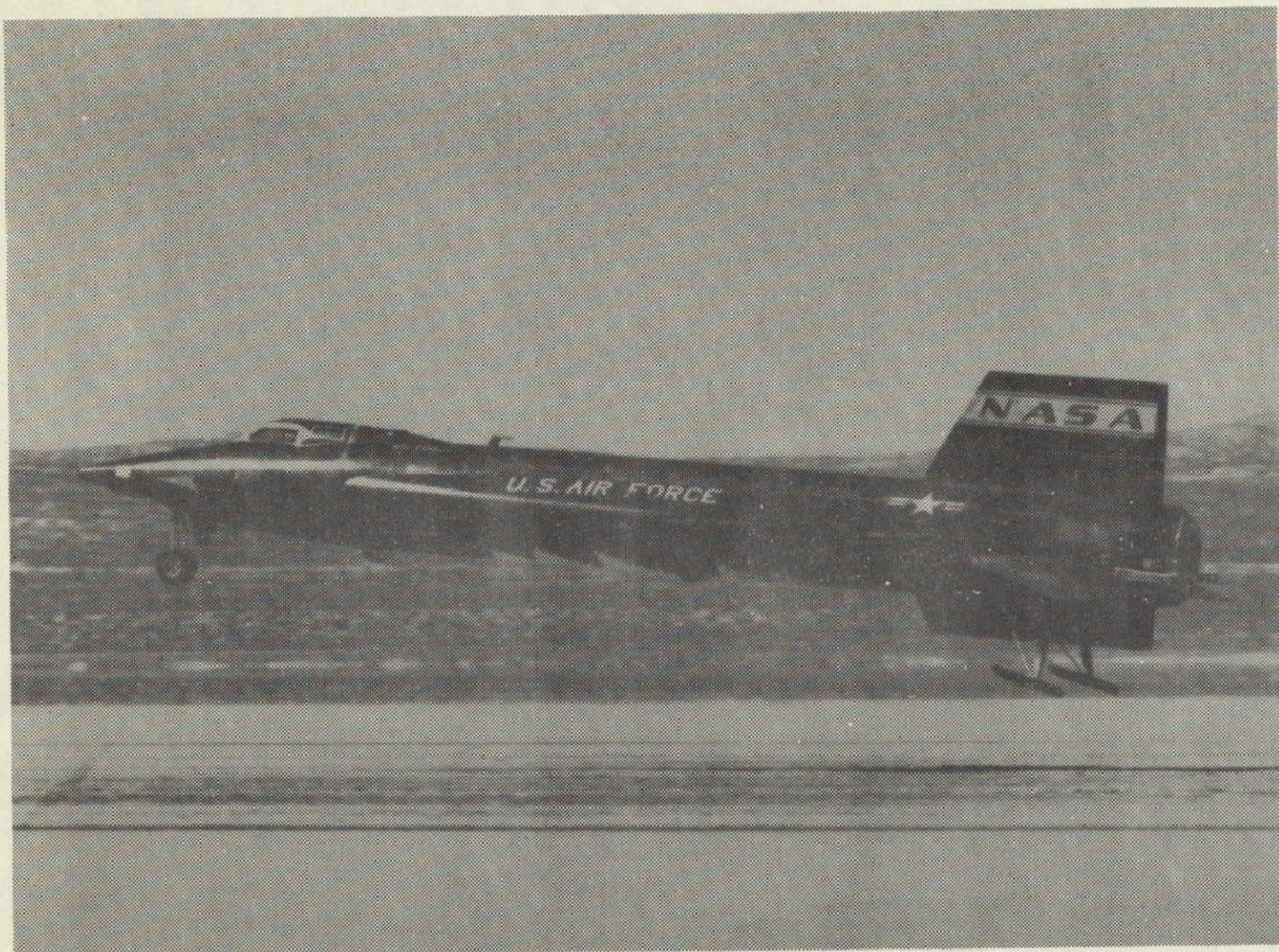
Figure 24.- The X-15 aircraft, landing configuration.
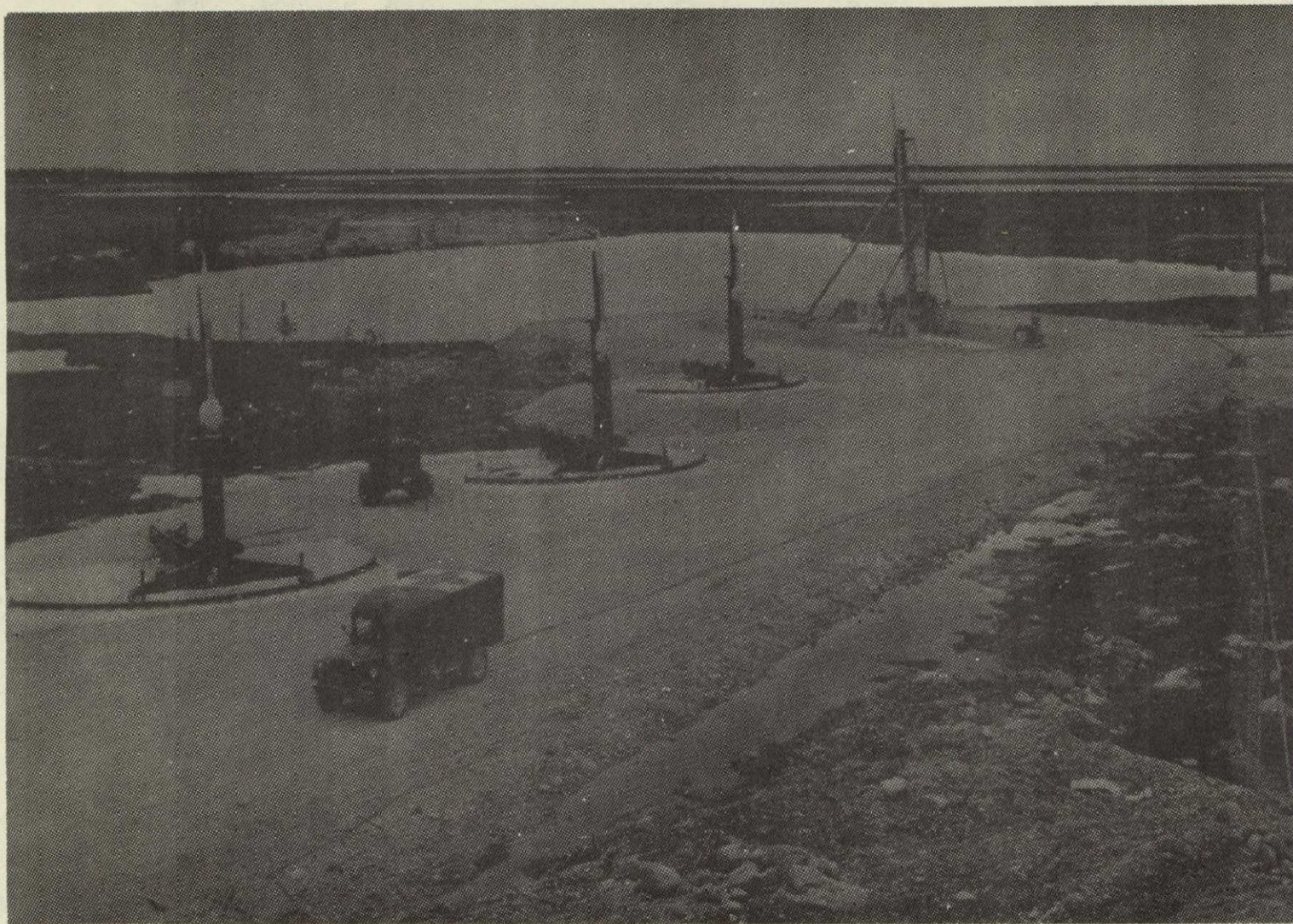
Figure 25.- Nike-Cajun and Black Brant outdoor launchers,
Fort Churchill Rocket Research Range, Manitoba, Canada.
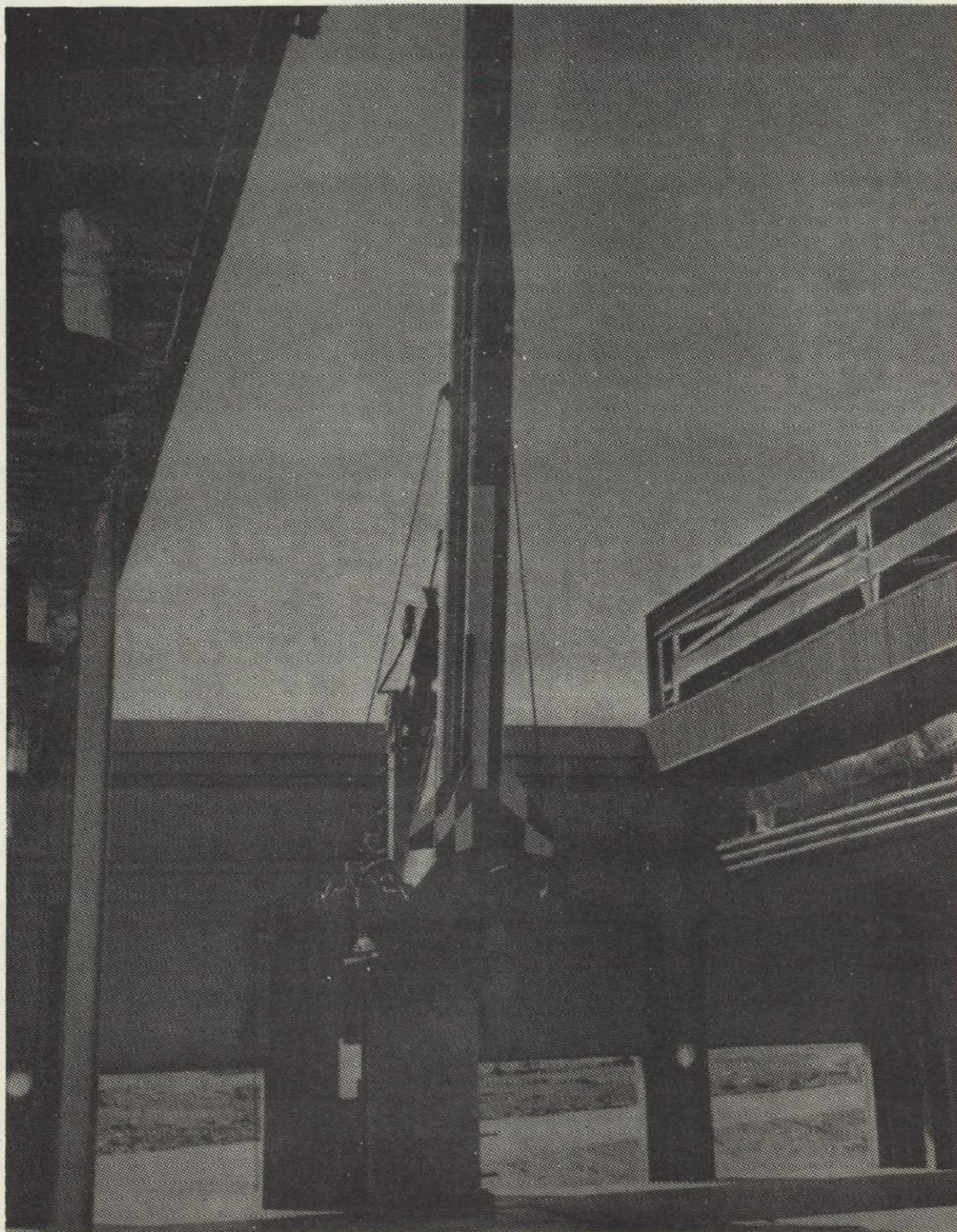
Figure 26.- A sounding rocket.
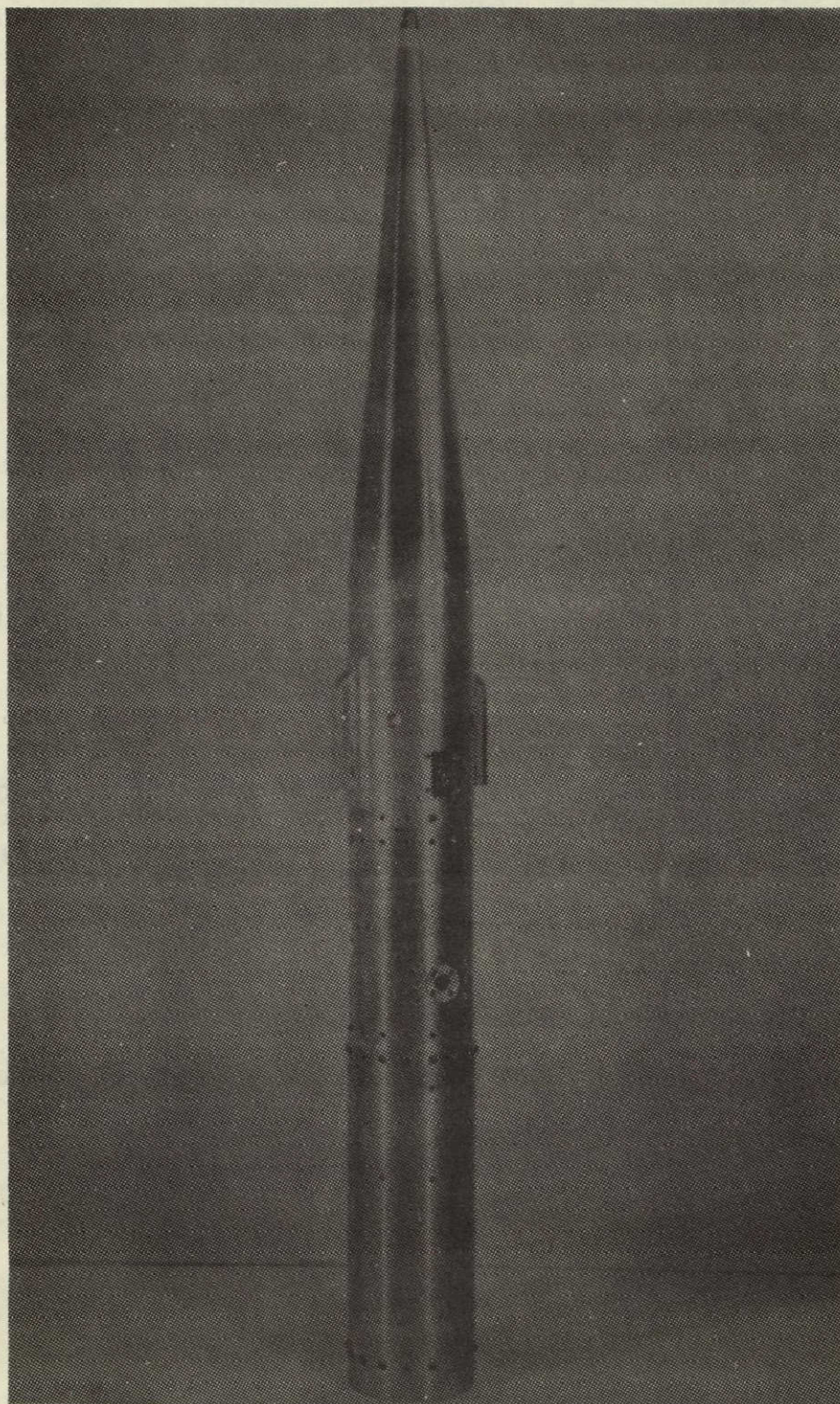
Figure 27.- A Langmuir probe.

Nose probe

Nose cone

Nose probe
connector

Magnetic aspect
sensor

Langmuir probe

Payload shell
(probe)

Battery pack

Antenna phasing

Transmitter

VCO and baroswitch

Regulator and
converter

Coupling ring

Payload shell
(chemical)

Timers and
battery packs

Arming area

Umbilical

Igniters for sodium
or valves for TMA

Sodium or TMA
canister

Arming door located
approx 135° from
umbilical

Figure 28.- Diagram of a Langmuir probe.
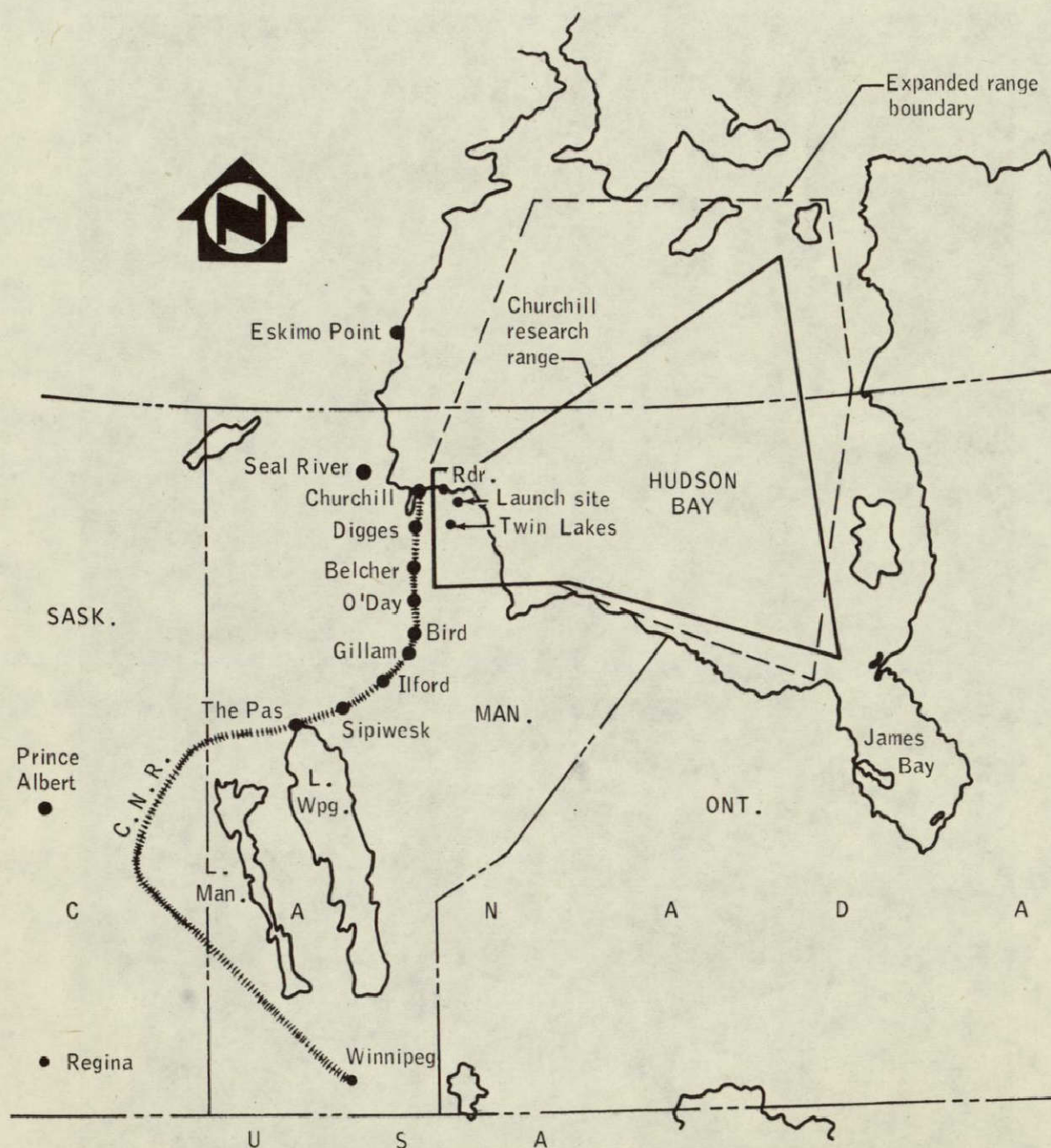
Figure 29.- Relative positions of the launch and observation sites at the Fort Churchill Rocket Research Range, Manitoba, Canada.

Figure 30.- The P-3A aircraft, NASA 927.

Figure 31.- Dual 70-mm camera system.

73
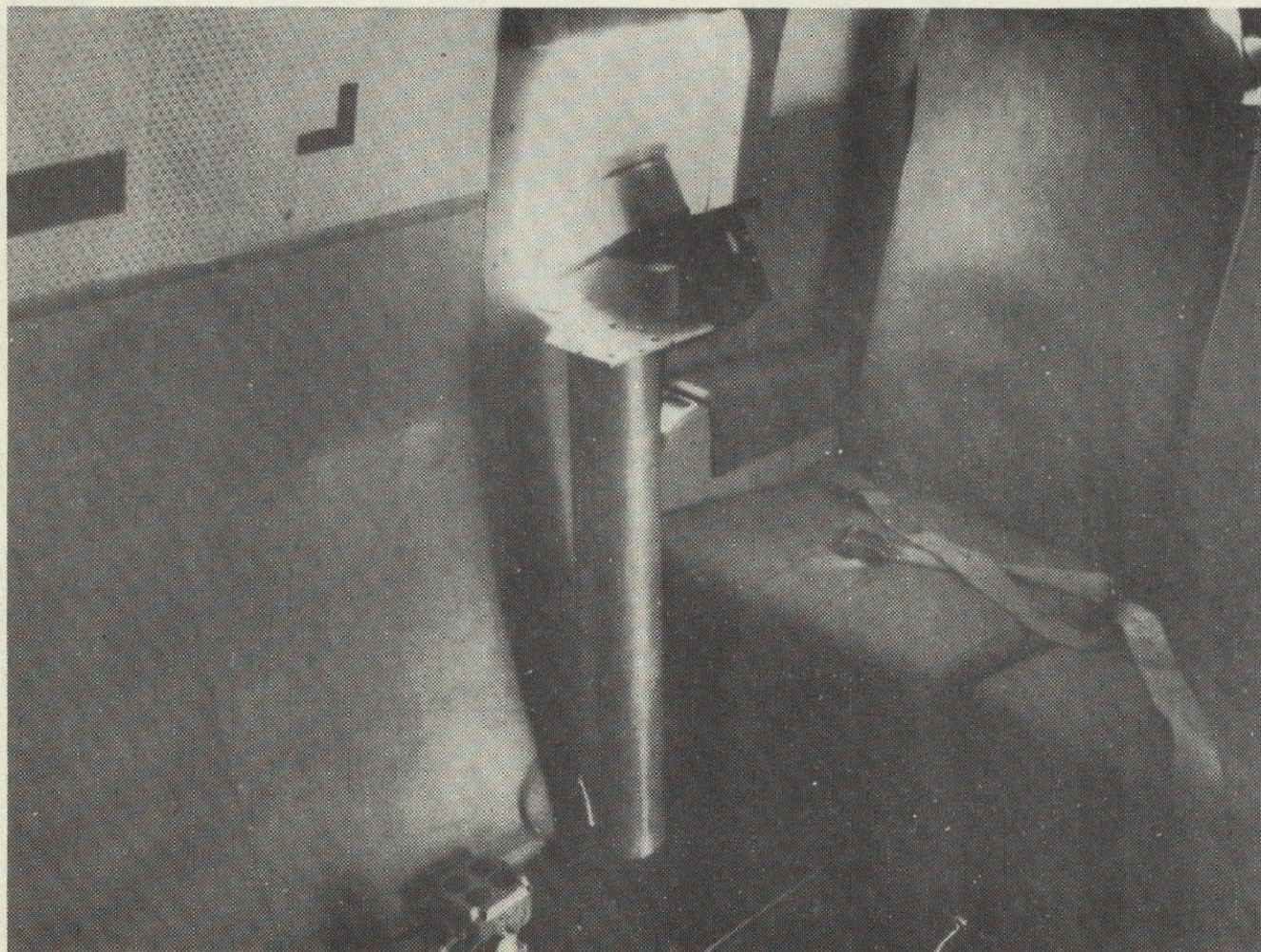
Figure 32.- 70-mm camera system.
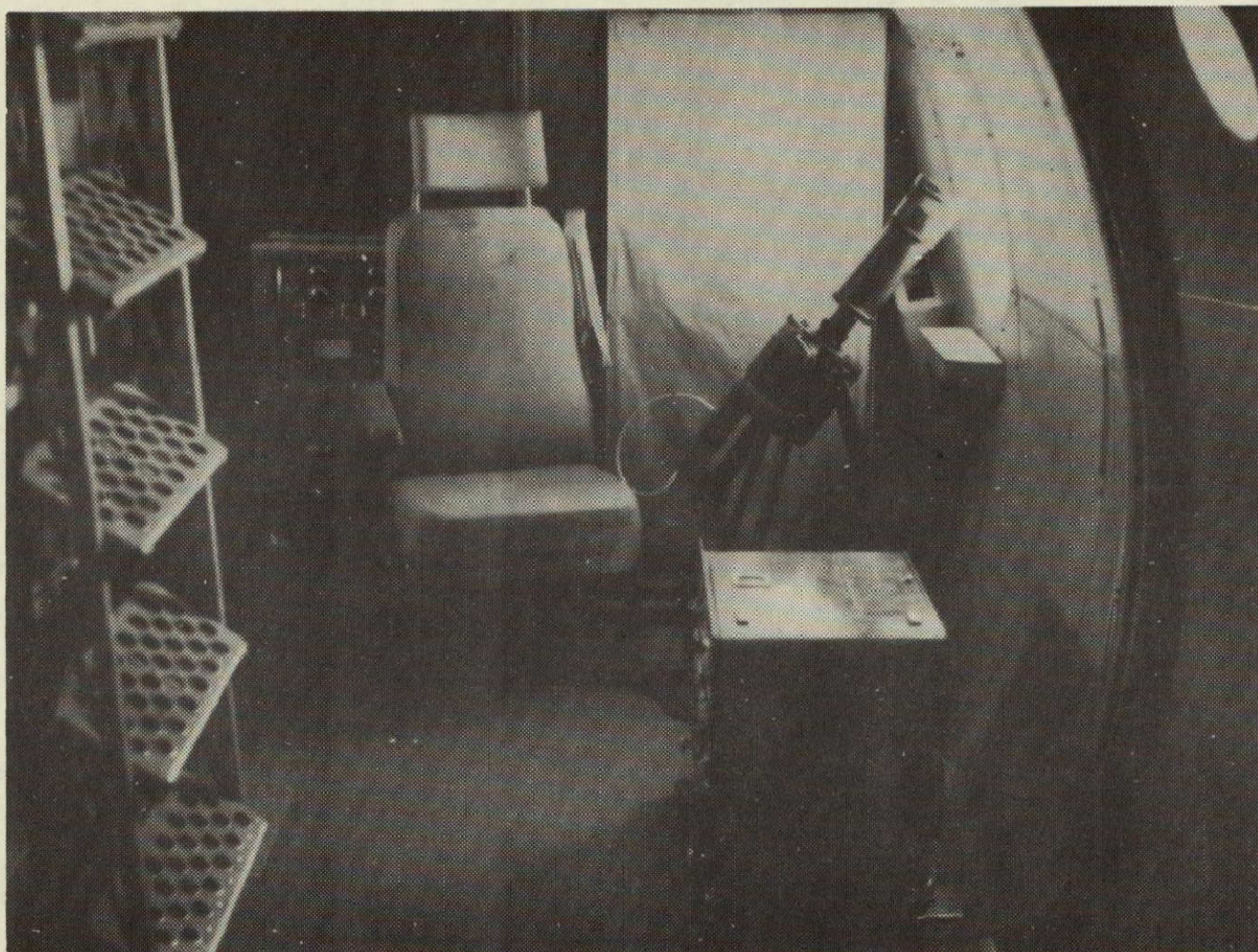
Figure 33.- Spectrophotometer system, Centre National de la Recherche Scientifique, Service d'Aeronomie, France.
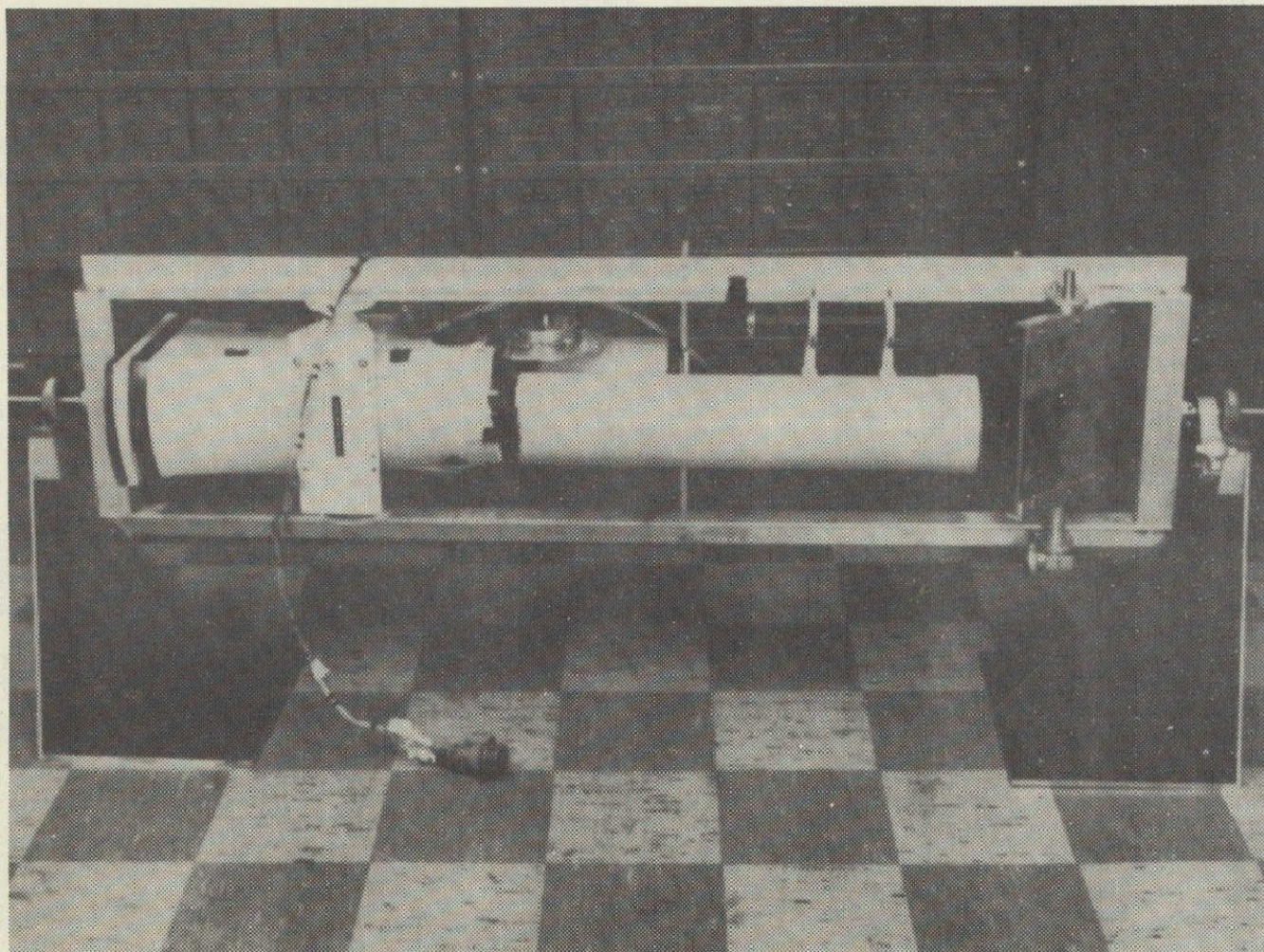
Figure 34.- Johns-Hopkins spectrometer system.

Figure 35.- Spectrometer recorder system.
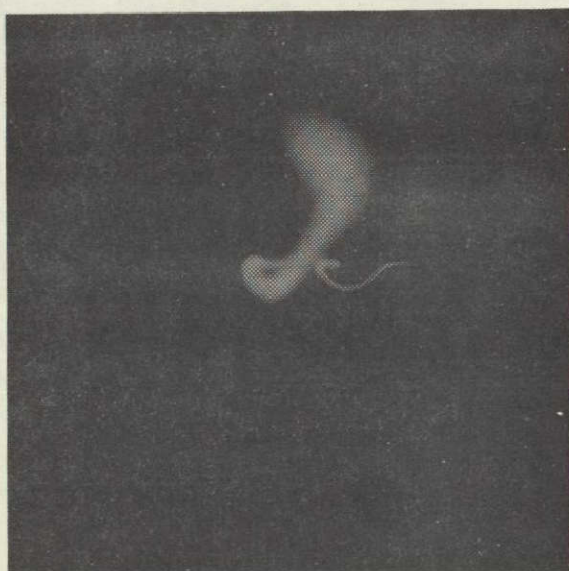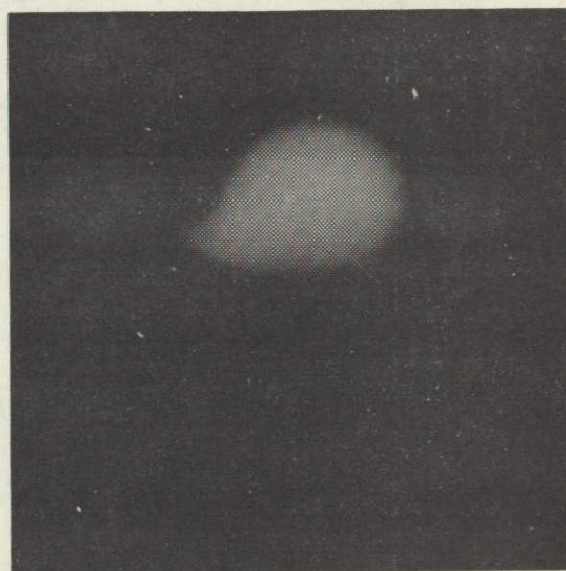
Figure 36.- A sequence of photographs of a typical rocket
release of trimethylaluminum gas.
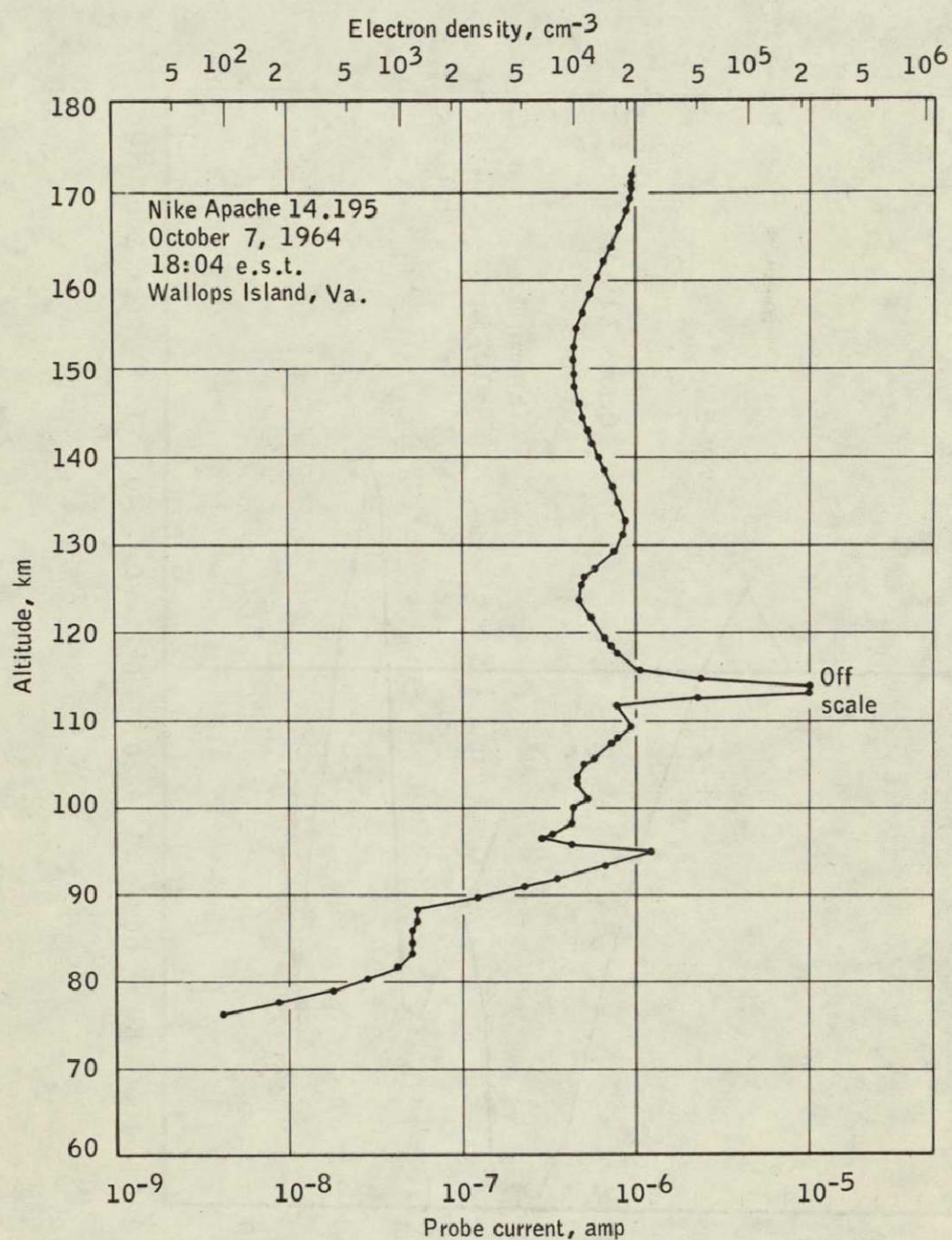
Figure 37.- Electron density profile from the Nike-Apache shot at Wallops Island, Virginia, October 1964.

E-W

N-S

October 7, 1964
18:08 e.s.t.

T=4 min
R=107 km

West
South

East
North

Wind speed , m/sec

Height, km
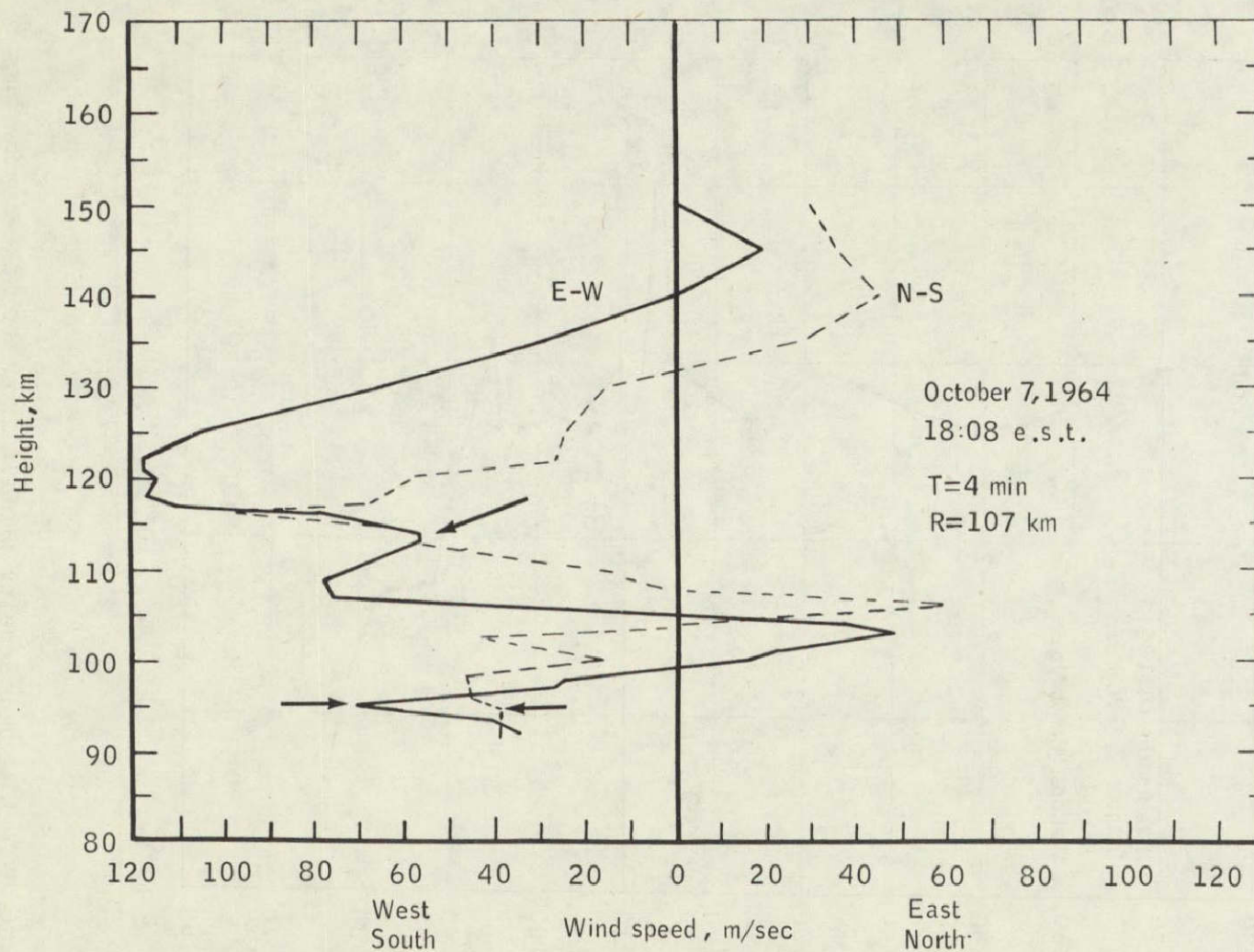
Figure 38.- East-west and north-south components of wind profiles from the Nike-Apache shot
(arrows show regions of increased electron density).

October 7, 1964
p.m.
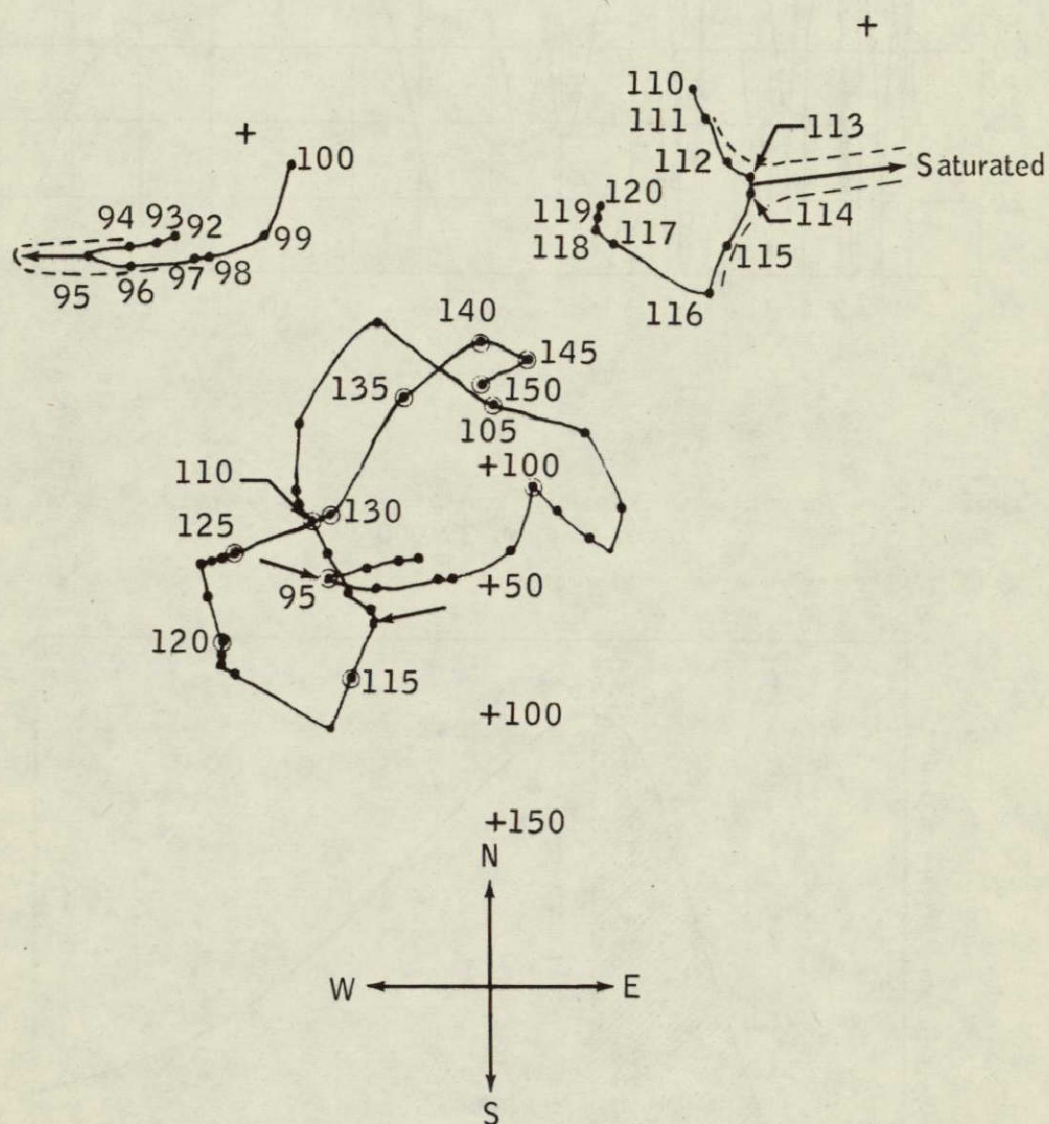
Figure 39.- Hodograph of the wind profile from the Nike-Apache shot.
Regions of enhanced electron density are marked by arrows, shown
separately on the same scale. Dashed lines represent general
region covered by the ionized layer.
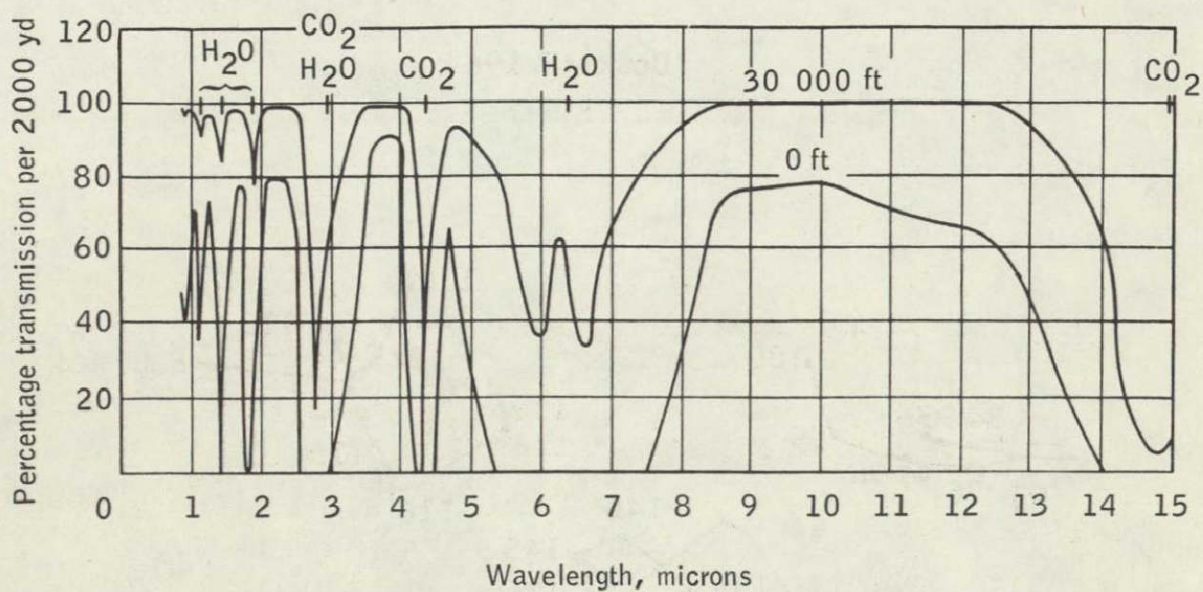
Figure 40.- Percentage transmission at various wavelengths at sea level and at 30 000 feet.
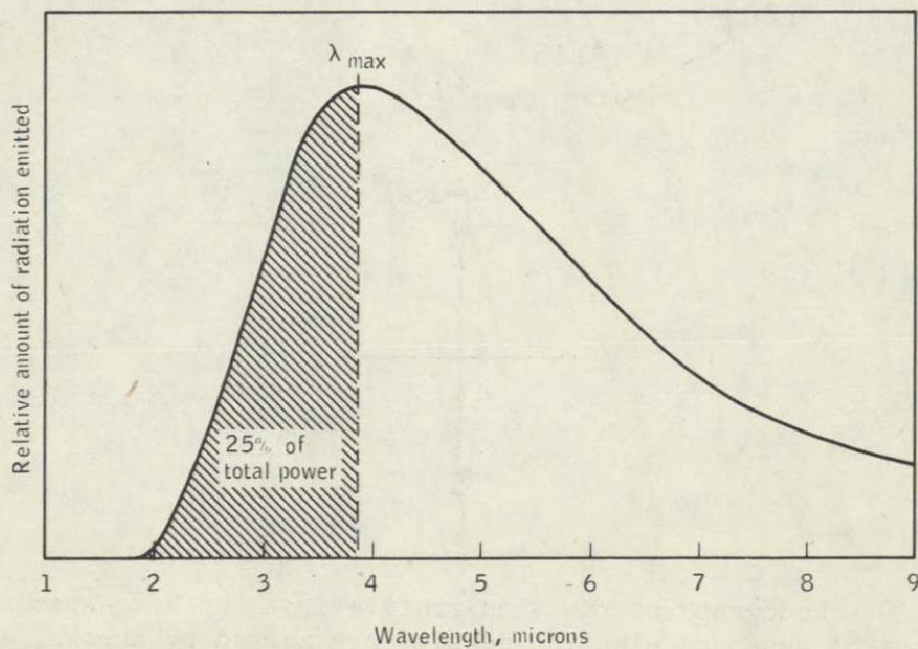
Figure 41.- Black body radiation curve.
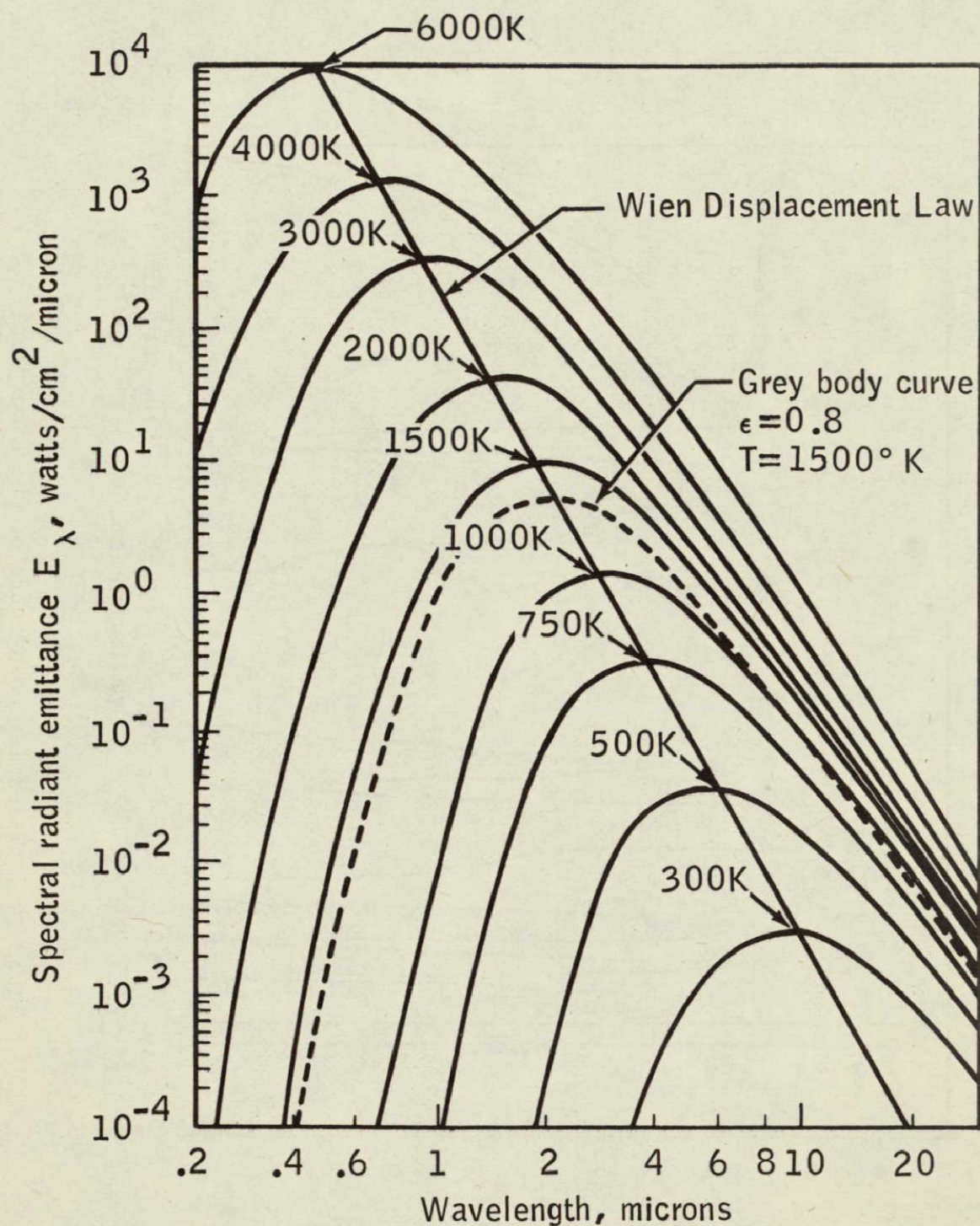
Figure 42.- An illustration of the Wien Displacement Law.
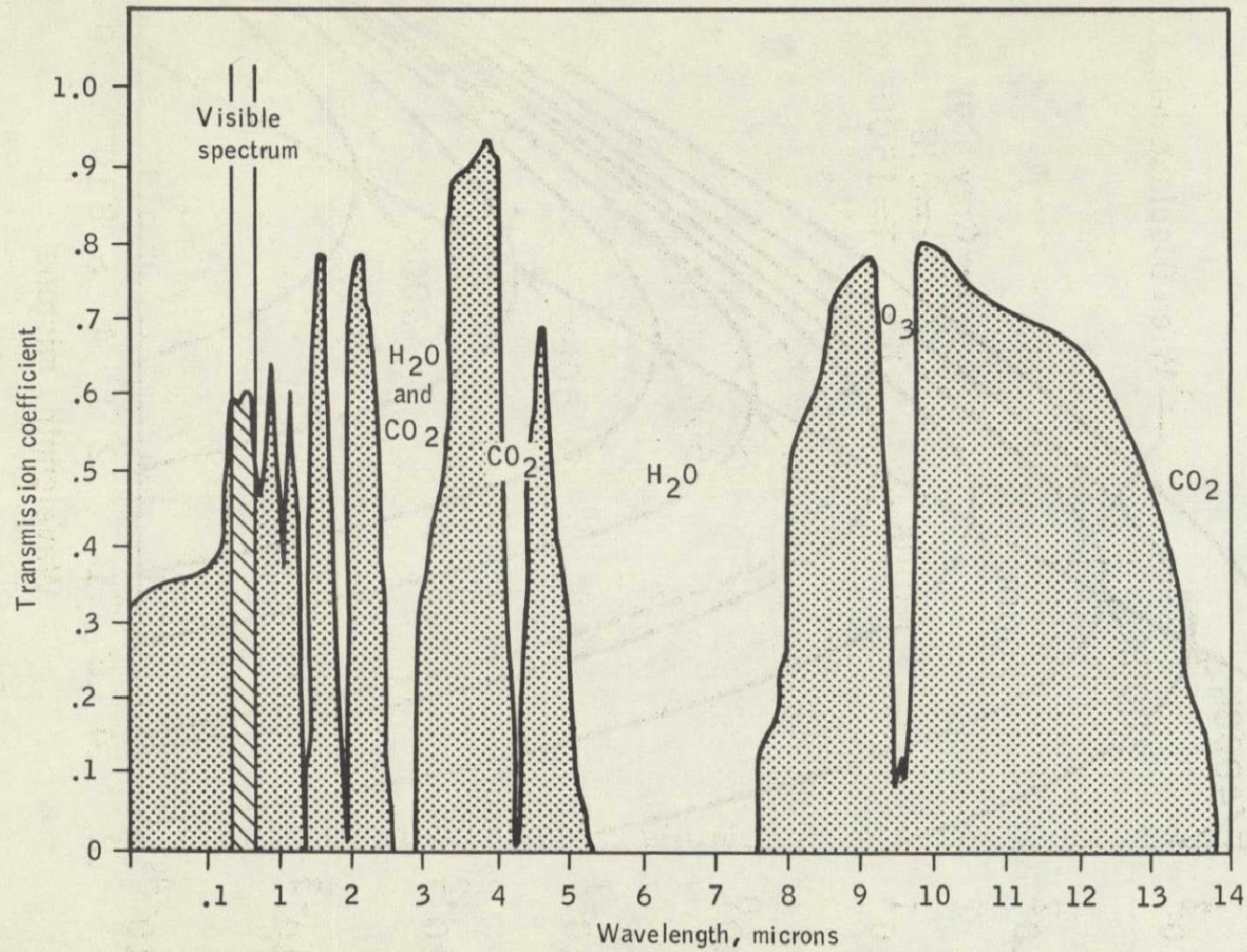
Figure 43.- Transmission spectra of the atmosphere.

Wavelength	Frequency, MHz		Sensor systems
.03 Å	10^{14}	Gamma rays	
.3 Å	10^{13}	X-rays (hard)	Scintillation counters; Gamma-ray spectrometers
3.0 Å	10^{12}	X-rays (soft)	
30 Å	10^{11}		Scanners with filtered photomultipliers; image orthicons
300 Å	10^{10}	Ultraviolet	Conventional cameras and and films
.3 μ	10^{9}	Visible light near IR	Cameras with IR-sensitive films; solid-state detectors in scanners and radiometers
3.0 μ	10^{8}	Intermediate IR	
30 μ	10^{7}	Far IR	Solid-state detectors in scanners and radiometers
300 μ	10^{6}		
.3 cm	10^{5}	EHF	
3.0 cm	10^{4}	SHF	Radar; rf receivers in scanners and radiometers
30 cm	10^{3}	UHF	
3.0 m	10^{2}	VHF	
30 m	10	HF	Electromagnetic pulse techniques
300 m	1	LF and MF	

Figure 44.- The electromagnetic spectrum.

86
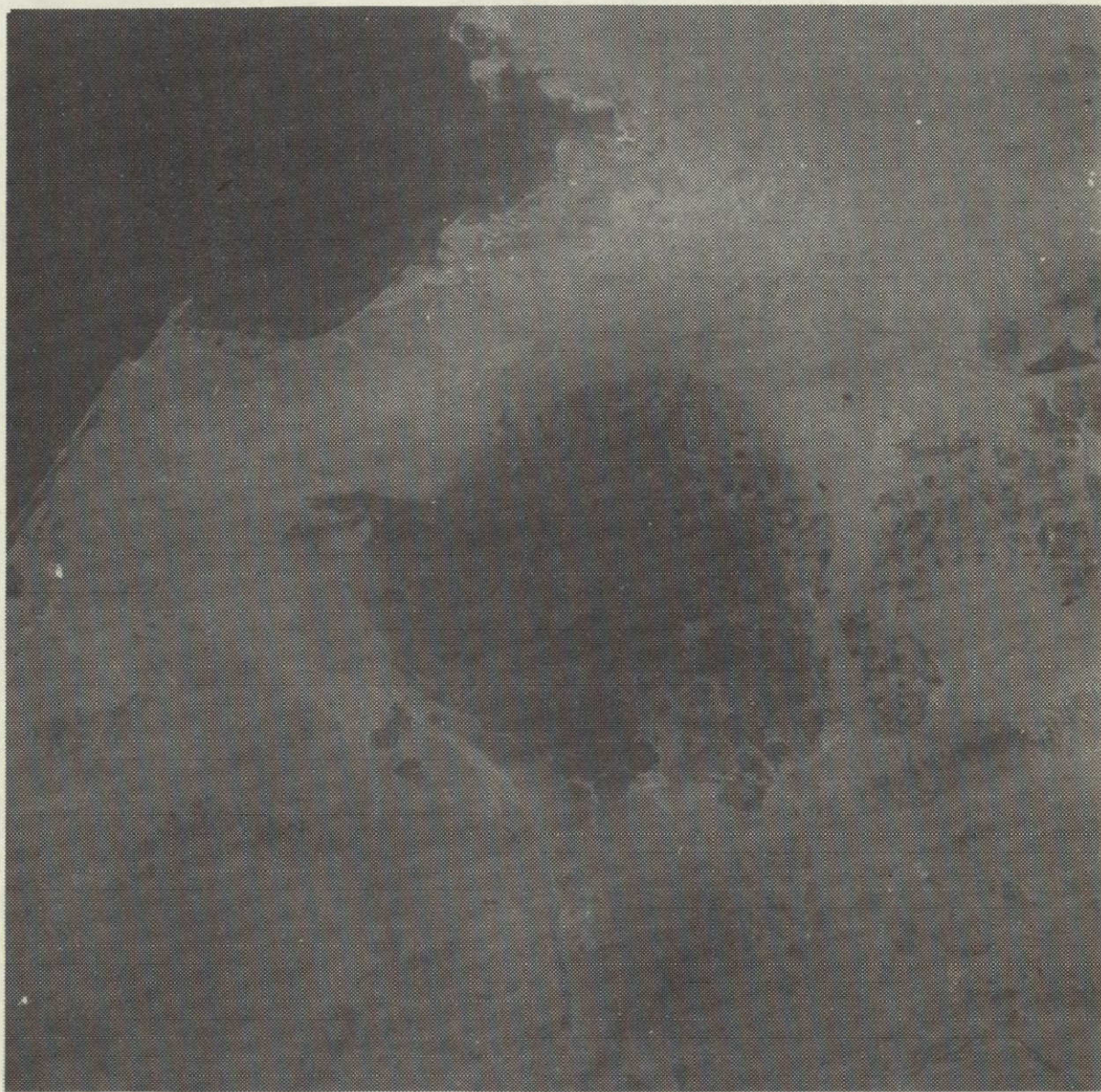
Figure 45.- The Sierra del Pinacate volcanic field.

Figure 46.- A portion of the Edwards Plateau and Staked
Plains interface in central Texas.

Figure 47.- A photograph of the Great Bahama Bank, Bahama Islands, taken from the Gemini IV spacecraft.
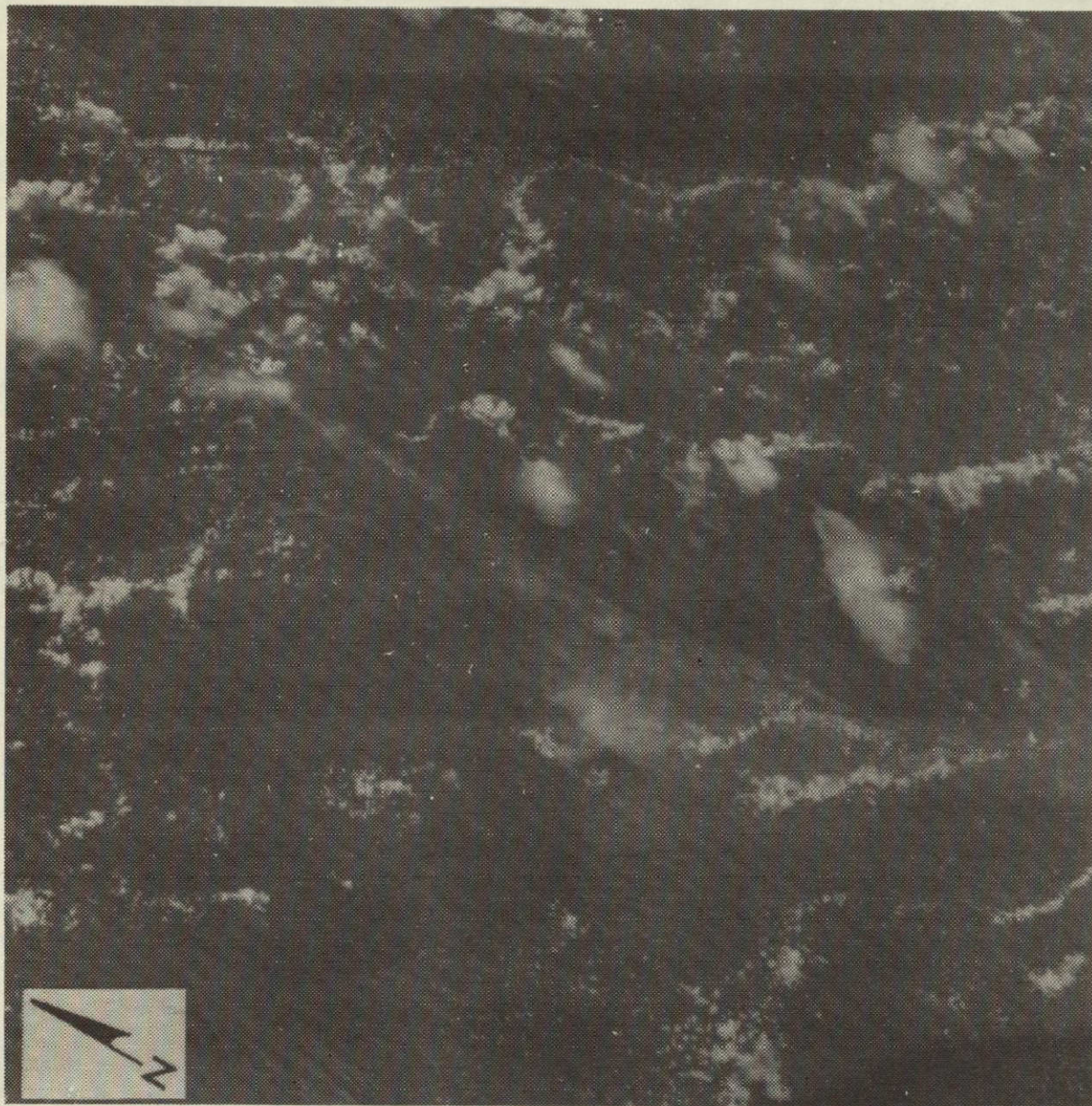
Figure 48.- An oblique view of the Great Bahama Bank, Bahama Islands, taken from the Gemini V spacecraft.
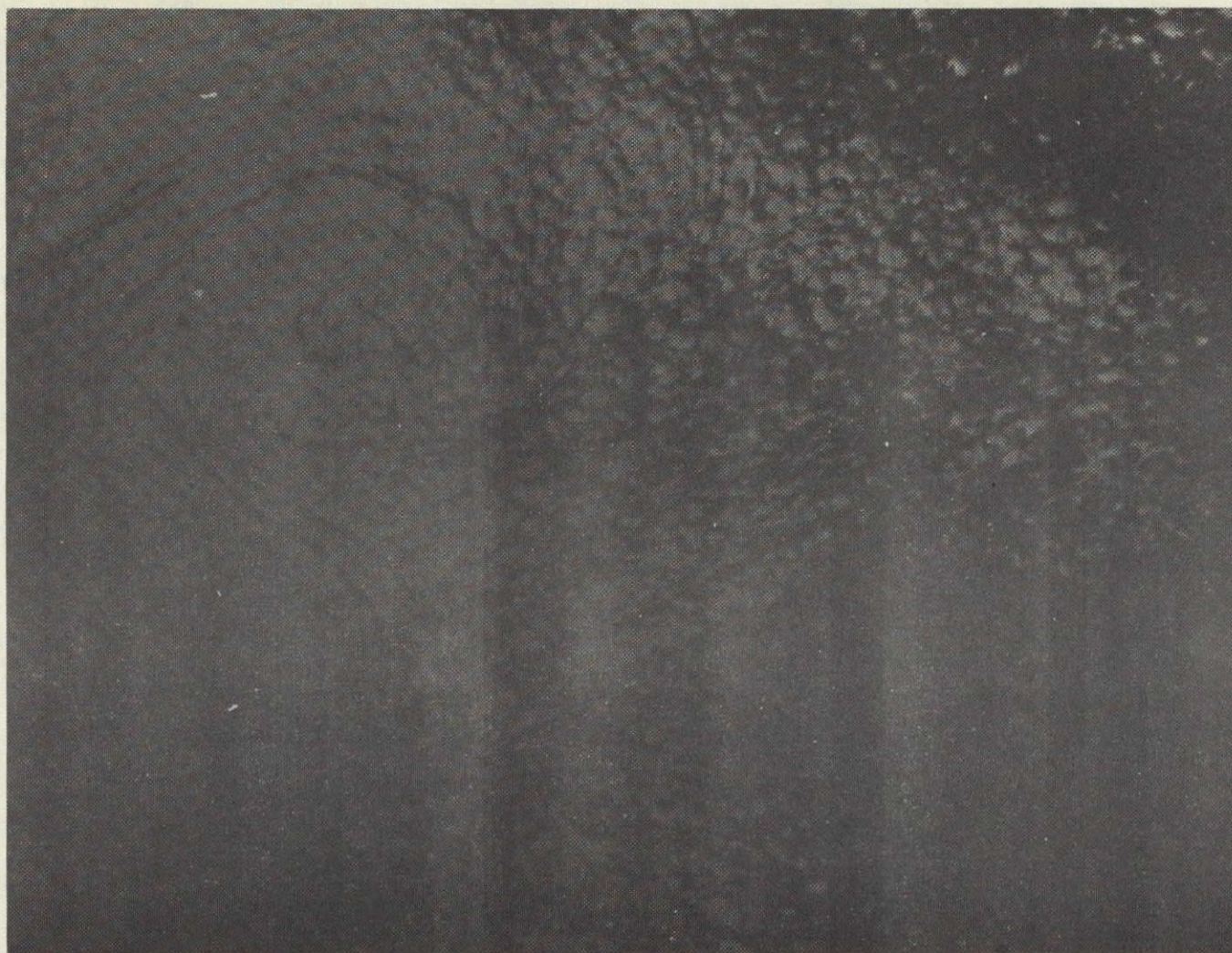
Figure 49.- A forming South Atlantic tropical storm, taken from the
Gemini V spacecraft.
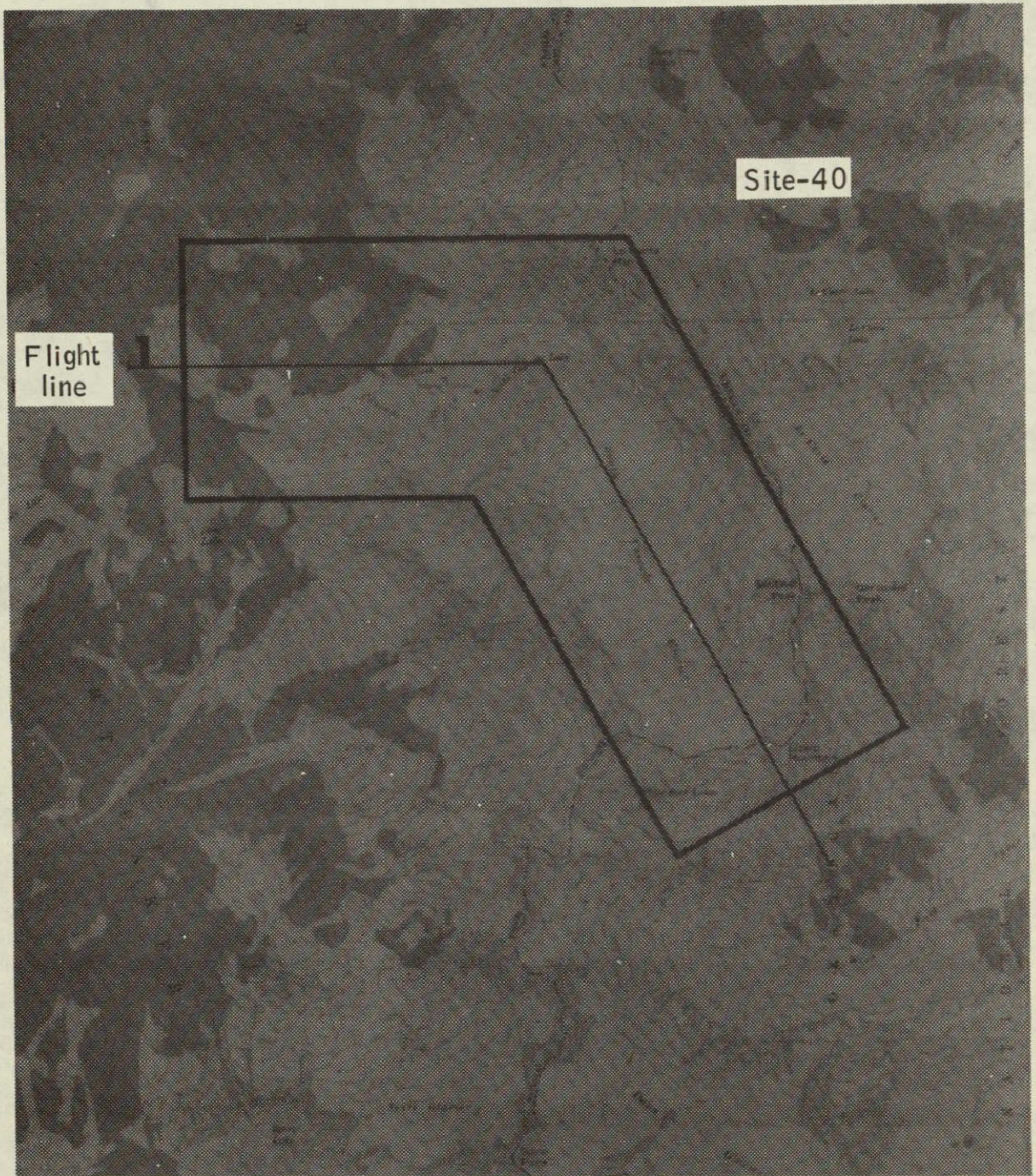
Figure 50.- A contour map of the South Cascade Glacier.
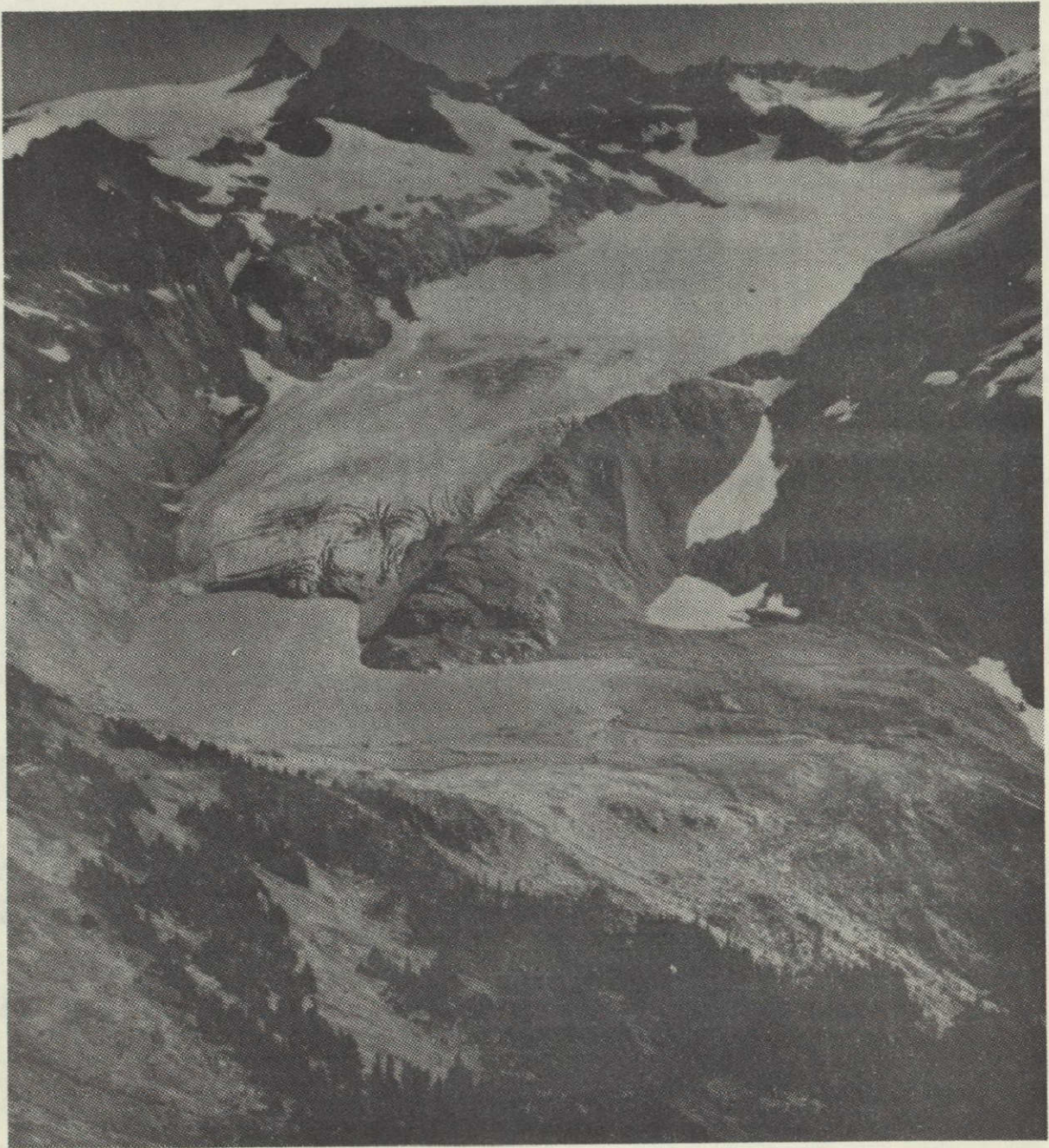
Figure 51.- An oblique aerial photograph of the South Cascade Glacier.

Figure 52.- A vertical photograph of the South Cascade Glacier,
taken by an RC-8 camera using color film.
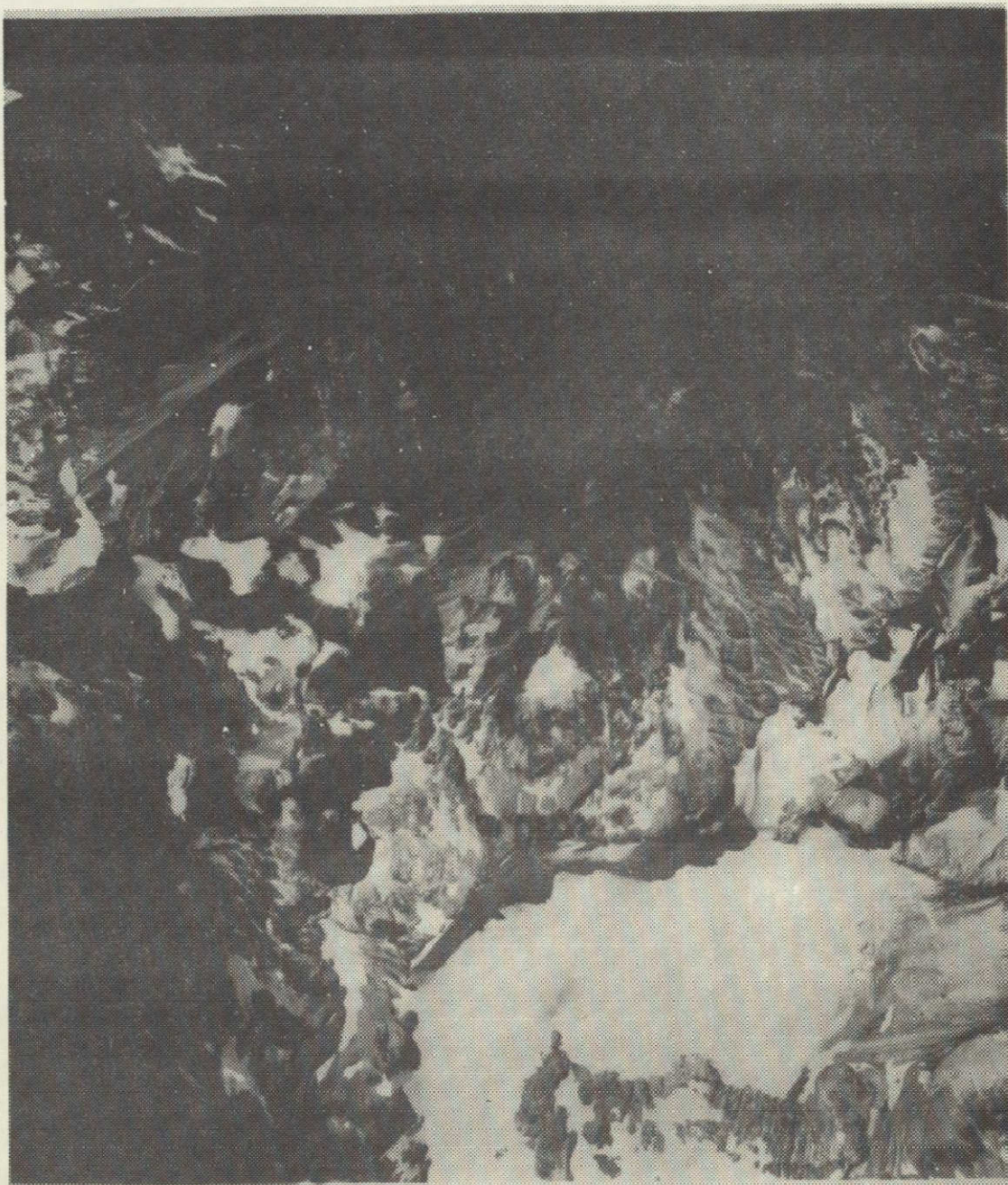
Figure 53.- A vertical photograph of the South Cascade Glacier,
taken by an RC-8 using infrared color film.
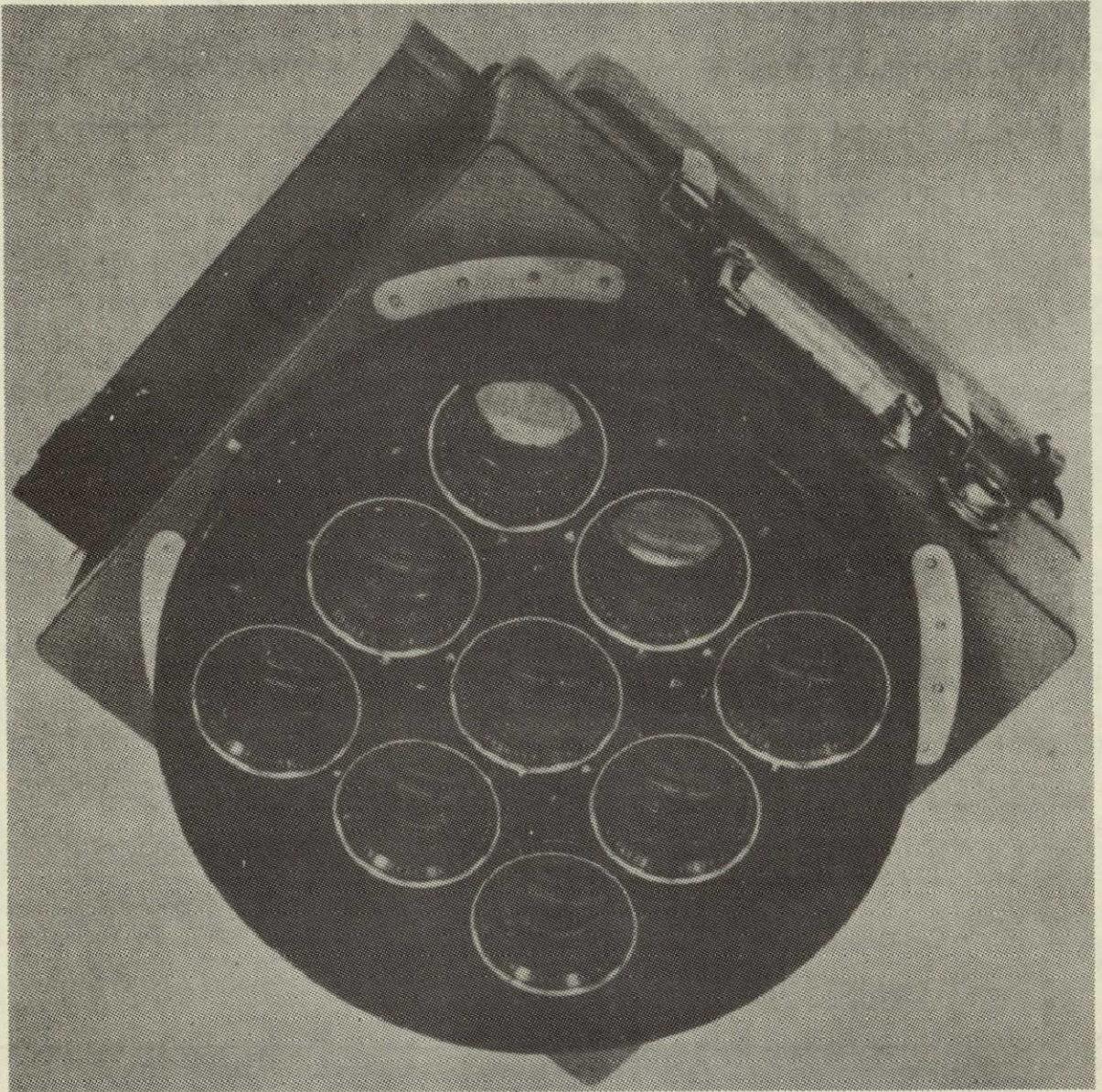
Figure 54.- A nine-lens multispectral camera system.

96

Flight, IMC and
film wind
direction

Film path 1

Film path 2

Film path 3
(infrared)

Frame
counter
numerals

1|2|3

1|2|3

1|2|3

1

3

7

36 + 38A

65A + 58

87B

2

5

8

3 + 47

72B

87

Cone
pin

4

6

9

21 + 57

21 + 34

87C

Shutter
direction
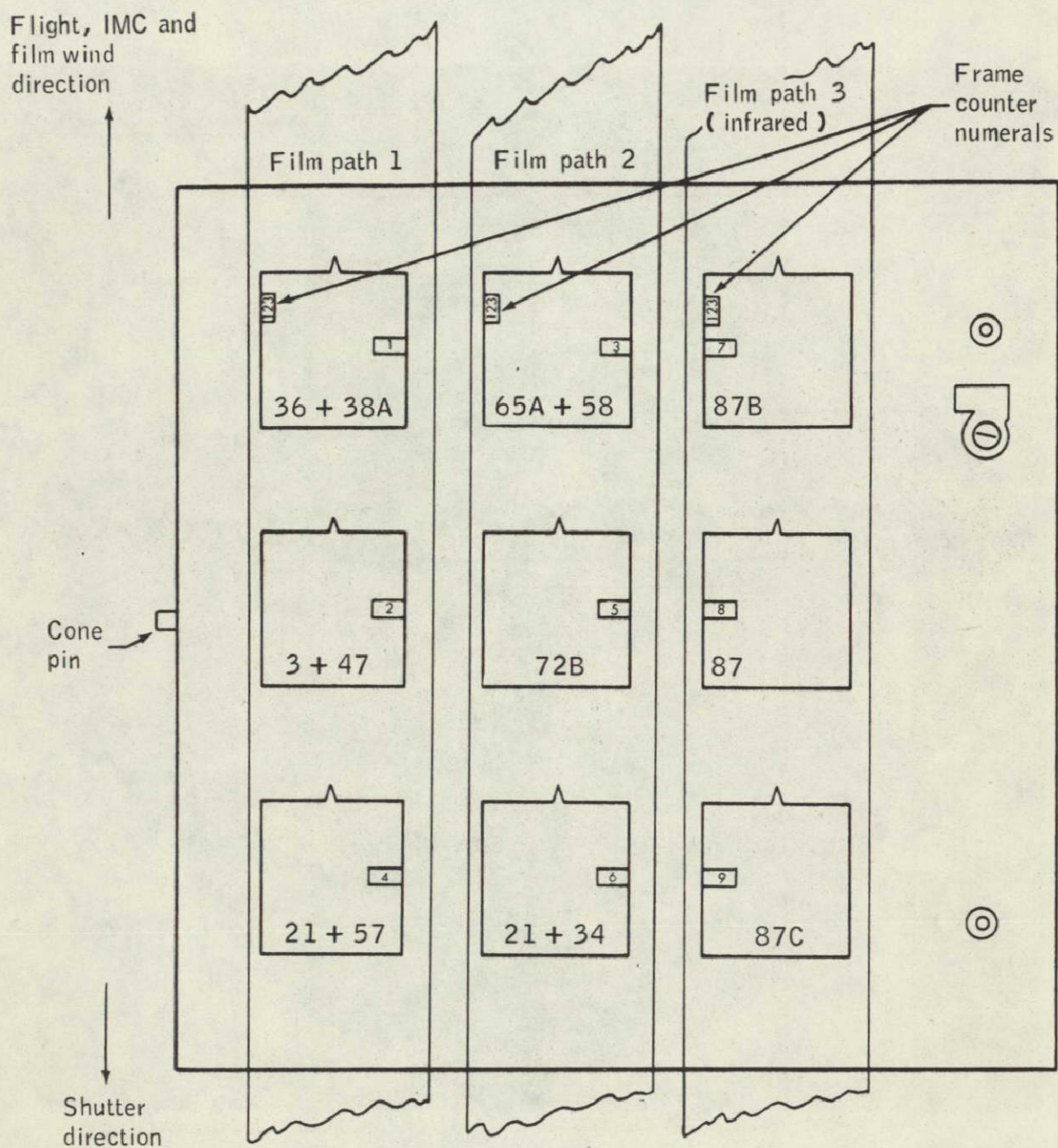
Figure 55.- Schematic view of the format area of the nine-lens camera.
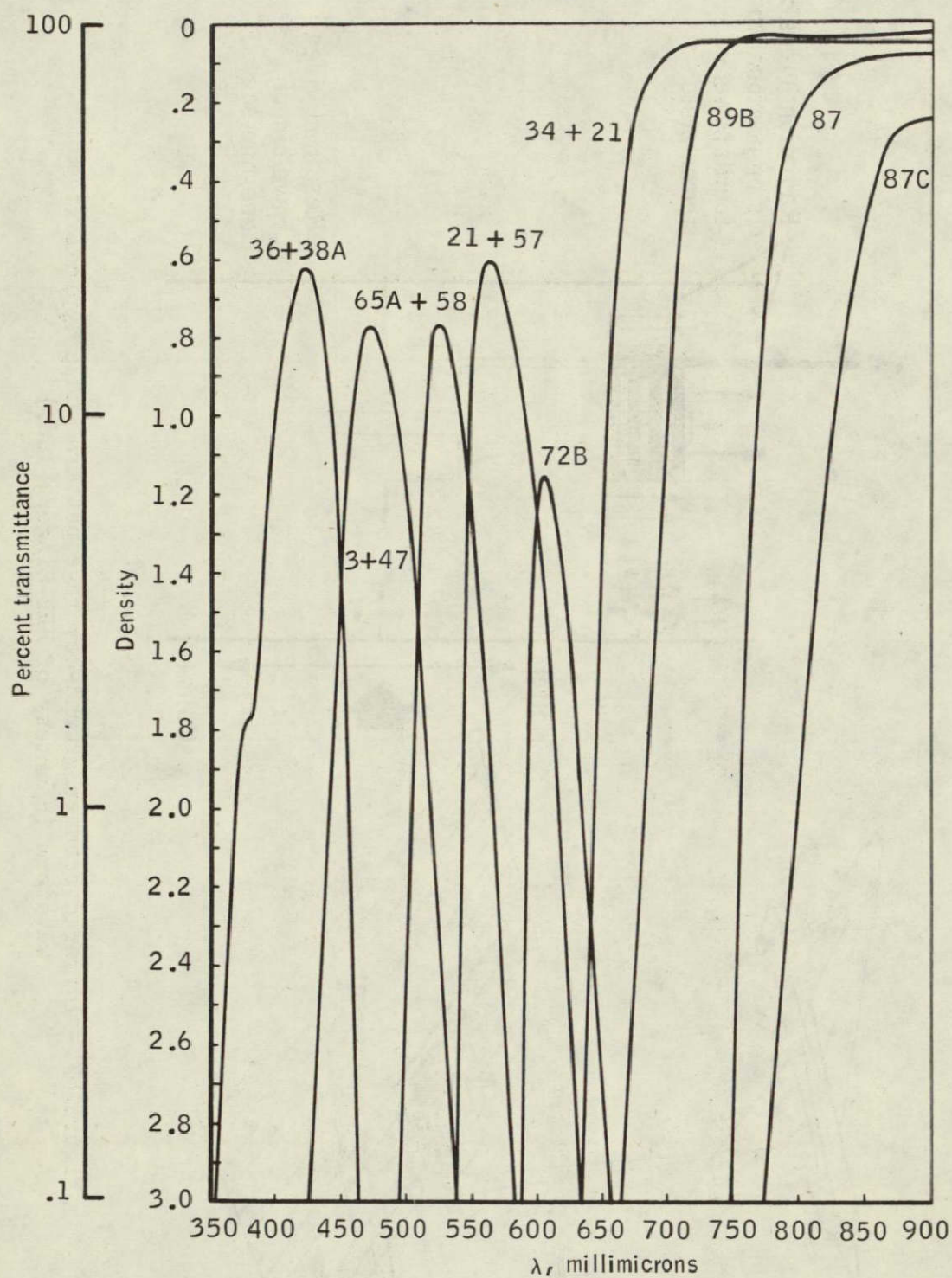
Figure 56.- Nominal transmission curves of multiband filters.

Radiation intensity
is proportional to
fourth power of
temperature

Hotter

Colder

Resultant video
waveform of
one line scan
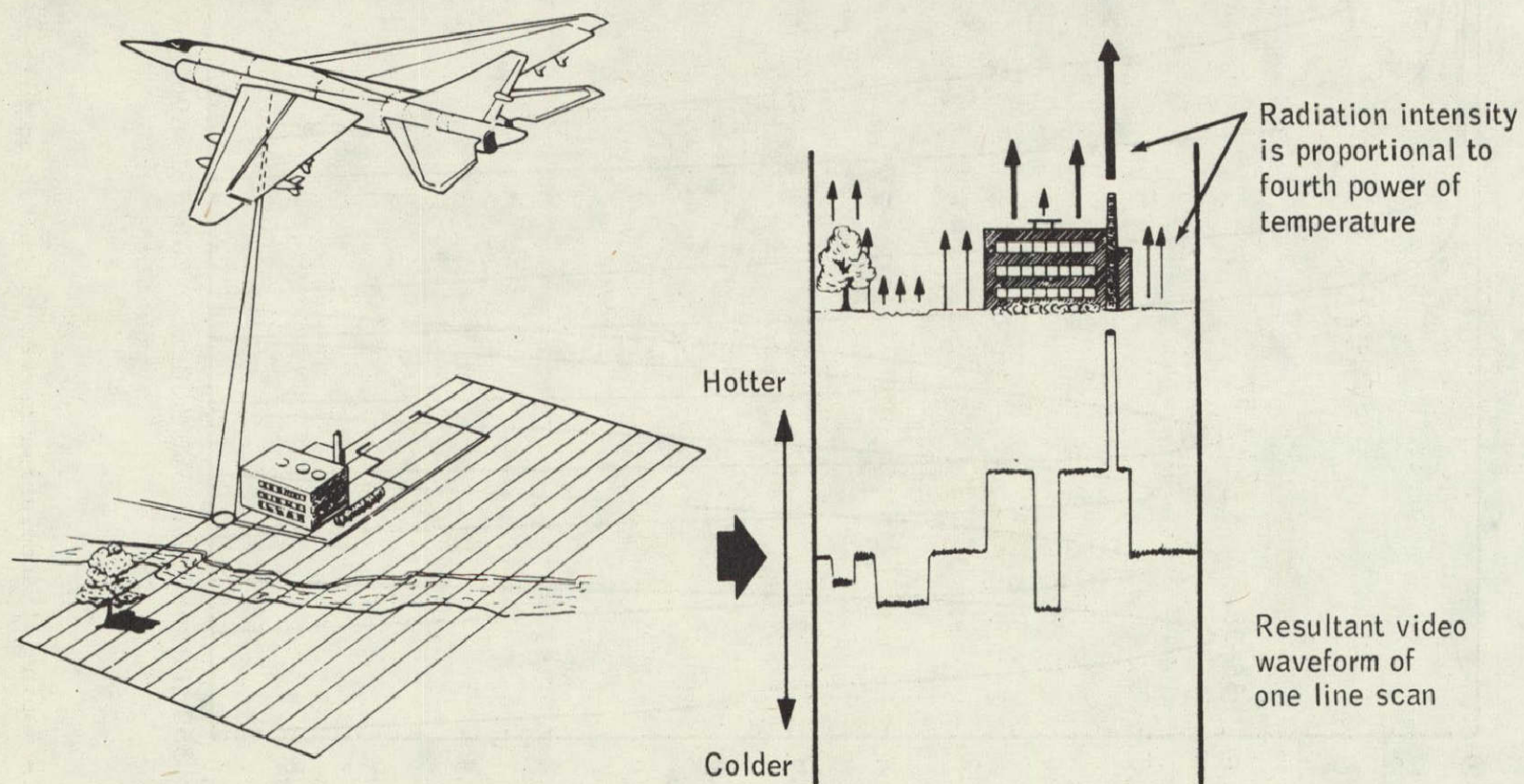
Figure 57.- Infrared scanner ground-coverage pattern and a typical video
waveform (courtesy of HRB-Singer, Inc.).
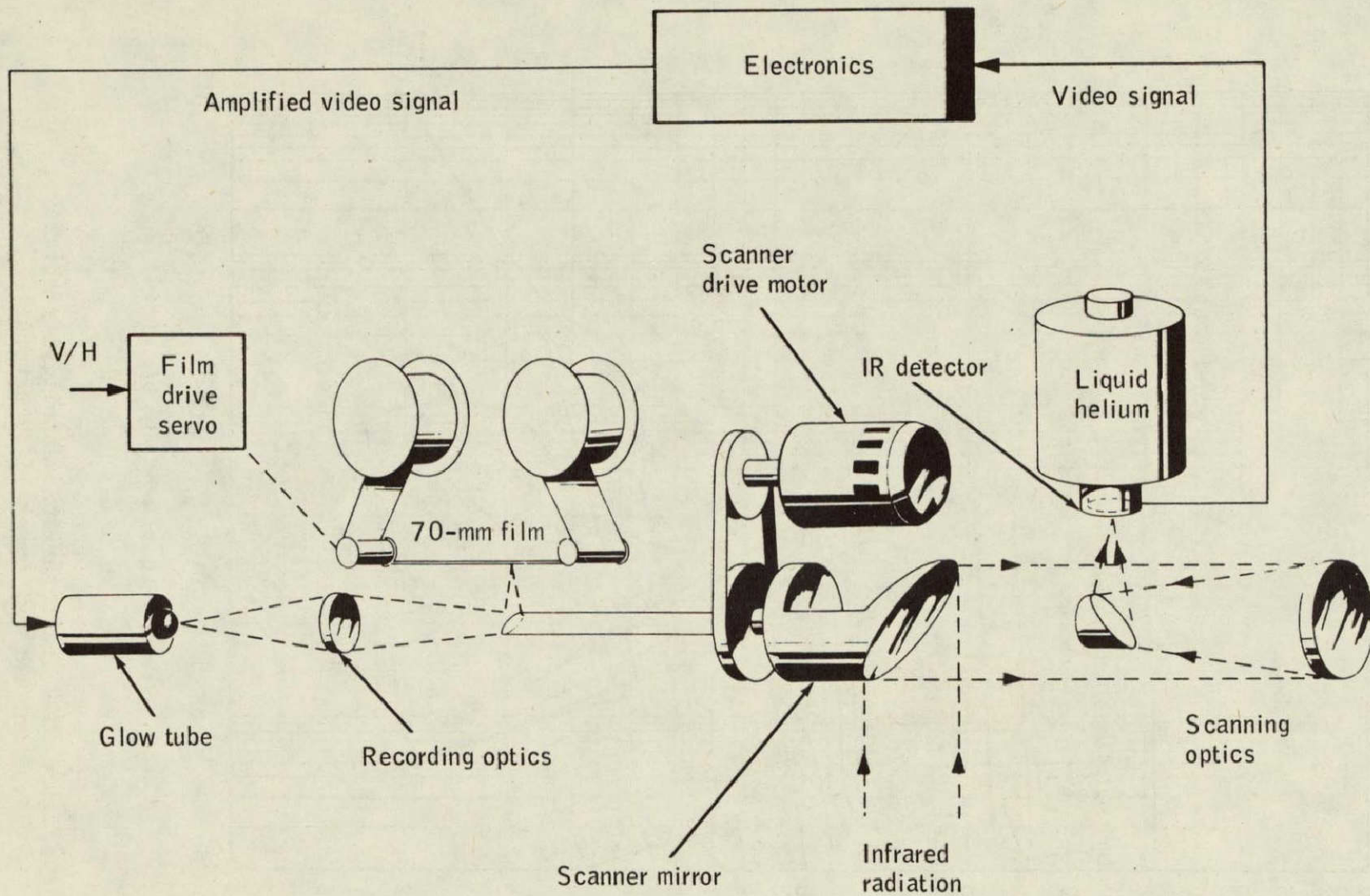
Figure 58.- Schematic representation of an infrared system employing reflective optics (courtesy of HRB-Singer, Inc.).
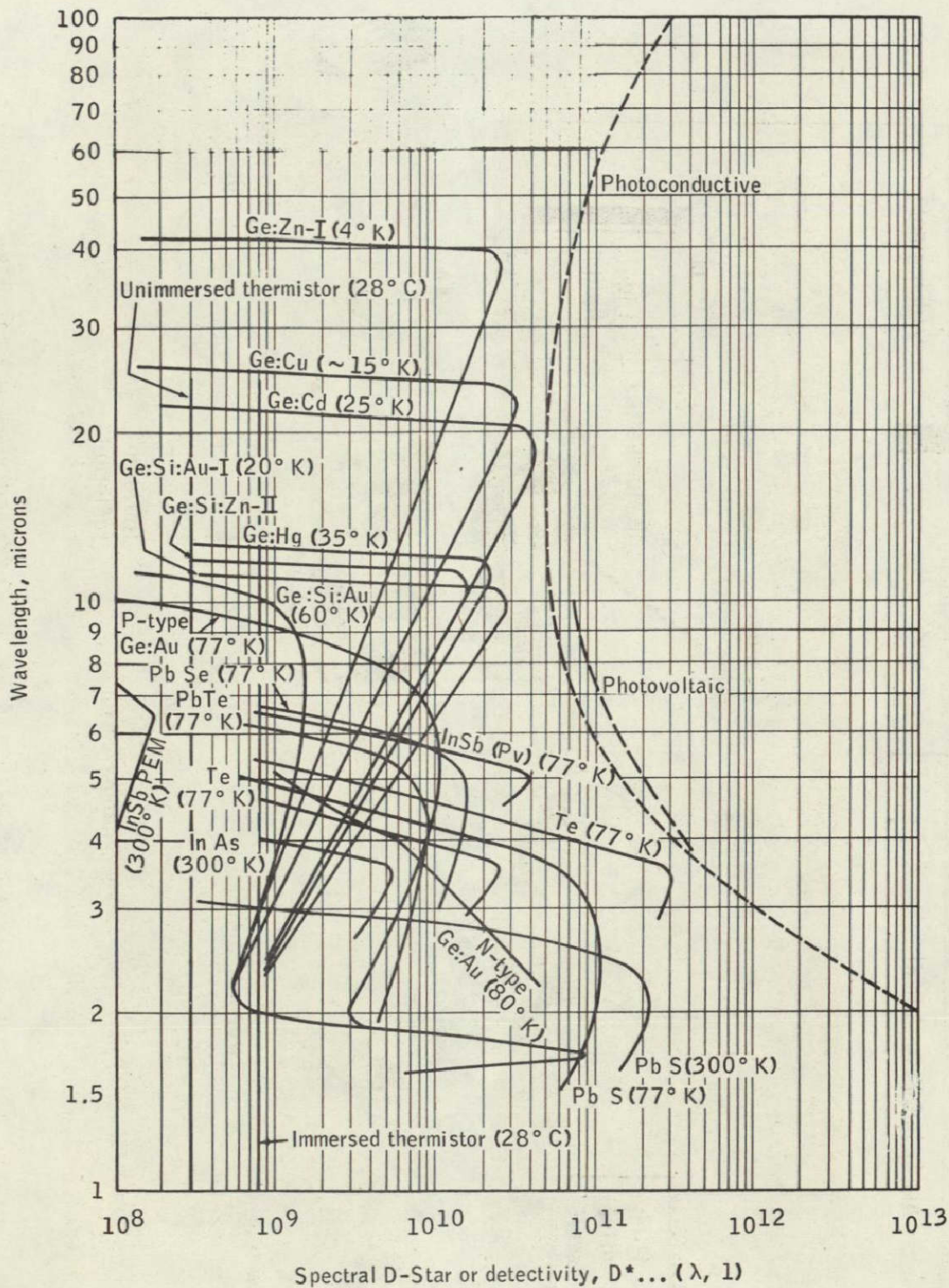
Figure 59.- Characteristic sensitivity curves
for several infrared detectors.
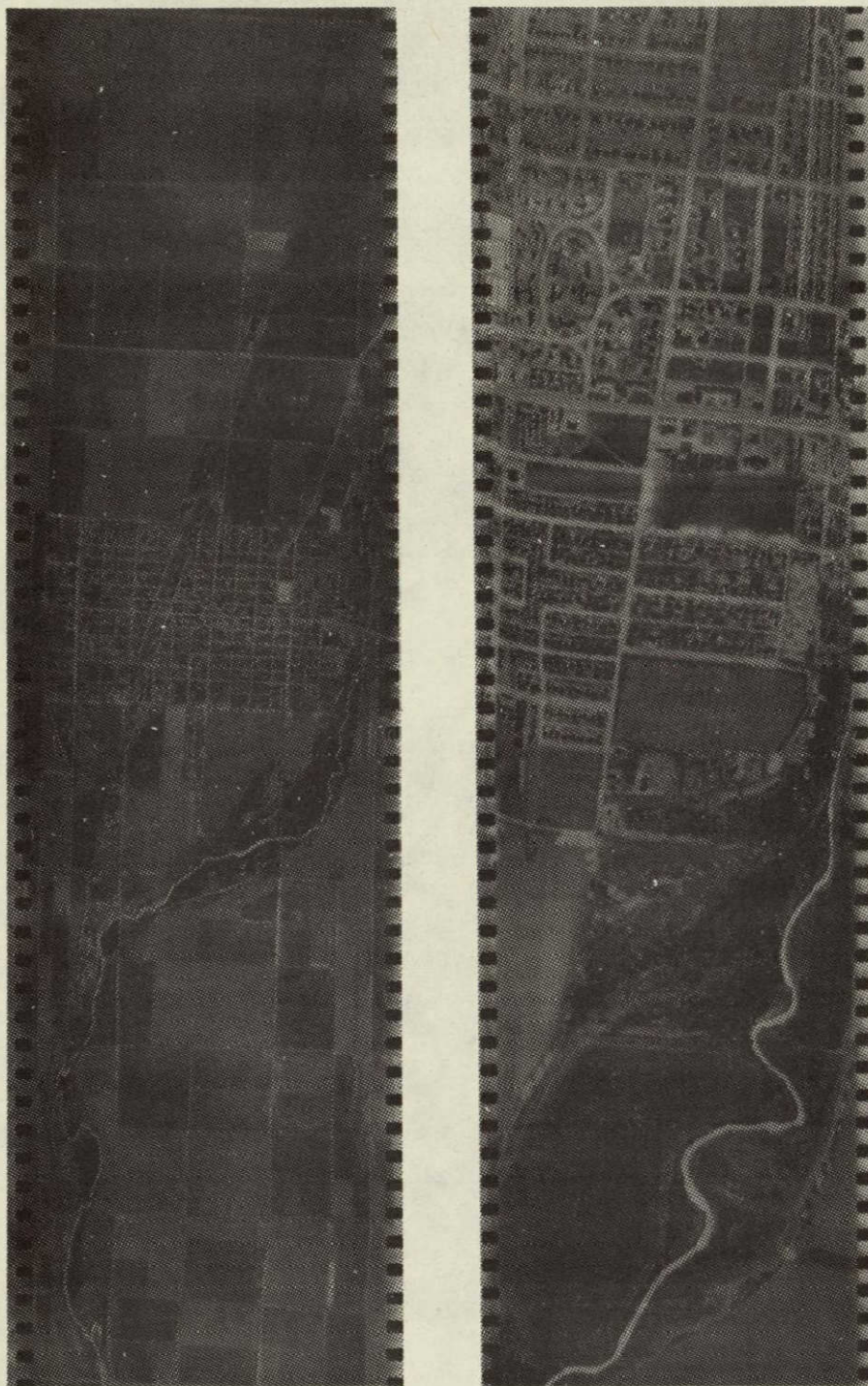
Figure 60.- Seventy-millimeter infrared
imagery (courtesy of HRB-Singer, Inc.).
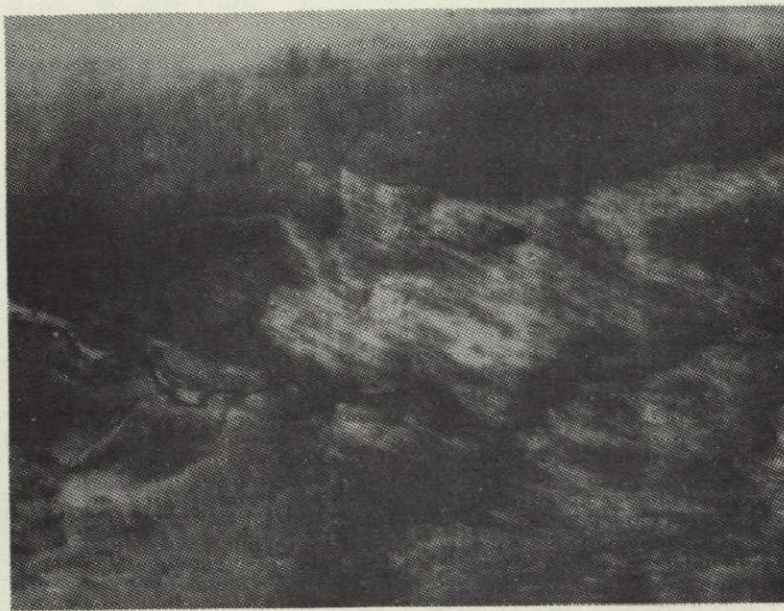
(a) Terrain near Quincy, California.

(b) Terrain near Walley's Spring, Nevada.

Figure 61.- Examples of infrared imagery
   (courtesy of Texas Instruments Inc.,
   SSD).
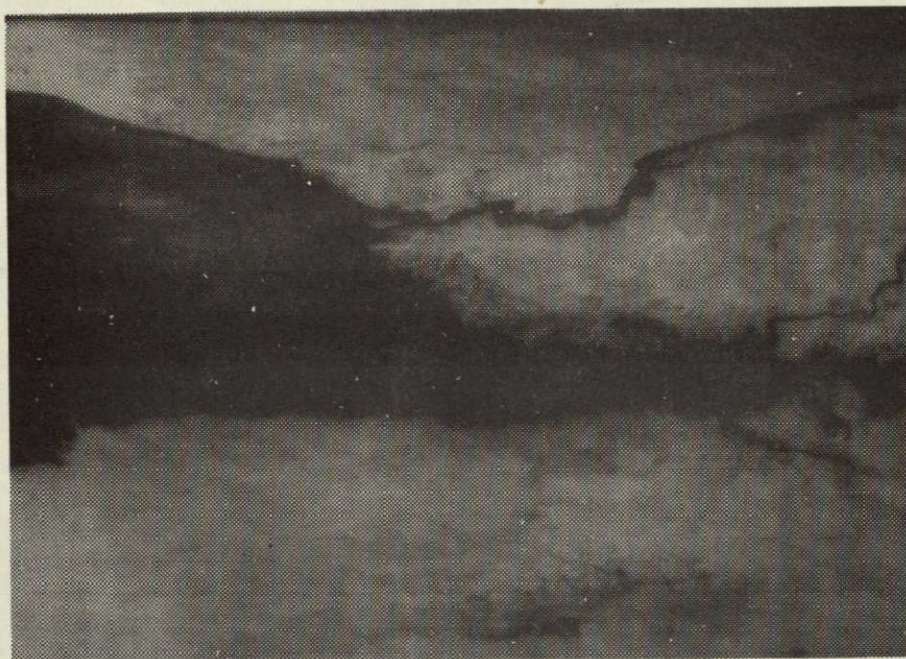
(a) Terrain near Walley's Springs, Nevada.
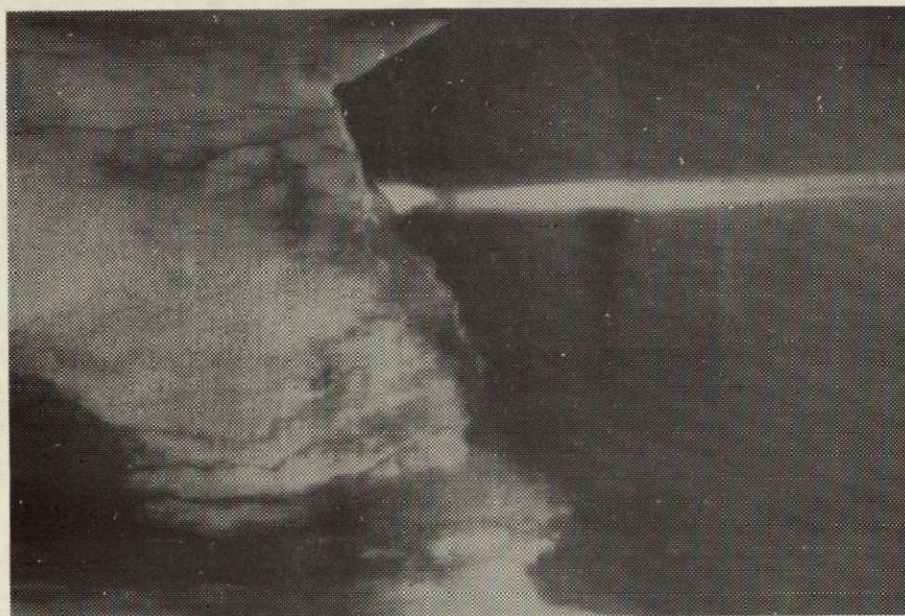
(b) Terrain near Salton Sea, California.

Figure 62.- Examples of infrared imagery (courtesy of Texas
Instruments Inc., SSD).
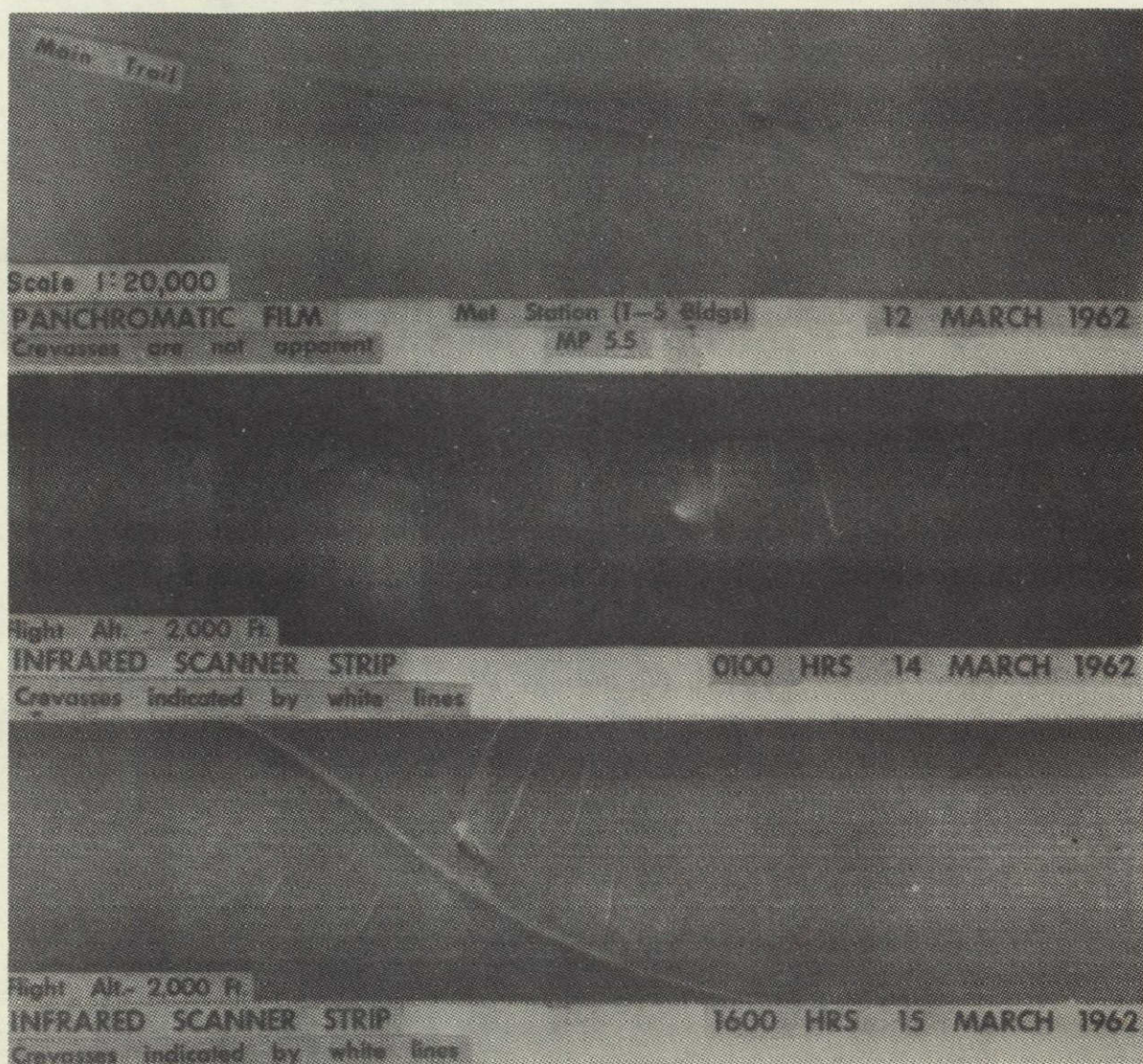
Figure 63.- Comparison of conventional photographic data with infrared imagery acquired under night and daytime conditions.
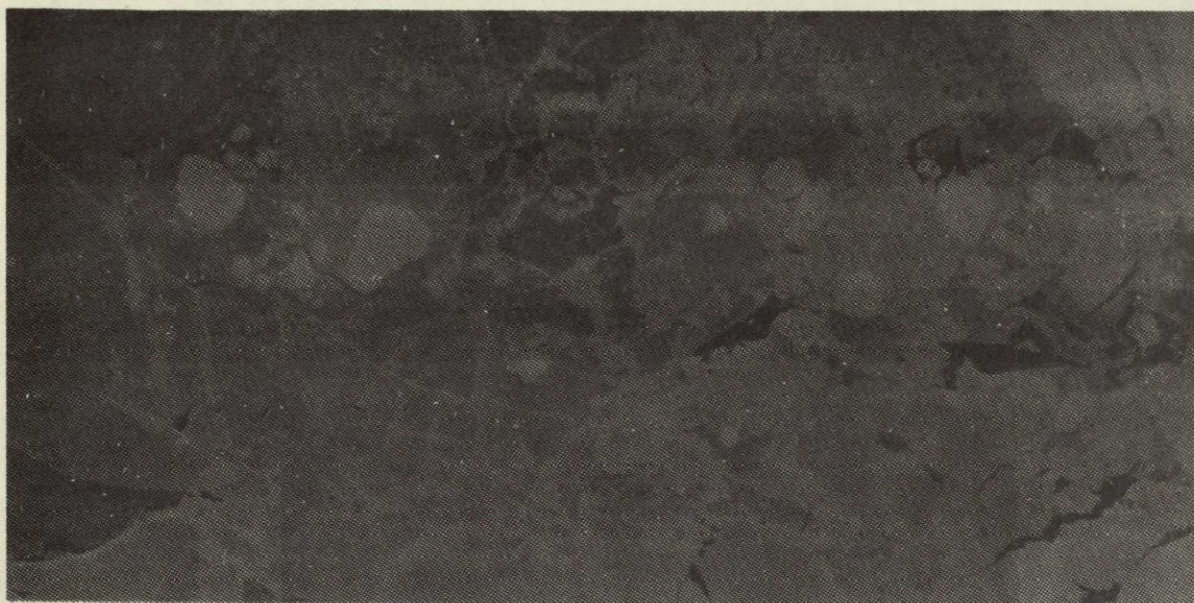
a) Panchromatic aerial photograph

b) Infrared imagery

Figure 64.- Conventional aerial photography and an infrared thermal image of sea ice obtained simultaneously.

(a) Infrared film.
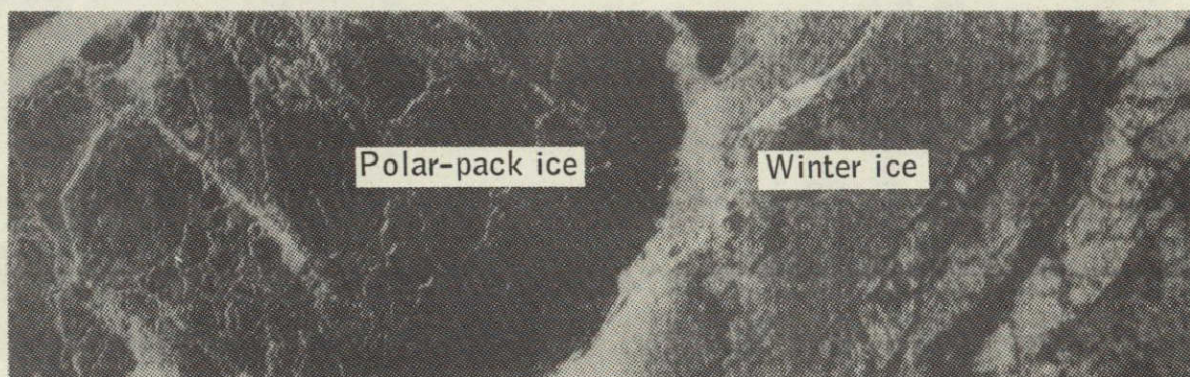
(b) Infrared scanner.

Figure 65.- Infrared images of ice obtained under
Arctic-night conditions.
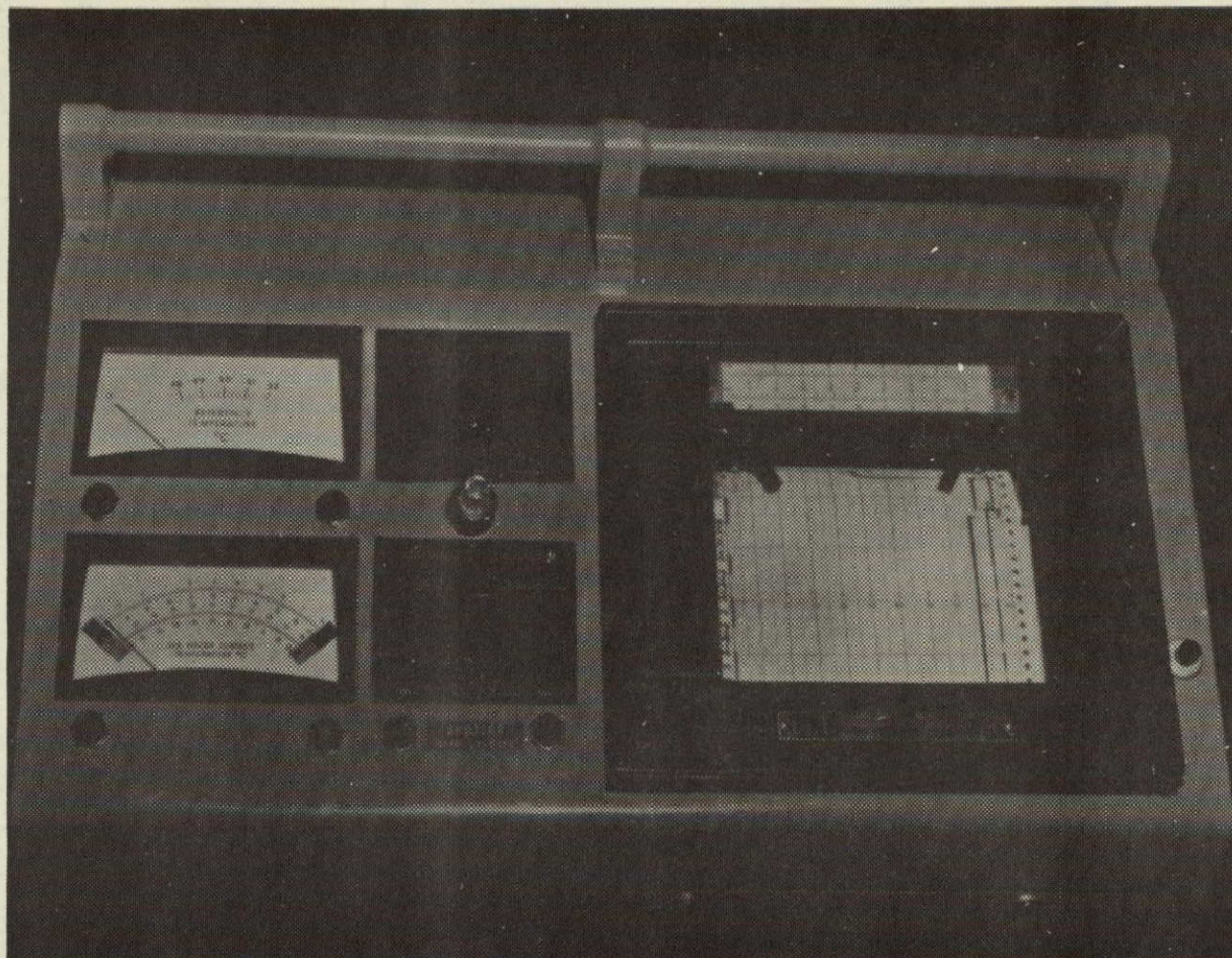
Figure 66.- Airborne Radiation Thermometer control unit installed in the
Antisubmarine Warfare Environmental Prediction Service aircraft.
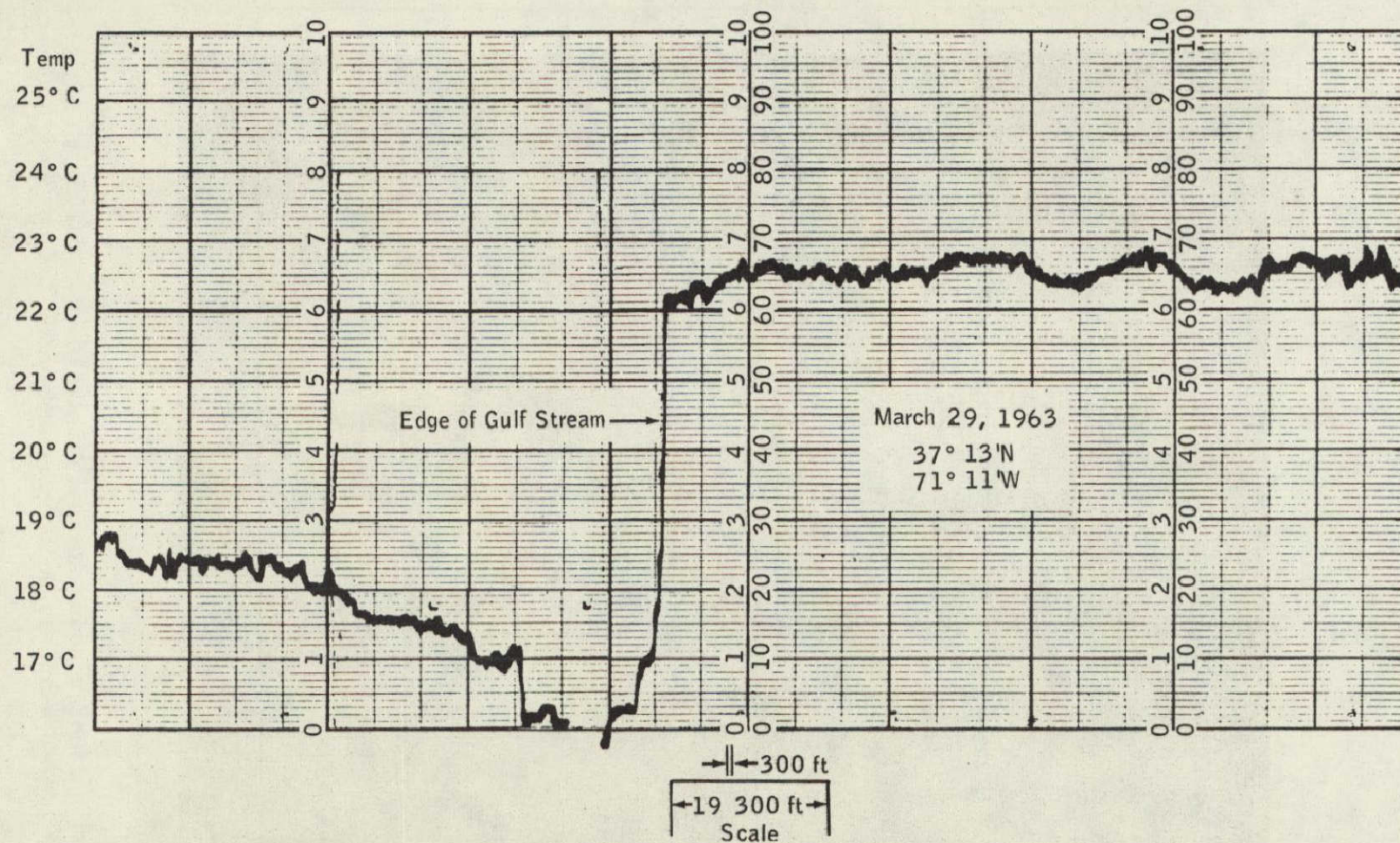
Figure 67.- Data sample obtained over the Gulf Stream in March 1963.

Figure 68.- The Naval Oceanographic Office C-121 aircraft.
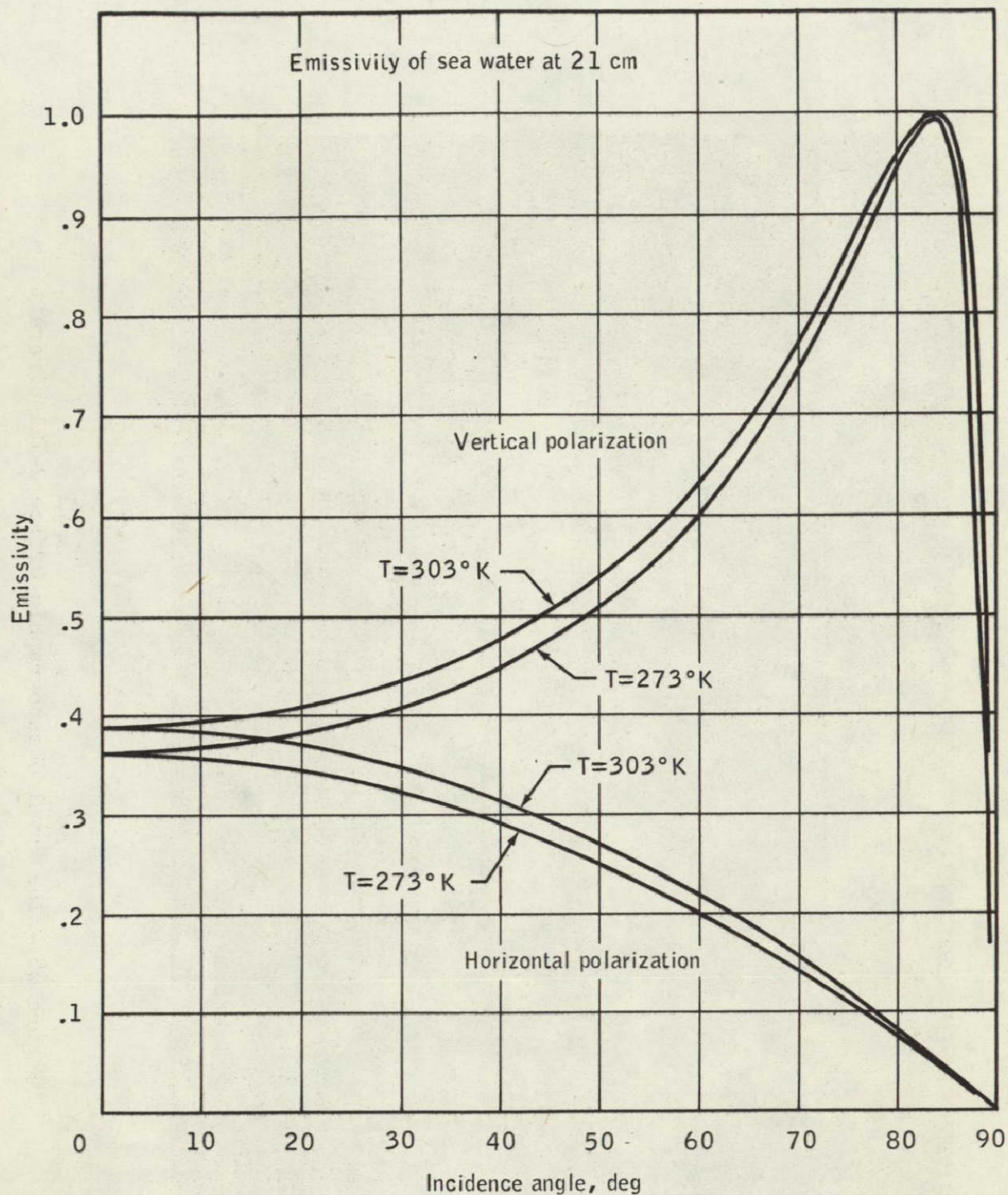
Figure 69.- Curve showing emissivity versus antenna looking angle
as related to radiometric measurements of ocean water.
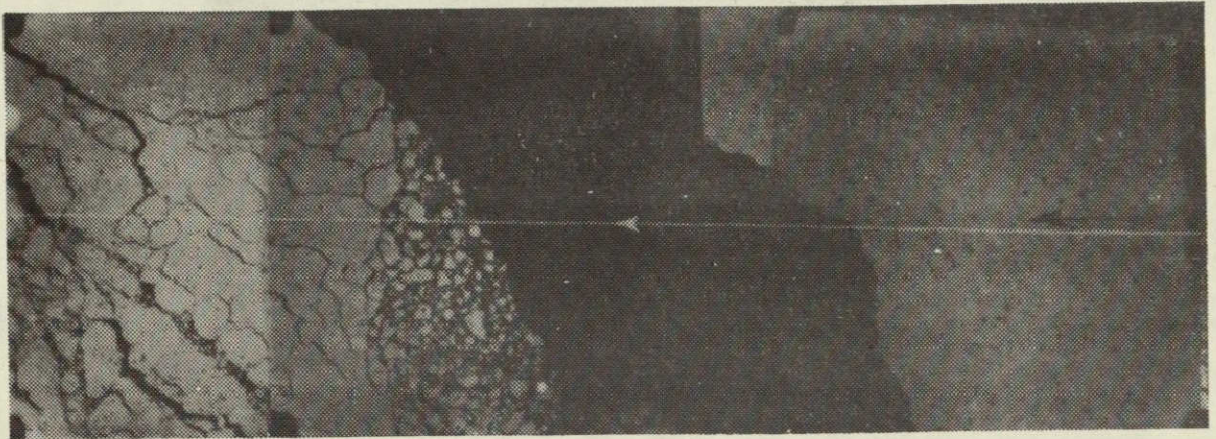
(a) Airphoto of ice-water boundary showing flight direction and radiometer track.

Pt. no. 20
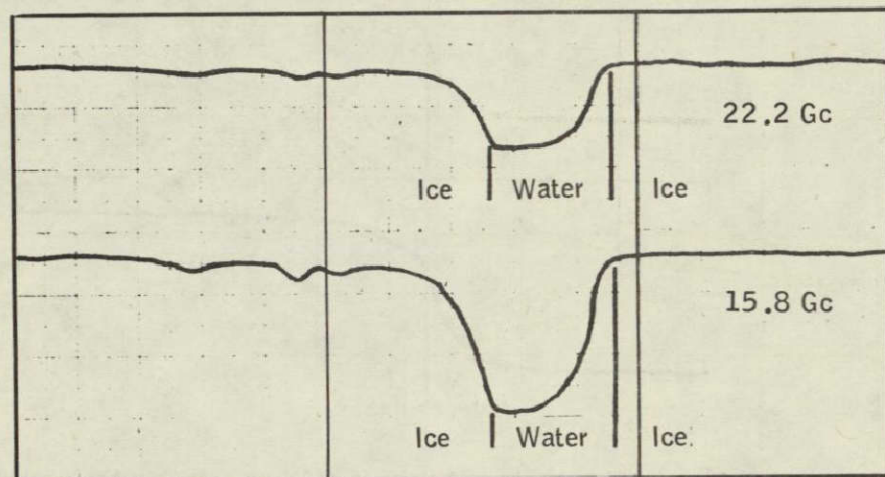
(b) Strip chart record of passive microwave radiometer signals.
(2 mm = 1 mm on original)

Recording parameters

Altitude . . . . 2000 ft
Ground speed . . . 165 knots (278 ft/sec)
Drift angle . . . . 1° right
Radiometer incidence angle . . . . . . 45°
Vertical polarization plane . . . . H

Original chart speed . . . . 1 mm/sec
Original 22.2 Gc trace . . 7.3° K/mm defl.
Original 15.8 Gc trace . . 7.7° K/mm defl.
Note:
1 mm on chart equals 3.31 mm on photograph

Figure 70.- Data obtained off the coast of Labrador
from the NASA-MSC CV-240A aircraft.

112
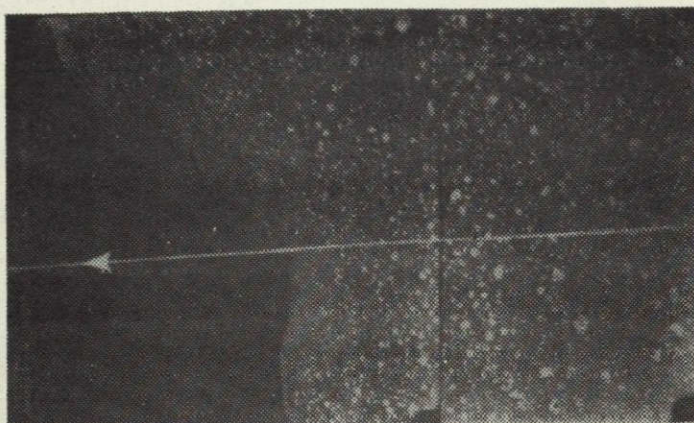
(a) Airphoto of ice-water boundary showing flight direction and radiometer track.

Pt. no. 28
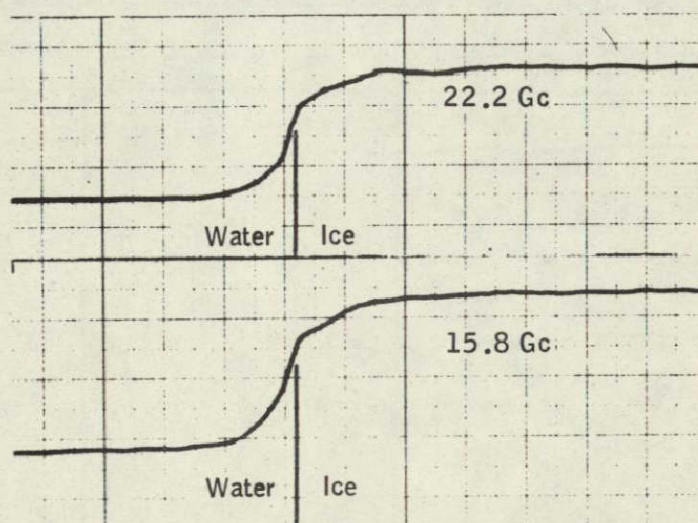
22.2 Gc

Water | Ice

15.8 Gc

Water | Ice

(b) Strip chart record of passive microwave radiometer signals.
(2 mm = 1 mm on original)

Recording parameters

Altitude . . . . 2000 ft
Ground speed . . . 150 knots (253 ft/sec)
Drift angle . . . . 5° left
Radiometer incidence angle . . . . 10°
Vertical polarization plane . . . . E

Original chart speed . . . . 1 mm/sec
Original 22.2 Gc trace . . 7.2° K/mm defl.
Original 15.8 Gc trace . . 7.4° K/mm defl.
Note:
1 mm on chart equals 3.01 mm on photograph

Figure 71.- Data obtained off the coast of Labrador
from the NASA-MSC CV-240A aircraft.
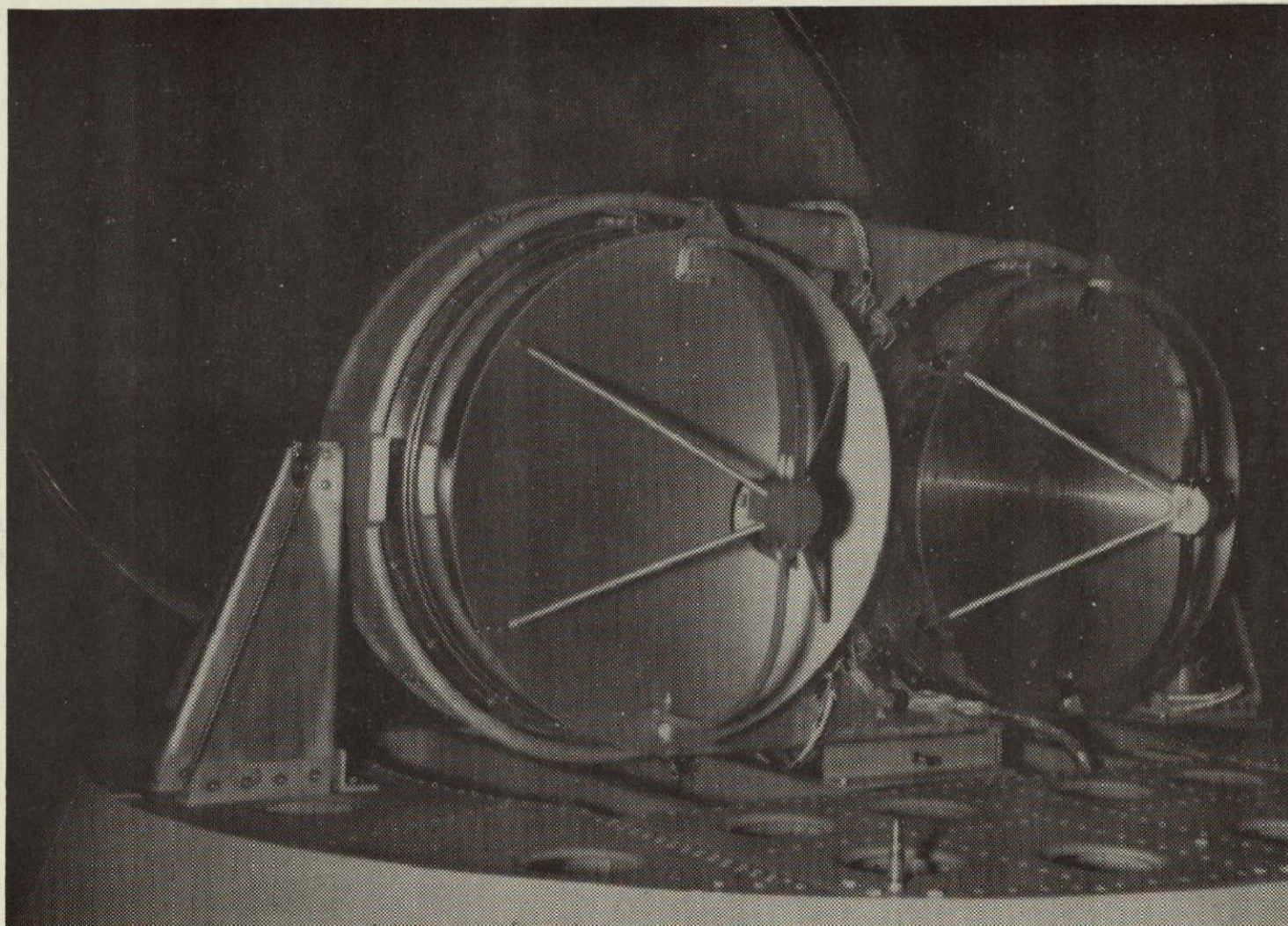
Figure 72.- Microwave radiometer systems installed in the NASA-MSC CV-204A aircraft.

Provides

- $\frac{V}{h}$ and drift data for navigation

- Maps for checkpointing and reconnaissance
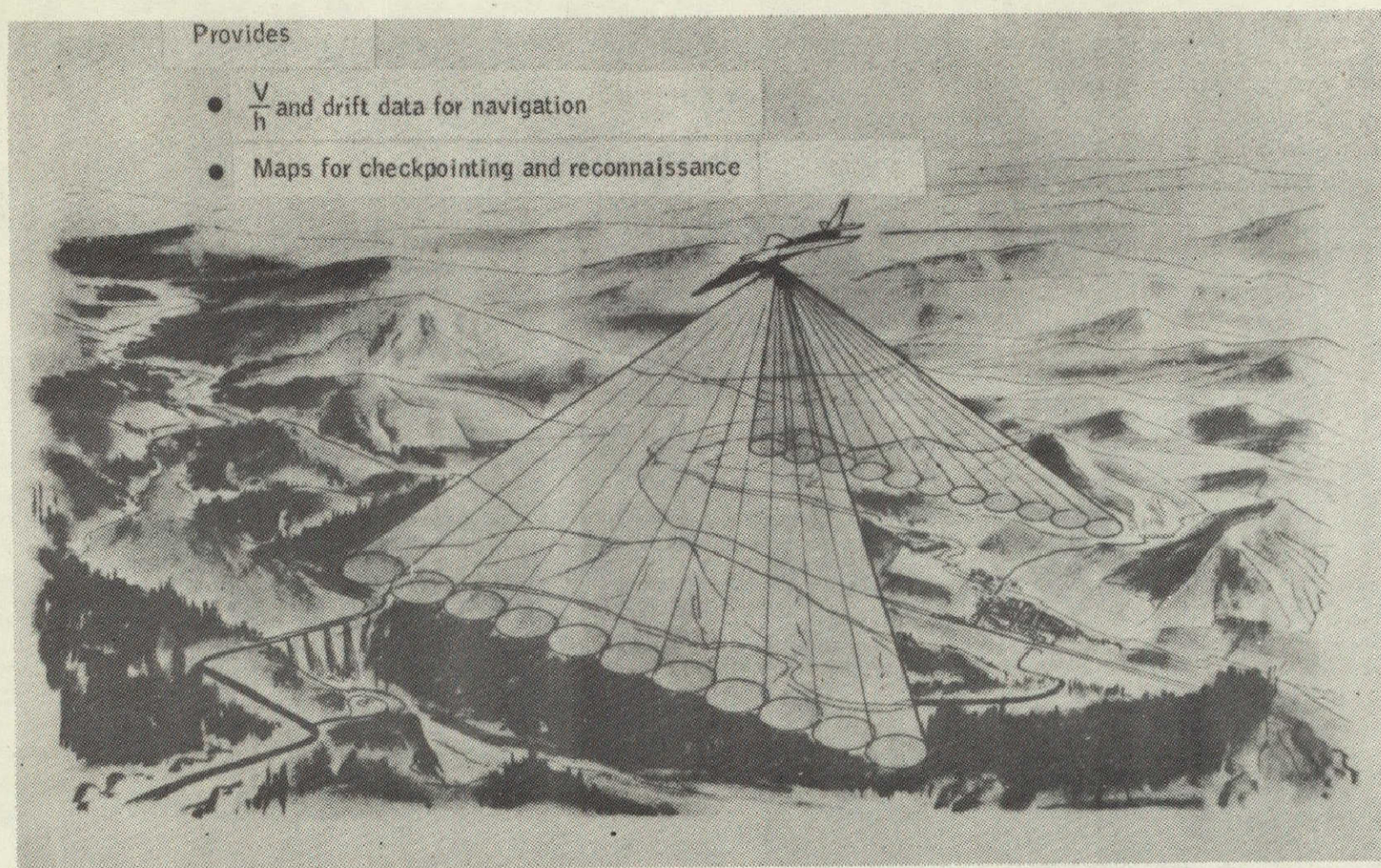
Figure 73.- Radiometric mapping system.
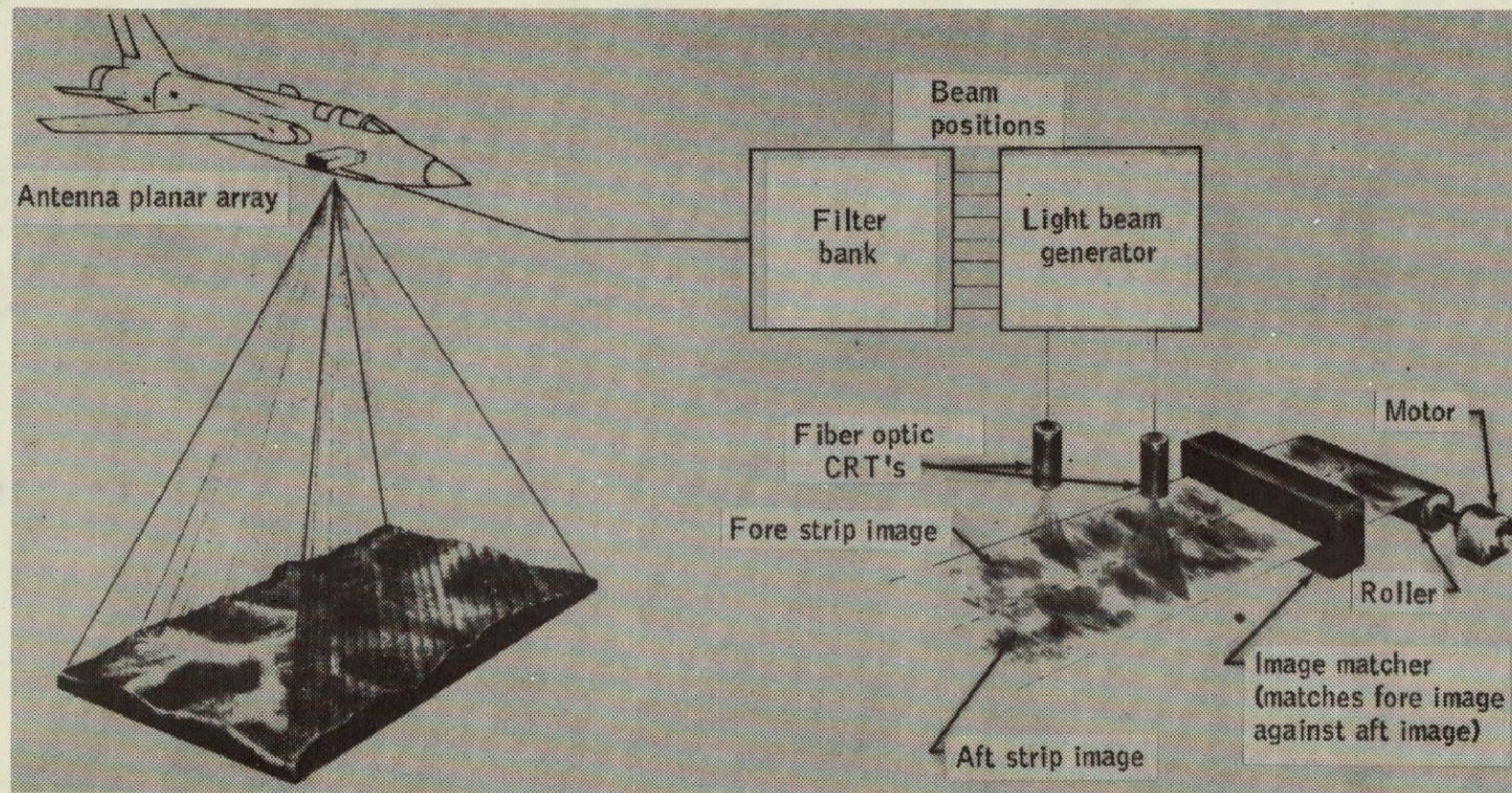
Figure 74.- Imaging microwave radiometer.
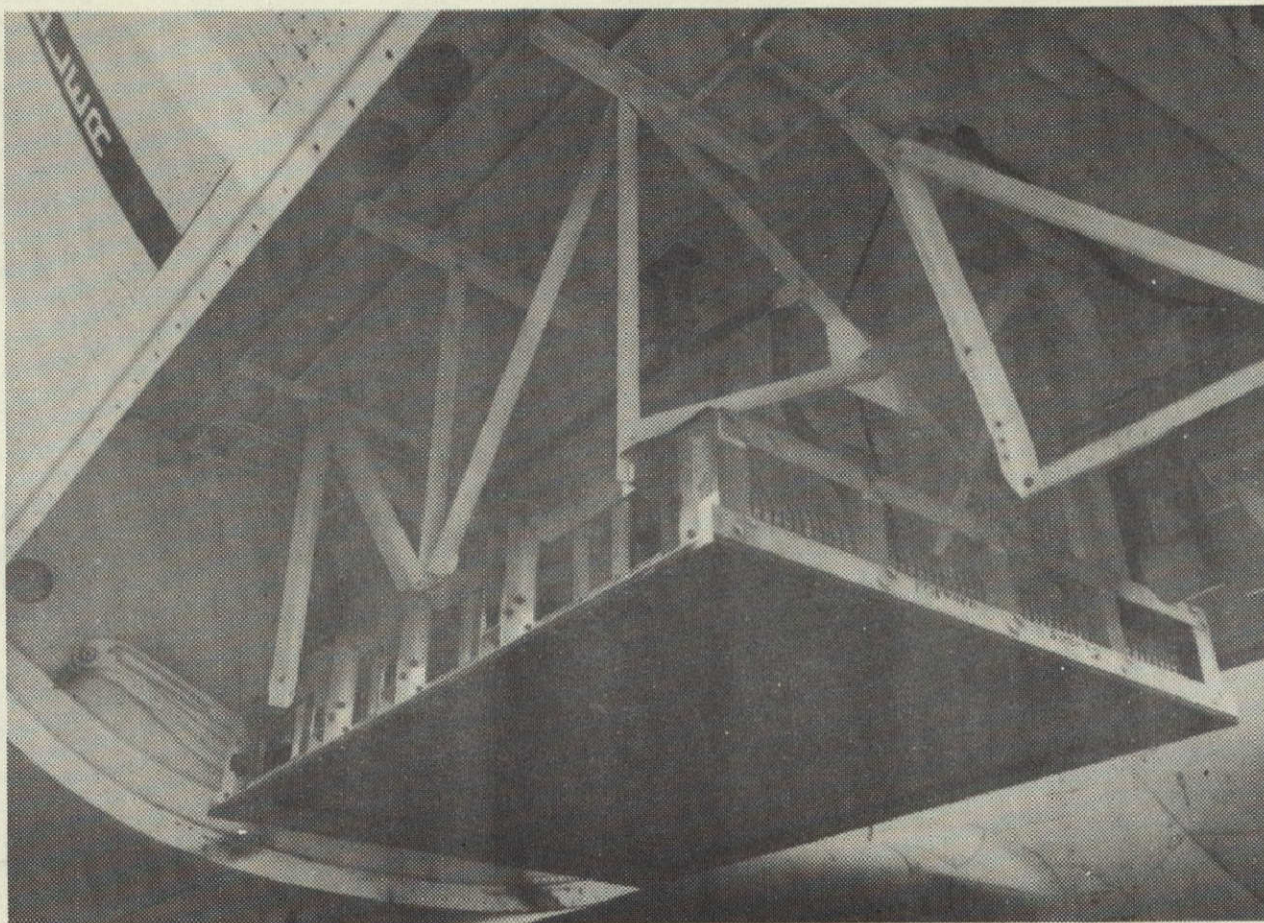
Figure 75.- Imaging microwave radiometer antenna installed
in the bomb bay area of a NASA P-3A aircraft.
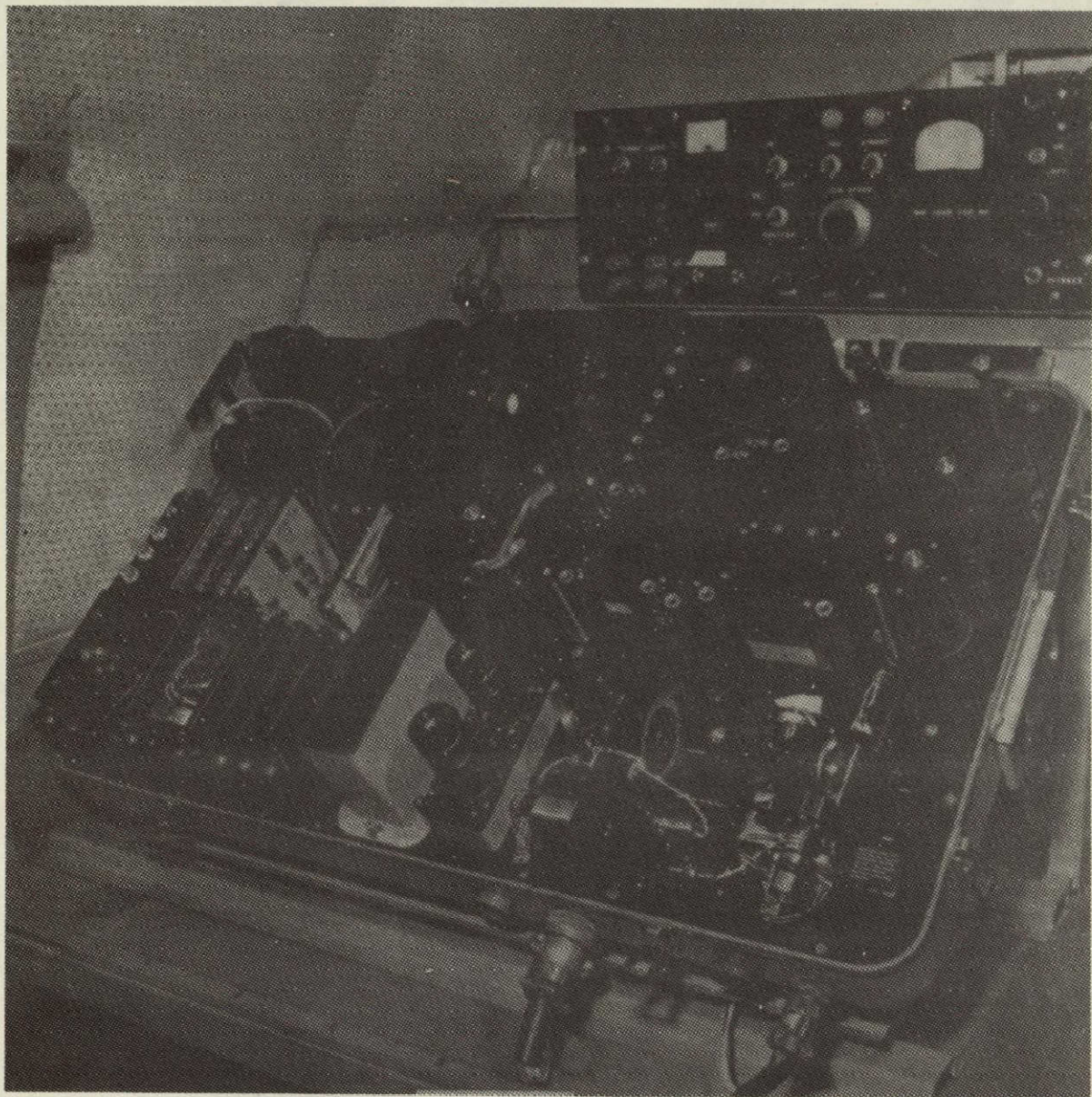
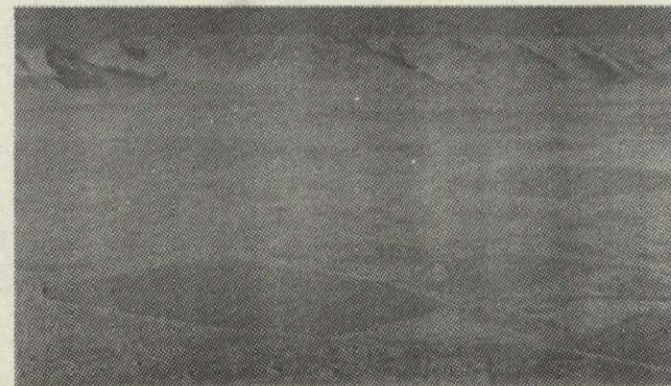Figure 76.- The cathode-ray tube/map-matcher unit
and systems control panel.
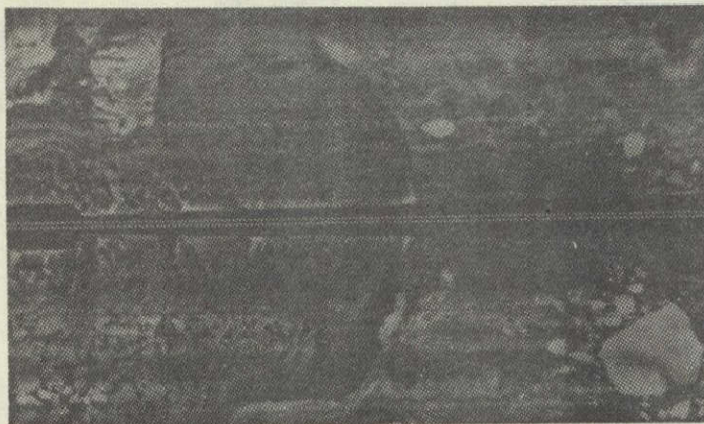
(a) Radar image.
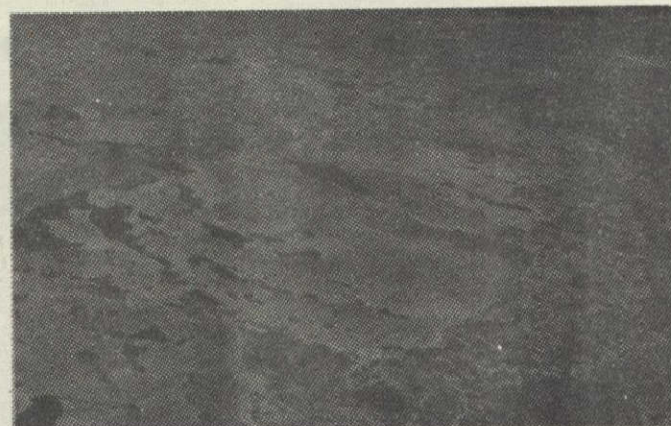
(b) Conventional photograph.
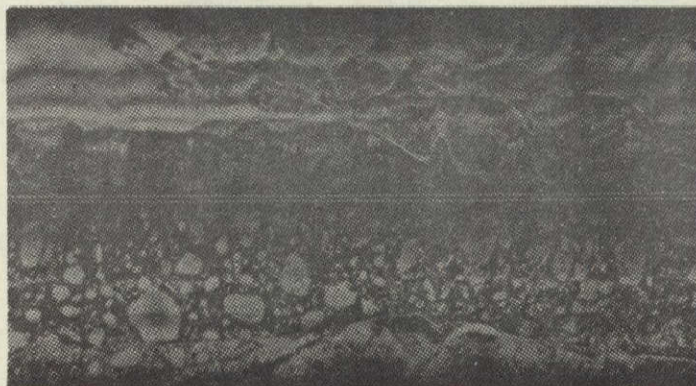
(c) Radar image.

(d) Conventional photograph.

Figure 77.- Data obtained over the Kane Basin and Smith Sound
area between Greenland and Ellesmere Island.
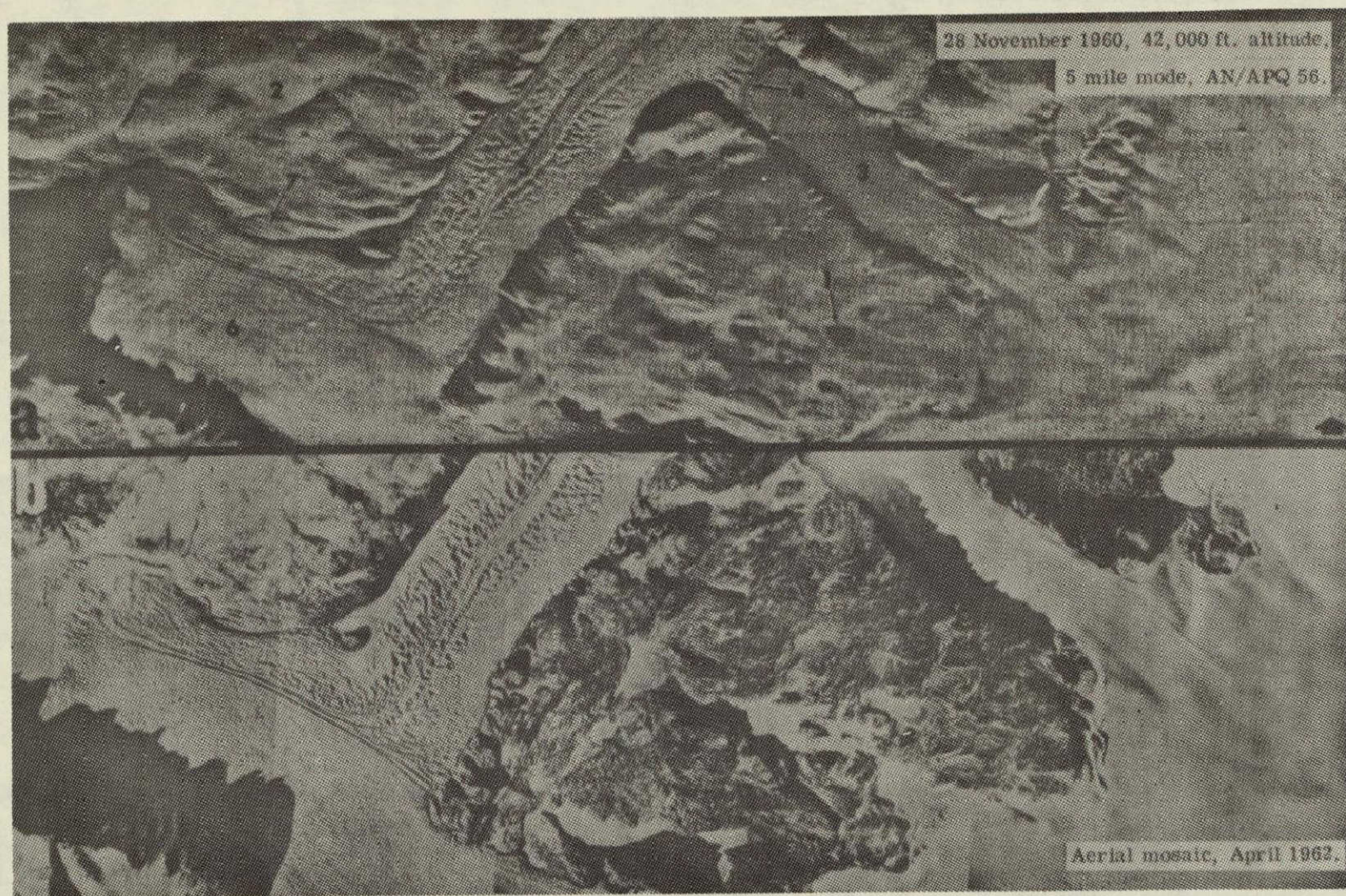
Figure 78.- A comparison of a radar map with an aerial photographic
mosaic of the Leidy Glacier.
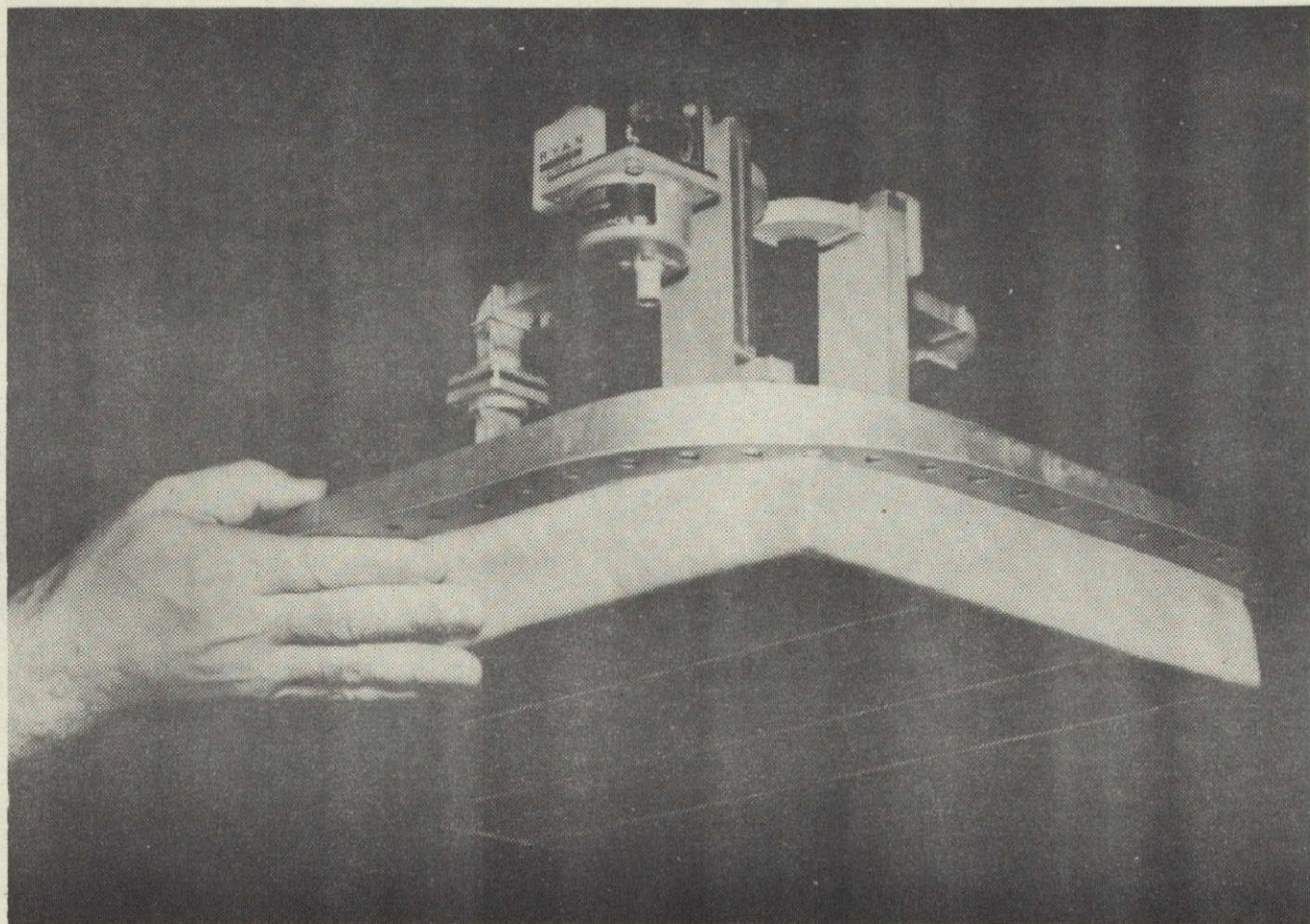
Figure 79.- A planar array antenna (Ryan Redop Scatterometer System).
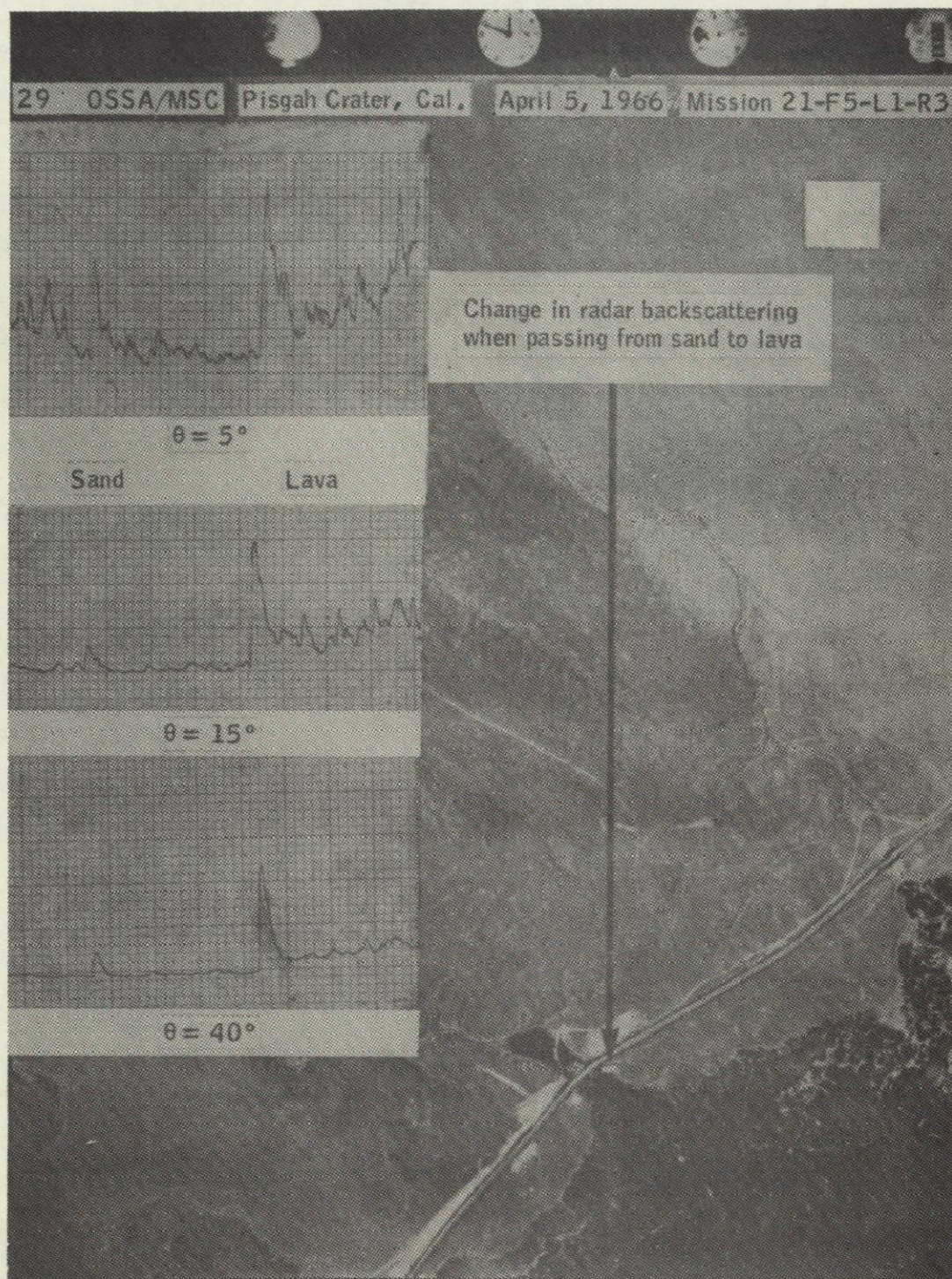
Ryan redop
scatterometer

$$D = \frac{2V}{\lambda} \sin \theta$$

Where: D = Doppler frequency   V = Aircraft velocity
λ = rf wavelength   θ = Angle of incidence
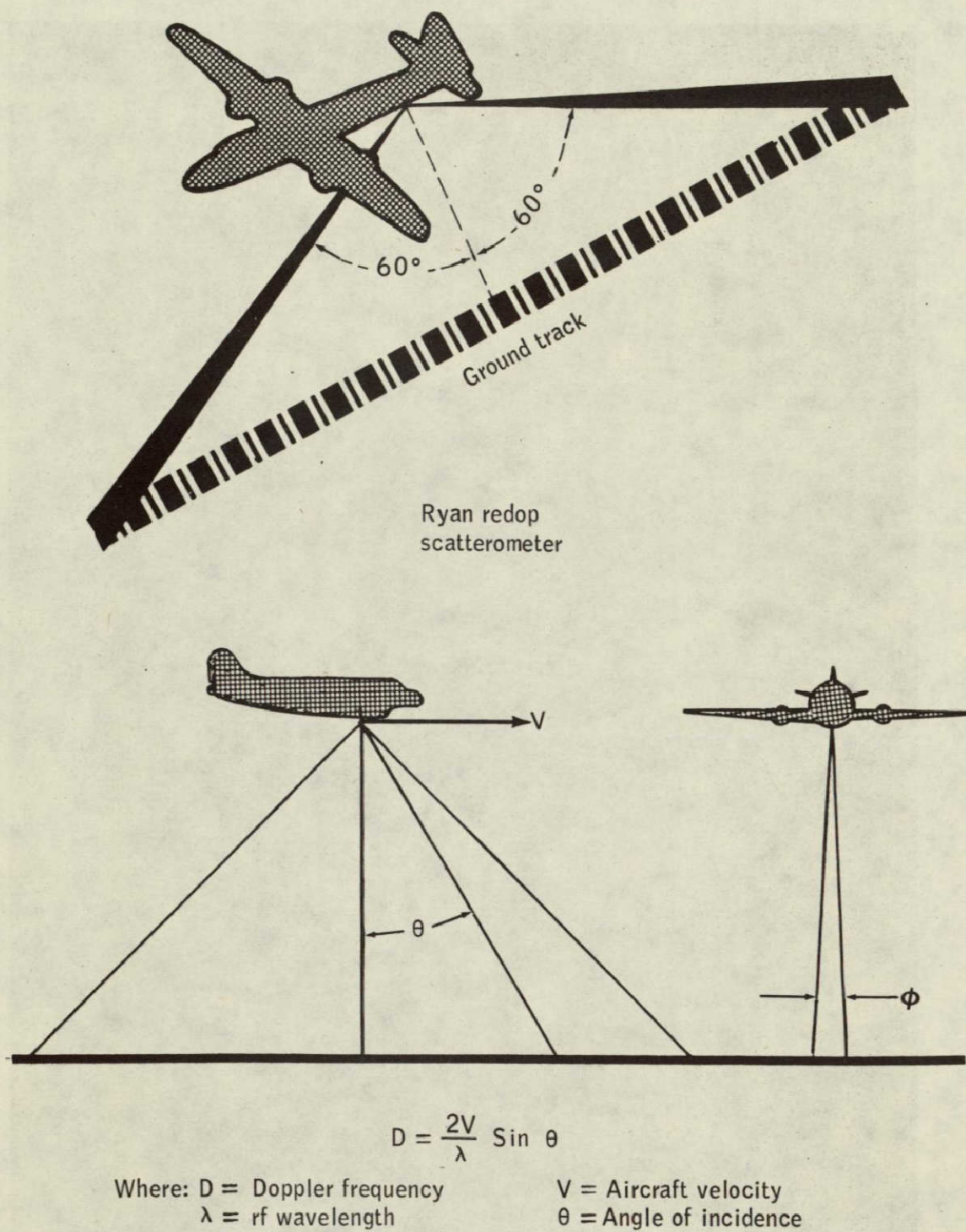
Figure 80.- Redop scatterometer antenna beam geometry.

Figure 81.- A composite of scatterometer and photographic data over the Pisgah volcanic crater area near Barstow, California.
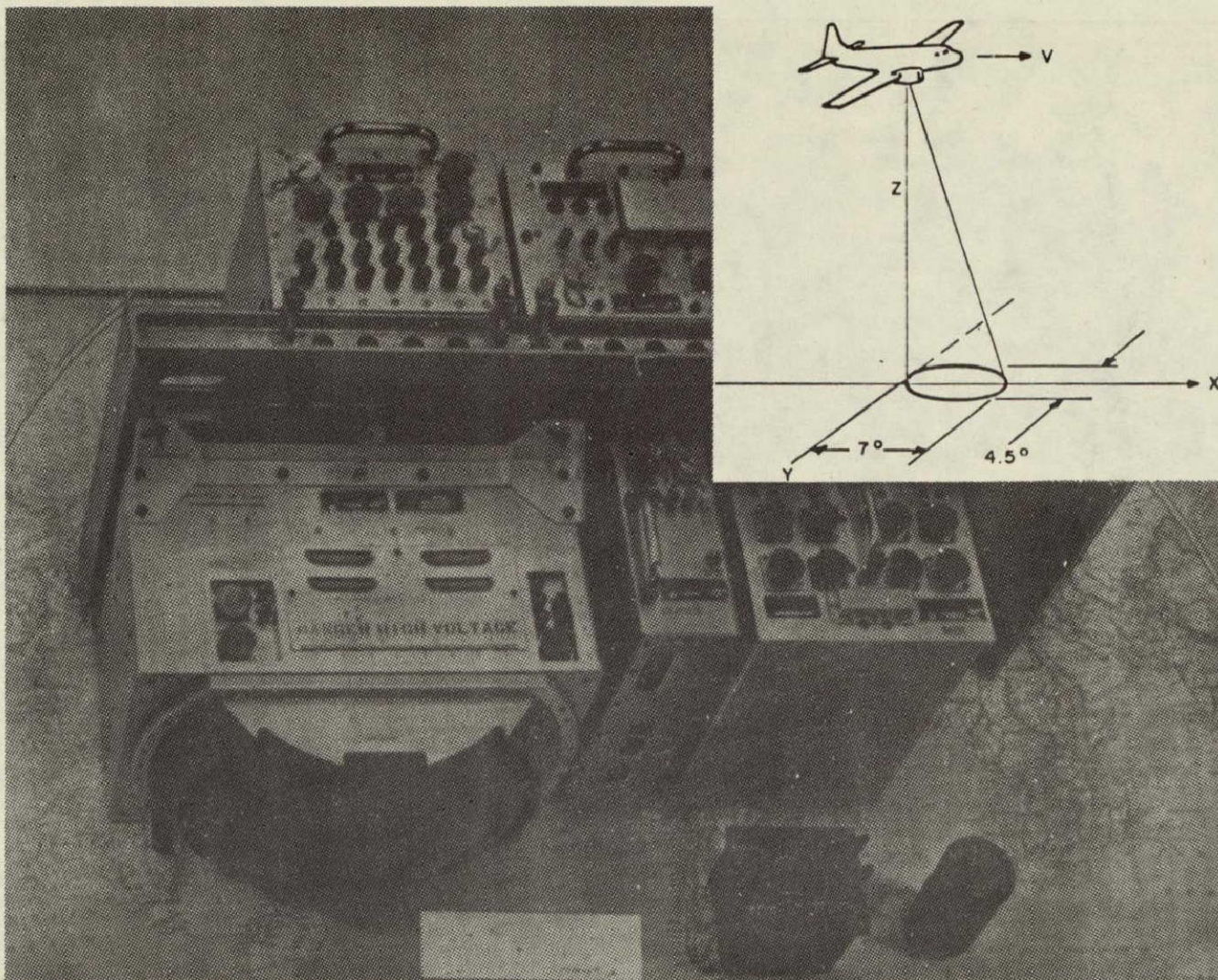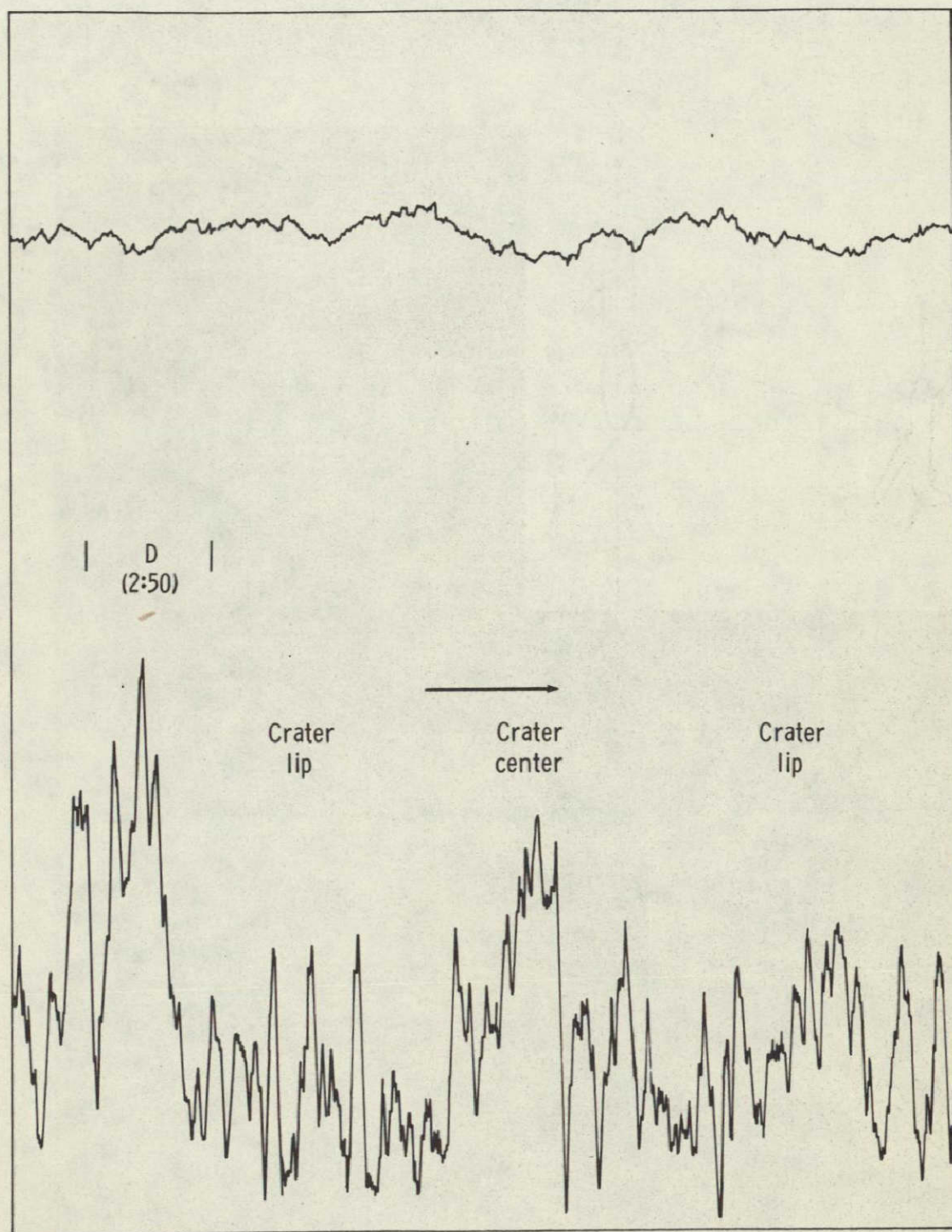
Figure 82.- The Spectrac scatterometer.

Figure 83.- A strip-chart sample of data obtained with the Spectrac system over Meteor Crater, near Winslow, Arizona.

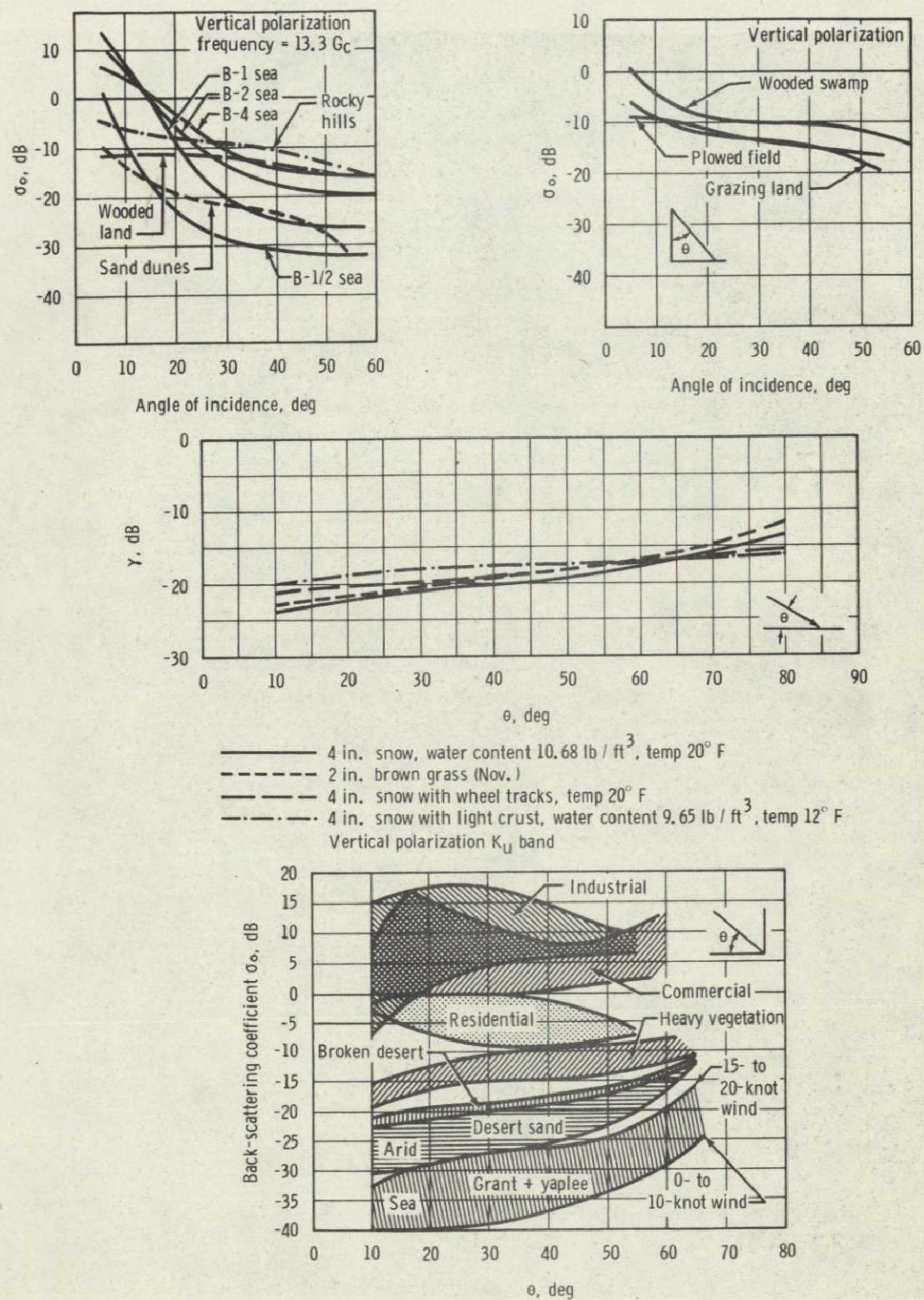Figure 84.- A correlation photograph at 4500 feet over Meteor Crater, near Winslow, Arizona.

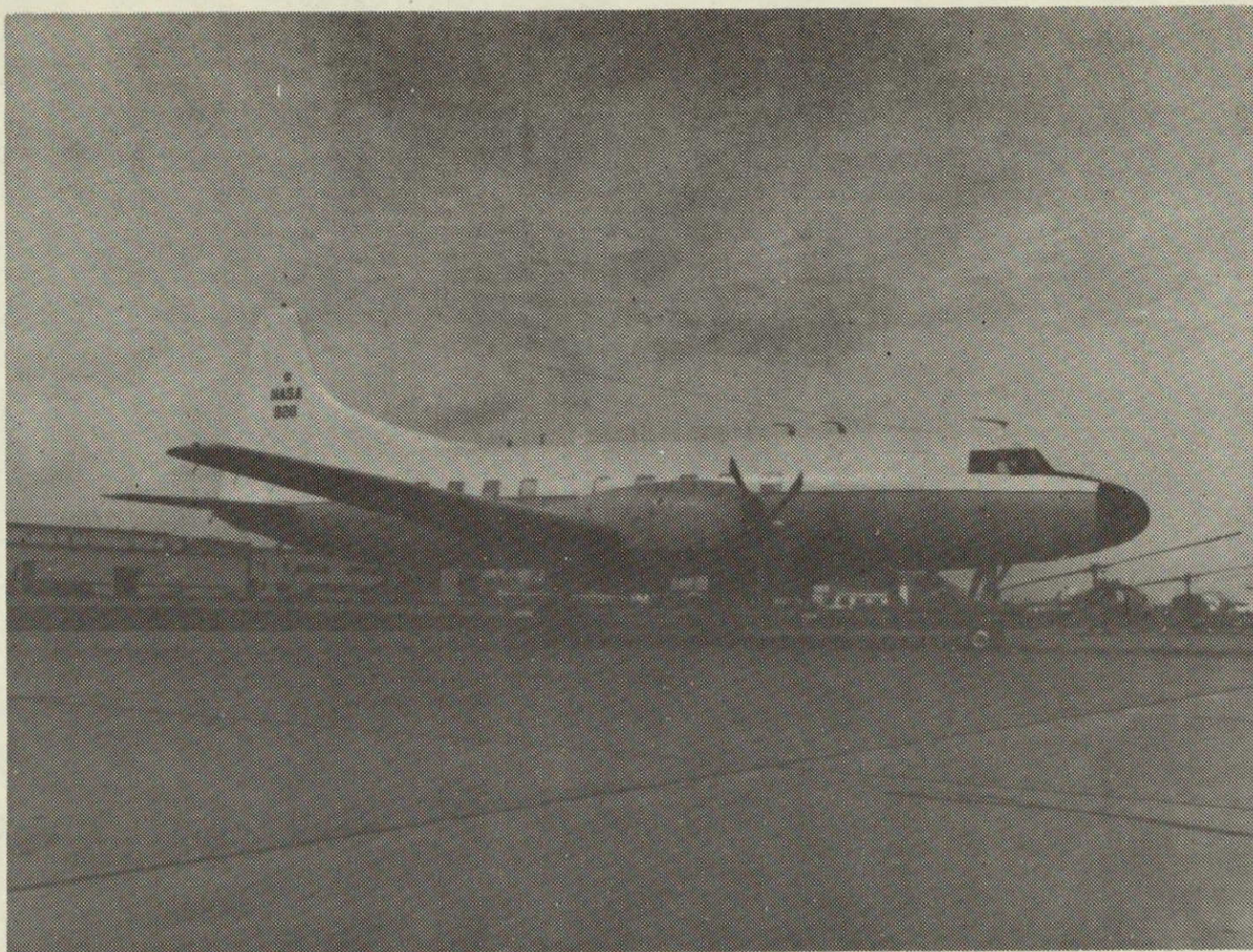Figure 85.— Characteristic curves developed from scatterometer data.

Figure 86.- The NASA-MSC CV-240A aircraft, NASA 926.

Figure 87.- The NASA-MSC NP3A aircraft, NASA 927.